PROPAGATION THROUGH TERAHERTZ WAVEGUIDES WITH PHOTONIC CRYSTAL BOUNDARIES

By

ADAM L. BINGHAM

Bachelor of Science, Optics
University of Rochester
Rochester, New York
2003

Submitted to the Faculty of the
Graduate College of the
Oklahoma State University
in partial fulfillment of
the requirements for
the Degree of
DOCTOR OF PHILOSOPHY
December, 2007

PROPAGATION THROUGH TERAHERTZ WAVEGUIDES WITH PHOTONIC CRYSTAL BOUNDARIES

Dissertation Approved:

Dr. Daniel Grischkowsky
Dissertation Adviser

Dr. Charles Bunting

Dr. Alan Cheville

Dr. Bret Flanders

Dr. A. Gordon Emslie
Dean of the Graduate College

Acknowledgments

There are so many people to thank who helped me find my way to this point. I'll begin by thanking my advisor Dr. Daniel Grischkowsky, who pushed me to excellence and constantly raised the standards of my work. I learned a great deal the past few years, and he's helped me every step of the way. He's been patient when I've needed it, impatient when I've needed it, and I'm very proud of the work we did together. I want to send my gratitude to the rest of my graduate committee, Dr. Alan Cheville, Dr. Charles Bunting, and Dr. Bret Flanders. All were very generous with their time, patience and input. Special thanks to Dr. Cheville, who provided a fresh viewpoint on almost everything academic.

As so much of the research time was spent in the lab, I have to thank Dr. Steve Coleman and Dr. Jianming Dai, who both helped get me started. Steve in particular taught me how to use, build, break and rebuild a THz system. He led by example, and was a major influence on my attitudes toward graduate research and cooking. Dr. Yuguang Zhao also deserves special credit for teaching me how to use the cleanroom to fabricate the photonic crystal structures used in this work. I'm still shocked by how little I knew when I started, but I never felt too overwhelmed, which is a credit to the people who helped me so much.

While there are too many of my fellow grad students/post docs to thank, I would like to give special thanks to Mufei Gong, Dr. John O'Hara, Stacee Harmon, Mo Awad, Dr. Abul Azad, Dr. Matt Reiten, Dr. Jiangquan Zhang, Suchi Ramani, Dr. Norm Laman, and Sree Harsha. All helped me in a variety of ways and I hope I was able to return the favor at some point. Robert Ingraham was always generous with his time and assistance using the SEM and sputter coater upstairs.

Of course, I have to thank my family. Mom and Donnie for providing constant encouragement and support, Granny and Grandpa for always making sure I was passing. I'm pretty sure they still don't know what I've been doing the last 4-5 years, but they've never questioned it, and Mom's main concern was that the THz radiation was going to give me cancer (it didn't). I also want to thank my stepmom Shelagh for pointing OSU's photonics program out in the first place. I wouldn't have come here without her.

Above everyone, I want to thank my wife, Minh Thu. She has been there for me from the start, encouraging me to begin the doctoral program, even though it meant we would be apart for awhile. After she came to live with me in Stillwater, I was reenergized and suddenly my goals didn't seem so impossible. She always provided love and support, and without her, who knows where I would be. I love her very much.

Finally, I want to thank my father, Tom Bingham. He passed away almost eight years ago, but he helped shape everything I am. I still miss him, but I know he would be very proud of me.

Adam Bingham, Nov. 2007

Table of Contents

Chapter **Page**

LIST OF TABLES

Table **Page**

LIST OF FIGURES

Figure **Page**

Figure **Page**

Figure **Page**

Figure **Page**

LIST OF SYMBOLS AND ACRONYMS

1D	one dimensional
2D	two dimensional
3D	three dimensional
17L	pattern of 1D photonic waveguide with 17 lines
17LD	pattern of 1D photonic waveguide with 17 lines including center defect
A	coefficient for scattering matrix calculation
a	PPWG plate spacing
Al	Aluminum
B	coefficient for scattering matrix calculation
c	speed of light in free space (2.998×10^8 m/s)
Cu	copper
D	1/e beam diameter (m)
DC	direct current
dB	decibels
$E_{xxx}(\omega)$	spectral amplitude
E_t	tangential electric field
f	focal length (m)
f_c	cutoff frequency (Hz)
FDTD	finite-difference time-domain
FEM	finite element method
FWHM	full-width at half-maximum
GaAs	Gallium Arsenide
H_t	tangential magnetic field

$H(\omega)$	frequency domain filter for FDTD simulations
j	imaginary number
k	propagation constant ($2\pi/\lambda$)
L	length (m)
L_G	length of grating section (m)
n	index of refraction
PBG	photonic bandgap
PPWG	parallel-plate waveguide
Q	quality factor
$R(\omega)$	reference spectrum
R_s	surface resistance
RIE	refractive ion etching
S_{mn}	scattering matrix coefficients
$S(\omega)$	sample spectrum
SEM	scanning electron microscope
Si	Silicon
SOS	Silicon on Sapphire
$T(\omega)$	frequency dependent amplitude transmission
T_{12}, T_{21}	transmission matrix coefficients
t_{scan}	duration of time scans (ps)
TEM	transverse electromagnetic
THz-TDS	THz time-domain spectroscopy
TE	transverse electric
TM	transverse magnetic
U_{mn}	cascaded scattering matrix coefficients
ω_{02}	1/e beam waist radius (m)
WG-N	nth photonic crystal waveguide cavity
Z_n	impedance of nth mode of PPWG (Ω)
α	absorption coefficient (cm^{-1})
β_n	propagation constant of nth mode of PPWG (m^{-1})
Δf	frequency spacing (Hz)

ε_0	permittivity of free space (8.854×10^{-12} F/m)
ϵ_n	Neumann’s number (dimensionless)
η_0	wave impedance of free space (377 Ω)
θ	angle (degrees or radians)
Φ_n	normalized modal field of the nth mode of a PPWG
λ	wavelength (m)
μ_0	permeability of free space ($4\pi \times 10^{-7}$ H/m)
σ	conductivity (S/m)
ω	radial frequency (radians/s)

Chapter 1 - Introduction

1.1 Terahertz Waveguides

Waveguides have been utilized for propagating electromagnetic waves for over 100 years. From robust, metallic rectangular waveguides at microwave frequencies to flexible dielectric fibers at optical frequencies, waveguides are employed today across the electromagnetic spectrum. As new devices are developed, the initial characterizations of waveguides often begin with determining the modal properties, or the distribution of the fields inside the waveguide. In order to transition to commercial applications, low-loss guides become necessary for long distance propagation. Eventually, integrated optical components are incorporated, allowing control over the guided-wave propagation that is usually only accomplished in free space.

With the rise of Terahertz (THz) frequency technology over the past 20 years, interest has steadily increased in THz waveguides for low-loss, high performance propagation. As techniques used at THz frequencies represent a mix of those found in microwave and optical frequencies, research into waveguiding structures has overlapped significantly with those fields. In particular, the search for the ideal guided-wave structure has led to investigations in circular [1], fiber [2], rectangular [3], dielectric [4], parallel-plate [5], coaxial [6], and single-wire waveguides [7-8]. While all of the above waveguides have their advantages, the transverse electromagnetic (TEM) mode of the parallel plate waveguide (PPWG) has thus far demonstrated the best combination of overall propagation characteristics for the guiding of sub-ps THz pulses including (relatively) low-loss, no modal-dispersion, high free-space coupling, and simple fabrication when compared to the other guides.

While the PPWG offers many advantages over other guided wave channels at THz frequencies, it also has proven surprisingly amenable to the inclusion of other guided wave components, enhancing its utility. As such, a great deal of research has been focused on creating a ‘toolbox’ of integrated components including planar/spherical metallic mirrors [8,9], transmitters [1], dielectric lenses [11], photonic crystals [12-13,12-15], receivers [16], resonators [16], superprisms [17] and others. Generally these components could be classified as being guiding, shaping, generating, detecting or filtering. Additionally, the PPWG may serve as a useful tool to simulate 3D structures and experiments in a 2D setting [12-13].

1.2 THz Photonic Crystals

At optical frequencies, photonic crystals have quickly evolved from theoretical curiosities to commercial products [18-20]. A photonic crystal is an artificial material with a periodically varying dielectric constant, which results in photonic bandgaps, where the propagation of certain frequencies of electromagnetic waves is prohibited in certain directions. This phenomenon is most commonly compared to the electronic bandgaps found in semiconductors where electrons are forbidden from having certain energy levels due to periodic variations of the potential due to the crystal structure. Photonic crystals have now been well characterized in both the microwave and optical regimes.

At THz frequencies photonic crystal demonstrations have included 1-D dielectric stacks [21], 2-D metallic and dielectric photonic crystals embedded in PPWGs [12-13,12-15], free-standing dielectric 2D photonic crystals fabricated via reactive ion etching [22], plastic photonic crystal fibers [23], hole arrays [24], and free-standing metallic cylinders [25-26]. The primary demonstrations of photonic crystals at THz frequencies demonstrated their filtering capability, with typical stopbands having a dynamic range on the order of 10-20 dB (ranging up to 40 dB) over varying bandwidths.

While the most obvious application of a photonic crystal is as a filter, their more promising capability as a waveguide has been underutilized at THz frequencies. The first THz waveguide demonstration involved an array of plastic cylinders stacked together with an air core forming a photonic crystal fiber [23]. This device had very similar performance to sapphire fibers that had been previously demonstrated [2]. A subsequent Teflon photonic crystal fiber attained loss of 0.3 cm^{-1} at 1 THz, which is still approximately a factor of 5 greater than the theoretical loss for a copper PPWG with 100 μm plate spacing [27]. One demonstration used 1-D dielectric photonic crystal slabs to guide the light with excellent overall performance including a very low attenuation coefficient of 0.1 cm^{-1} at an unspecified frequency [28]. Photonic crystal waveguides have been the subject of numerical simulations at THz frequencies [29], including one demonstration of a planar guiding structure with novel geometry that appears to have excellent guiding characteristics (the loss was not specified) [30]. An unbound, air-core photonic crystal waveguide which acts as a passband filter was fabricated on a Silicon wafer [31]. While research has continued, experimental demonstration of planar photonic crystal guiding, which is necessary for single-chip interconnects, has been lacking.

1.3 Purpose of This Study

While current PPWG technology is the ideal tool for many THz applications, the necessary 1-D propagation of the PPWG limits the ability to form on-chip circuitry. While rectangular waveguides offer the potential of 2-D integrated pathways, little effort has gone towards implementing them due to the higher attenuation coefficient relative to a typical PPWG, and the dispersive propagation of the TE_{10} mode. As development of single frequency THz sources continues, dispersion will become a less important design constraint. Loss however remains a critical concern. Photonic crystal waveguides offer great potential in terms of low-loss propagation. More importantly, photonic crystal waveguides offer a platform upon which a 2D world of integrated pathways, devices and components can be implemented. These integrated devices will form the foundation for all future applications of THz guided waveguide technology including sensors, interferometers, lasers, and other devices.

Before characterizing photonic crystal waveguides, it was necessary to determine transmission properties of the photonic crystal lattice. However, the initial attempt to observe the output through a metallic photonic crystal in a PPWG yielded no transmission. In order to obtain transmission, the symmetry of the waveguide was broken by installing a 100 μm air gap between the top of the 70 μm tall photonic crystal structure. Transmission through the air gap was observed, with extremely strong stopbands showing as much as 40 dB of dynamic range with extremely sharp turn-ons [32].

Following the observation of strong stopbands through air-filled asymmetric photonic crystal filled waveguides, the research described in this dissertation revolves around utilizing periodic lattices (be they corrugated sidewalls or bounded photonic crystals) to filter, guide, shape and modulate THz beams inside the confines of a PPWG, often with dramatic results. The 2-D photonic crystal substrates were fabricated in-house at the Ultrafast Terahertz Optoelectronic Laboratory cleanroom, taking advangtage of micro-electro-mechanical systems (MEMS) technology. This allows experiments to be rapidly conceived, designed, and tested. The essential ingredient in each of the THz waveguides demonstrated here is the incorporation of photonic crystal boundary which dramatically alters an otherwise ordinary PPWG. After failed attempts to theoretically model the 2D structure, a simpler 1D structure will be demonstrated with similar results. A theoretical treatment utilizing the mode matching technique will be used to analytically calculate the transmission through the 1D structure, yielding design control, and physical understanding of the stopband formation [33]. As a waveguide-integrated filter, the performance of the photonic waveguides is among the best demonstrated at THz frequencies in terms of dynamic range and the sharpness of the turn-ons.

After characterization of the photonic waveguides, the photonic crystal structure will be used to provide a side wall in the PPWG setting producing the photonic crystal waveguide envisioned earlier. The loss will be experimentally determined and compared to a conventional rectangular waveguide. Numerical methods will be used to theoretically model the photonic crystal waveguides,

While studying the photonic crystal geometry for waveguiding applications is part of the goal for this dissertation, proof of its value as a platform for 2D on-chip circuitry is demonstrated by the integration of defect cavities. In both the photonic waveguide and the photonic crystal waveguide geometries, the desire to integrate components is addressed by the integration of resonant cavities inside these structures. These cavities allow long lasting resonances to build up inside the waveguide, resulting in very sharp linewidths and corresponding high Q values. High Q resonators have many potential applications in high-sensitivity sensing and detection. Photonic crystal’s powerful confinement capabilities will be tested against standard rectangular waveguide cavities.

1.4 Outline of Thesis

Chapter 2 will describe the Experimental Setup used to characterize these Photonic Waveguides. This will include a description of the standard THz-TDS system, including beam profile calculations and waveguide coupling effects. The fabrication of the PPWGs will be described. The lithographic fabrication process used to create the periodic structure will be described in detail, and its benefits will be noted.

Chapter 3 will present experimental results for the Photonic Waveguides, where one of the waveguide plates has been replaced by a plate with a finite metallic photonic crystal boundary. The transition from 2D geometry to 1D geometry will be explored and experimental data for both 1D and 2D boundaries will be shown. A defect will be incorporated into the 1D geometry allowing a sharp resonance to build up.

Chapter 4 will go into detail on the theoretical techniques used to calculate the output of the 1D Photonic Waveguides presented in Chapter 3, concentrating on the application of the mode-matching technique. A favorable comparison between theory and experiment will be shown. Physical insight gained from the theoretical modeling along with previous observations of tunable 2D photonic waveguides will be discussed.

Chapter 5 will describe the photonic crystal waveguides, where photonic crystal sidewalls are placed inside the PPWG. There are demonstrations of both dielectric and metallic photonic crystal waveguides of varying lengths. Absorption data will be compared to that of a rectangular waveguide, and general propagation characteristics will be discussed. Numerical simulations will be used to provide a theoretical comparison to the experimental data.

Chapter 6 will describe the development of integrated devices for the photonic crystal waveguide. A variety of photonic crystal waveguide cavities will be designed and experimentally verified. Demonstrations of side-coupled cavities in a rectangular waveguide will be used as a comparison for the photonic crystal waveguide cavities.

Chapter 7 will review the work presented here and draw conclusions about what has been learned. Future work will also be discussed.

Chapter 2 - Experimental Setup & Apparatus

A variety of experimental and fabrication techniques were necessary to perform the experiments described in this dissertation. As all of the experimental work utilized a THz Time-Domain Spectroscopy (THz-TDS) system which has been well detailed in a number of places, a relatively short review will be given. The remainder of the chapter will characterize the parallel plate waveguides, and detail the fabrication the photonic crystal chips.

2.1 THz-TDS Setup

The standard experimental system for spectroscopic analysis at THz frequencies is known as a THz-TDS system. An illustration of a typical system is shown in Figure 2.1. A KLM Ti:Sapphire femtosecond laser pumped by a Spectra Physics Millennia Laser produces ~80 fs pulses with a center wavelength of 810 nm which are used to excite the transmitter and receiver. The transmitter consists of coplanar 10 μm aluminum lines on a GaAs substrate, separated by 80 μm. These lines are biased at 70 V, and the optical beam is brought to a 5 um focus near the anode line of the transmitter. The laser pulse produces charge carriers in the GaAs substrate, which are then accelerated towards the lines creating a near single cycle pulse of electromagnetic energy. Due to the near single-cycle pulse shape, the broadband frequency spectrum extends from 0.1 to 4.0 THz. The THz radiation is then coupled to a spherical silicon lens which is approximately index matched to the GaAs transmitter. The silicon lens serves to collimate the radiation as it begins to propagate in free space. To an adequate approximation, the size of the beam as it travels in through space can be determined by Gaussian beam theory.

The confocal optical system which makes up the backbone of the experiments described in this dissertation is illustrated in Figure 2.1. Upon exiting the transmitter/silicon lens, the beam then travels 119 mm to a parabolic mirror with focal length f = 119 mm. The beam then travels an additional 119 mm where it then reaches a second, frequency-dependent focus at the center beam waist of the system. The second half of the optical system is a mirror image of the first providing 1:1 imaging of the transmitted beam on the receiver. Benefits of the confocal setup include unity power coupling throughout the system, and a focused beam in the center of the system, creating an optimal location for sample placement as shown in Figure 2.1. The beam radius as a function of frequency is plotted in Figure 2.2 using a MATLAB program named GB Menu developed by Dr. Alan Cheville [34]. Due to the broad bandwidth of the system, the beam waist at the center of the system ranges from approximately 9 mm at 0.5 THz to 1 mm at 4 THz.

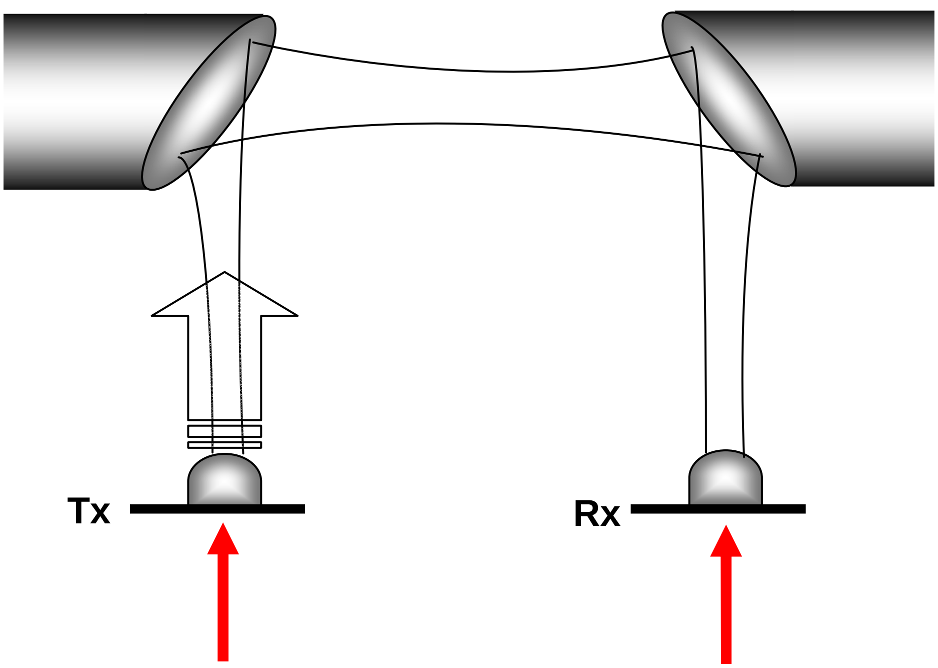

Figure 2-1 - Diagram of standard THz-TDS system [36]

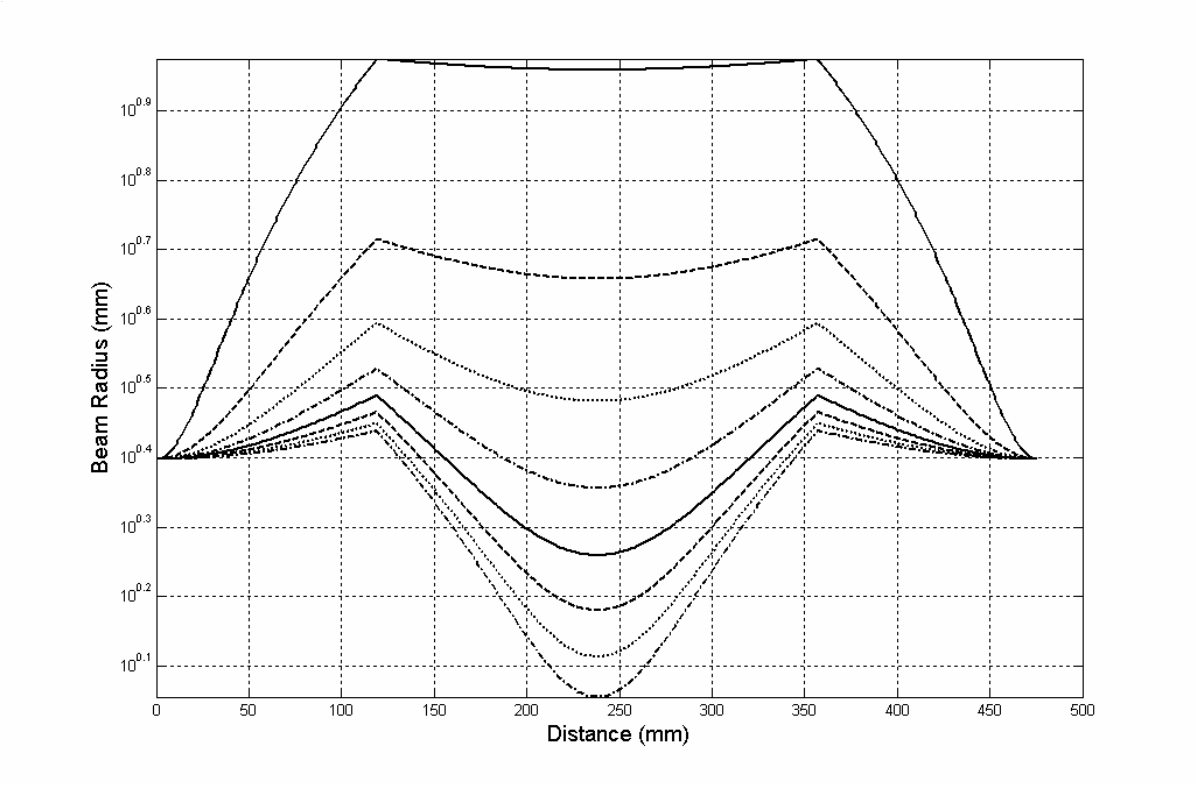

Figure 2-2 **-** Approximate Beam Waist of THz beam as it propagates through the system. The different lines represent discrete frequencies, each spaced 0.5 THz apart. The upper most line is the 0.5 THz, and the lowest line is 4.0 THz. The waveguide/Si Lens apparatus will be placed at the center beam waist of the system.

Once the beam has traversed the optical system it is focused by a silicon lens onto the receiving antenna. The silicon-on-sapphire (SOS) antenna is again patterned with transmission lines, only this time there is a 10 μm wide dipole in the center of the lines. The THz beam is focused onto the dipole attached to the 5 μm wide unbiased transmission lines. Another optical pulse, split off from excitation optical pulse, and temporally delayed to arrive at the receiver at the same time as the THz pulse, hits the receiver again exciting carriers. This makes the spot conductive, allowing a current amplifier to measure and amplify the current induced by the THz pulse hitting the receiver. The optical pulse hitting the receiver pulse is shifted in time, sweeping through the entire THz waveform, and data is acquired through a lock-in amplifier which is connected to a chopper which modulates the THz radiation at approximately 330 Hz.

Typically the system is used for spectroscopic purposes by comparing both the pulse information and the Fourier-transformed spectral information of a sample and appropriate reference pulse. The change induced by the sample can yield a great deal of information about the sample including absorption, phase change, index of refraction, and numerous other sample dependent quantities. In the work presented here, the reference will almost always be an unperturbed PPWG. A typical free space THz pulse and spectrum are shown in Figure 2.3.

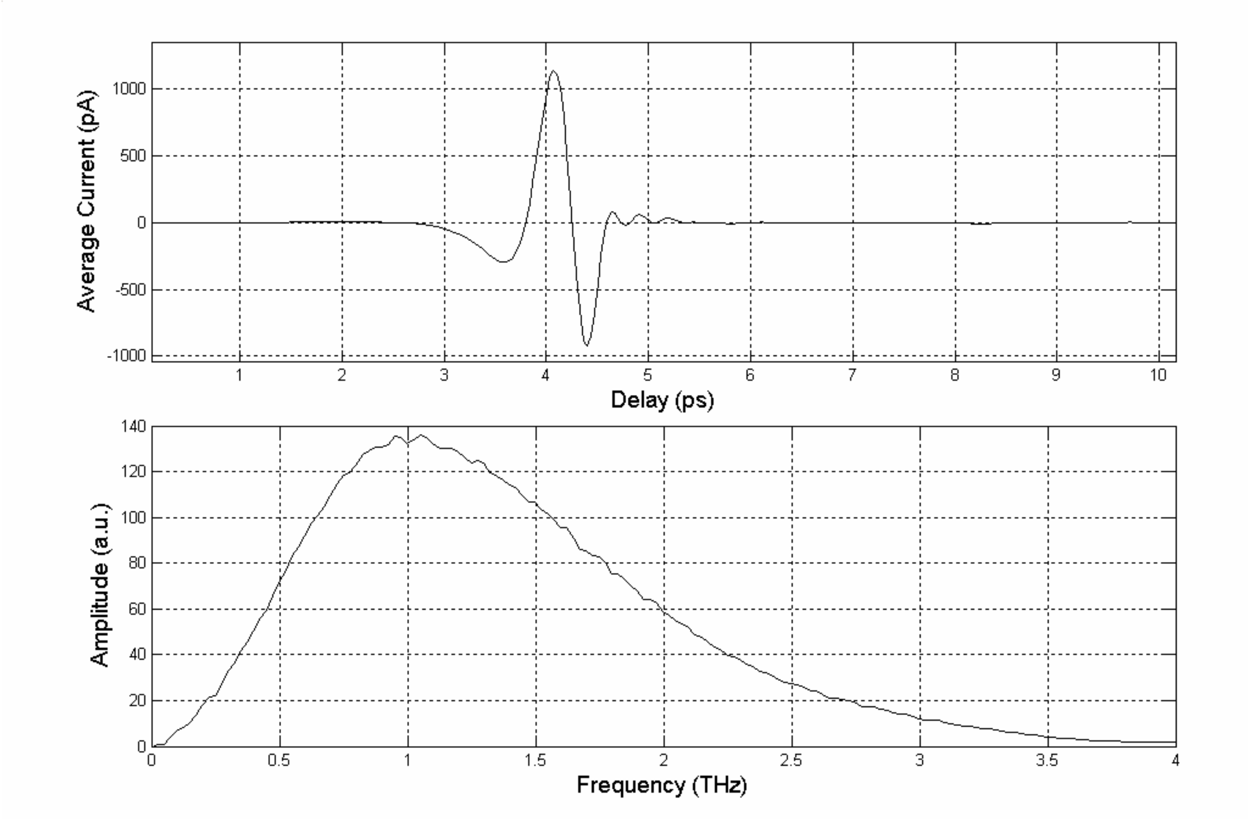

Figure 2-3 - Typical free space THz pulse. (a) THz pulse from system used to perform experiments in this dissertation. The pulse is slightly chirped with the high frequency components arriving slightly later in time. (b) Spectral Amplitude of (a). The spectrum extends from 0 to 4.0 THz. The oscillations in the spectrum are likely due to residual water vapor in the system.

The time-domain pulse shown in Figure 2.3 has a scan length of 10 ps. This limits the frequency-domain resolution to

$$\Delta f = {}^{1}\!/_{t_{scan}} = 100GHz \tag{2.1}$$

where Δf is the spacing between frequency data points, and t_{scan} is the total length of the scan. As there is no time-domain signal after 6 ps, all the frequency-domain features will be resolved. However, resolving sharp frequency domain features requires much longer scans to properly resolve. Ideally, the scans should last long enough to observe all time-domain data.

However, two factors limit the length of time-domain scans. First, once the signal drops below the noise level of the system, it becomes indistinguishable from the noise, and therefore the scans must be stop. Second, for many cases, there are reflections that appear in the time-domain signals which cause Fabry-Perot oscillations in the frequency-domain, altering the natural shape of the data. Many of the scans shown in this dissertation have been truncated to avoid reflections in the time-domain. In the cases where some features are not fully resolved, longer time scans are taken, however, the spectra shown will also be from the truncated pulses. For most cases, the scans will be truncated at 130 ps, giving a resolution of 7.7 GHz, which provides adequate resolution for all but the sharpest features.

2.2 Waveguide Fabrication and Design

As previously stated, one of the advantages of PPWGs is their simple fabrication. The PPWGs used in these experiments were fabricated by taking two aluminum plates with typical dimensions of 1” long x 3” wide x 0.5” thick and polishing them to a mirror like finish. Sandpaper, jeweler’s rouge, and a chemical polish were used in combination to achieve the desired finish. The plates were then placed together separated by only small metal spacers which maintained a constant plate spacing. Figure 2.4 shows a common Aluminum PPWG along with the mount used to hold the waveguide. The Silicon coupling optics are not pictured.

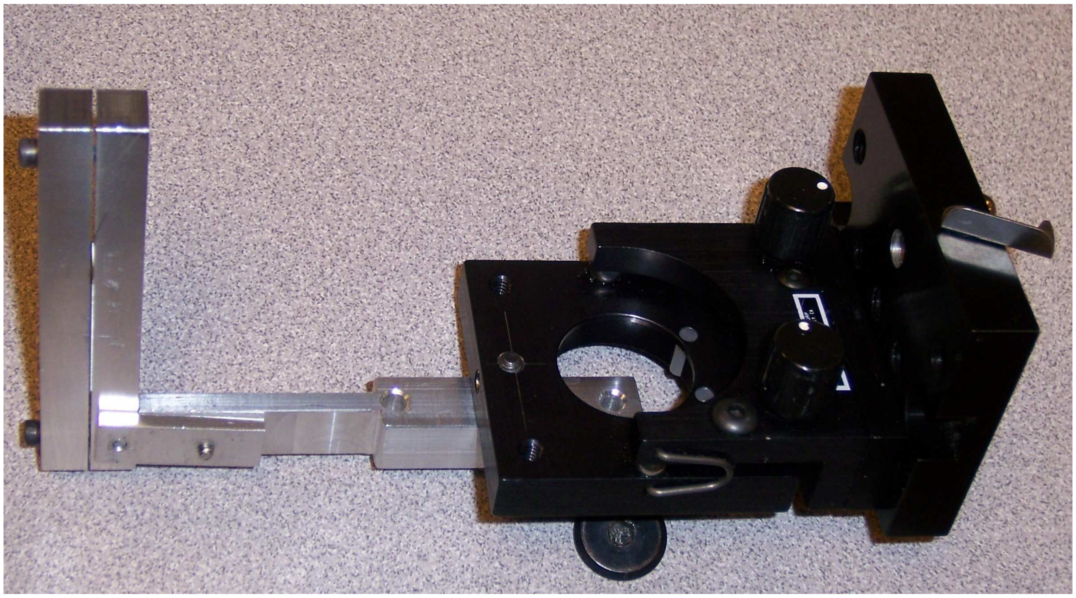

Figure 2-4 - Parallel Plate Waveguide and mount. The 1 cm long waveguide is fabricated out of Aluminum. For this short waveguide, the silicon lenses are mounted separately and butted up against the waveguide in the THz-TDS system. Longer waveguides often have optics mounted directly onto the waveguide.

The primary considerations in waveguide design are the loss processes. Waveguide losses can be divided into two groups, Ohmic losses and coupling losses. The Ohmic losses stem from the finite conductivity of the metal plates of the waveguide. These losses are minimized by keeping reasonable propagation lengths inside the PPWG, and choosing a metal with a high DC conductivity. For these reasons, all PPWGs used in the following experiments were less than 1” long, and Aluminum was used for the metal plates. For a 1” Al waveguide with an 100 μm plate spacing, this leads to 70% transmission at 4.0 THz (the trail end of the bandwidth).

The coupling losses are determined by the overlap of the spatial field of the propagating beam at the waveguide aperture and the modal field distributions inside of the waveguide. Our linearly polarized field is a good match with the TEM (TM_0) mode of the PPWG, resulting in excellent coupling across the waveguide aperture. Due to the symmetrical nature of our beam, only even modes are excited as the coupling to odd modes is negligible. Typically a 100 μm plate spacing is used, meaning the first higher order mode that can be excited is the TM_2 mode, which has a cutoff frequency of 3.0 THz. However, the coupling to this mode is still very small, and experiments have shown that only the TEM mode is excited from 0 to 4 THz for plate spacing less than 150 μm.

One important difference between the standard THz-TDS system described in section 2.1 and the one used in the experiments described in this dissertation is the inclusion of plano-cylindrical silicon optics for waveguide coupling. The lens produces a line focus, with a minor axis radius given by equation (2.2) [35-36].

$$w_{02} = \frac{\lambda f}{\pi w_{01}} \tag{2.2}$$

where f is the focal length of the silicon lens, and w_{01} is the input beam radius. At 1 THz, for a 9 mm beam and a focal length of f = 6.71 mm, w_{02} = 150 μm. This dramatically improves free space coupling, as the THz beam is focused from an approximate 1/e diameter of 9 mm (at 1 THz) to a diameter of 300 μm.

2.3 Fabrication of Photonic Crystal Samples

The 1-D and 2-D periodic structures that will be inserted into the PPWG as shown in the next chapter were fabricated in the UTOL clean-room following a standard SU-8 negative photoresist processing procedure. A typical metalized 2D photonic crystal lattice on a Si substrate is shown in Figure 2.5. To fabricate this structure, a 3” diameter, ~500 μm thick silicon wafer is metallized with 300 nm of Aluminum in a thermal evaporator. This initial metallic layer had two benefits. First, the adhesion between SU-8 and Aluminum is slightly improved over that of SU-8 and silicon. Second, if there was to be no further metallization to the sample, the periodic structure was already on a metallic substrate, meaning it could be inserted into a PPWG and tested.

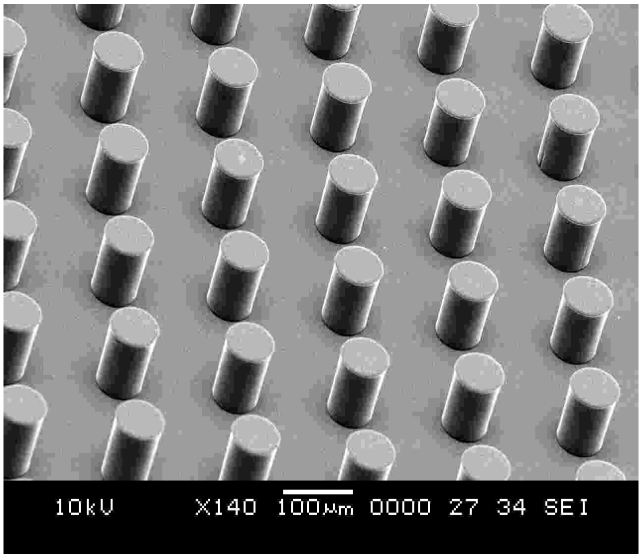

Figure 2-5 - Photonic Crystal structure made of metallized SU-8 photoresist. The cylinders are approximately 70 μm tall and 70 μm in diameter. The period between cylinders is 160 μm.

After metallization, the silicon wafer is then cleaned and a 20 μm to 70 μm layer of SU-8 photoresist is spun onto the wafer. After a brief soft-bake, the wafer is exposed to UV light through a customized mask designed to yield the desired structure for between 30 and 90 seconds (depending on the layer thickness), and then soft baked on a hot plate at 95° C. The masks were custom designed and the features had sub-micron dimensional precision. The wafer is then developed in SU-8 developer for approximately 6 minutes, before being rinsed in Isopropanol, and hard baked at 150° C. To metallize the now hardened SU-8 structures, the wafer is placed in a Cressington 108auto sputter-coater, which yields even coverage over the entire wafer surface (including the sidewalls). Approximately 400 nm of Au is sputtered on the wafer surface. This completes the development process. The SU-8 film thickness was measured to be uniform within a range of +/- 2 um across the surface of the wafer. After dicing into (typically) 1” x 1” squares, the wafers were inserted into a fitted PPWG, and the entire setup was placed inside the THz-TDS system. The silicon lenses were mounted directly onto the waveguide (for plano-cylindrical lenses), or in separate xyz holders (for the hyper-hemispherical lenses).

The SU-8 process is extremely versatile, producing a wide variety of desired patterns and structures varying from pillars, holes, grating lines in arrays of varying complexity. Once hard-baked, the SU-8 structures are relatively robust (considering their size), and can act as spacers between the waveguide plates. Most importantly the SU-8 process provides nearly-ideal structure with smooth sidewalls and no undercutting especially when compared to most etching processes. The reproducibility of the cleanroom processes ensures the excellent quality of the structures and repeatable results tested in the laboratory.

Chapter 3 - Experimental Results I: 2-D and 1-D Photonic Waveguides

The initial plan for the experiment presented here was to incorporate 2D photonic crystal cylinder structures as described in Chapter 2 into the metal PPWG to control the frequency dependent transmission. As the TEM mode has no spatial dependence in the dimension perpendicular to the plates of the PPWG, three-dimensional photonic crystal cylinder structures can be replicated in the two dimensional (2D) geometry of the PPWG [13]. Due to the lack of transmission through the 250-period metallic photonic crystal, the 2D photonic crystal symmetry was broken by incorporating an air gap between the tops of the cylinders and the upper parallel plate of the waveguide. While this structure was much more geometrically complex than the initial metallic photonic waveguide, the air space allowed THz to propagate through the waveguide, and as will be shown, powerful filtering effects were observed. PPWGs with a periodic boundary on one of the plates will be designated as Photonic Waveguides.

3.1 2-D Photonic PPWGs

The fabrication procedure for the 2-D photonic waveguides was outlined in Chapter 2. Figure 3.1 shows scanning electron microscope (SEM) images of two such photonic bandgap (PBG) surfaces which will be integrated into waveguides and analyzed in this section. The leftmost SEM image in Figure 3.1 shows a PBG surface consisting of 70 μm tall cylindrical pillars in a planar square array. This will be designated as the type I photonic surface. Although the array was fabricated using a lithographic mask that has precise 60 μm diameter holes with a 160 μm array period, the diameter of the cylinders increased to approximately 70 μm during the development process. The rightmost SEM image in Figure 3.1 a PBG surface consisting of 70 μm deep holes in a hexagonal array. This will be designated as the type II photonic surface. For this pattern, the mask had an array period of 100 μm, and a hole diameter of 60 μm. During the development process, the diameter of the holes decreased to approximately 40 μm.

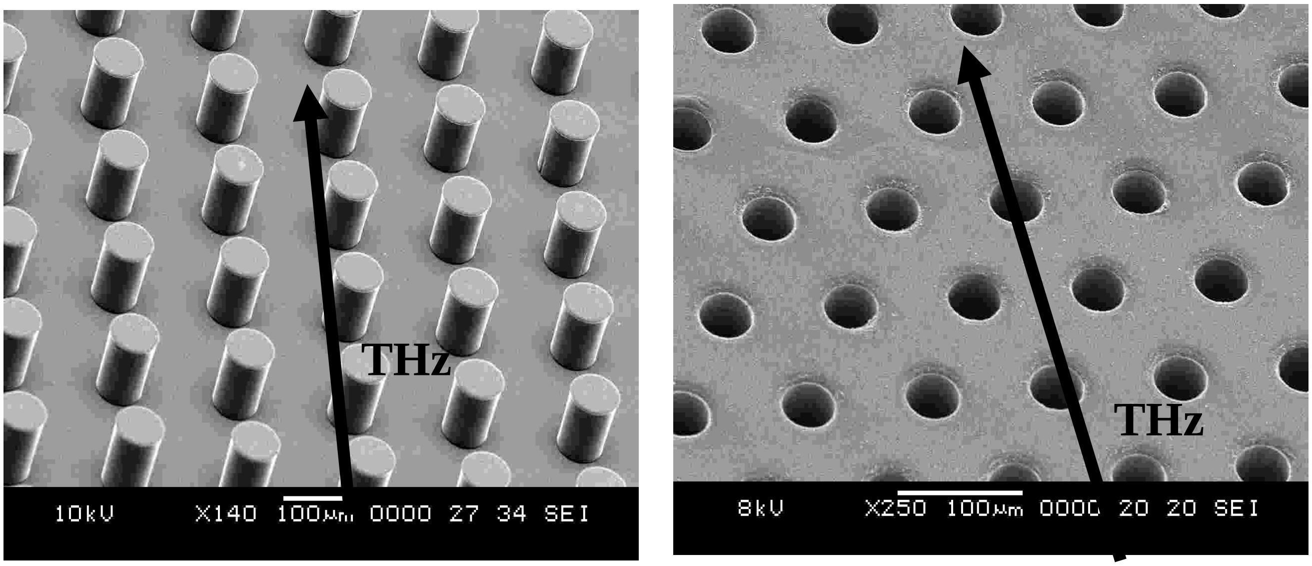

Figure 3-1 - Left SEM image is the type I PBG surface. Right SEM image is the type II PBG surface [32].

The photonic surfaces shown in Figure 3.1 were diced into square 25.4 x 25.4 mm chips, and placed in a matched Aluminum PPWG. The resulting parallel plate photonic waveguides were characterized in the THz time-domain spectroscopy (THz-TDS) system discussed in Chapter 2. A reference THz pulses was measured through a 25.4 mm square Cu PPWG with 100 μm plate separation. For the purposes of this experiment, we assume the difference in loss between the copper waveguide and the aluminum waveguide is negligible. Theoretically, the output transmission is reduced only 4% at 1 THz by using an Aluminum waveguide. Two plano-cylindrical silicon lenses are used to couple the radiation into and out of the waveguide, placed at the confocal beam waist of the THz-TDS system. 100 μm edge spacers are placed between the other Al plate and the metallic PBG surface to create an even plate spacing across the sample. The propagation directions relative to the PBG surfaces are indicated in

Figure 3.1. The incoming THz pulse is polarized perpendicular to the plate surfaces. Figure 3.2 illustrates the geometry of the waveguide on an exaggerated scale.

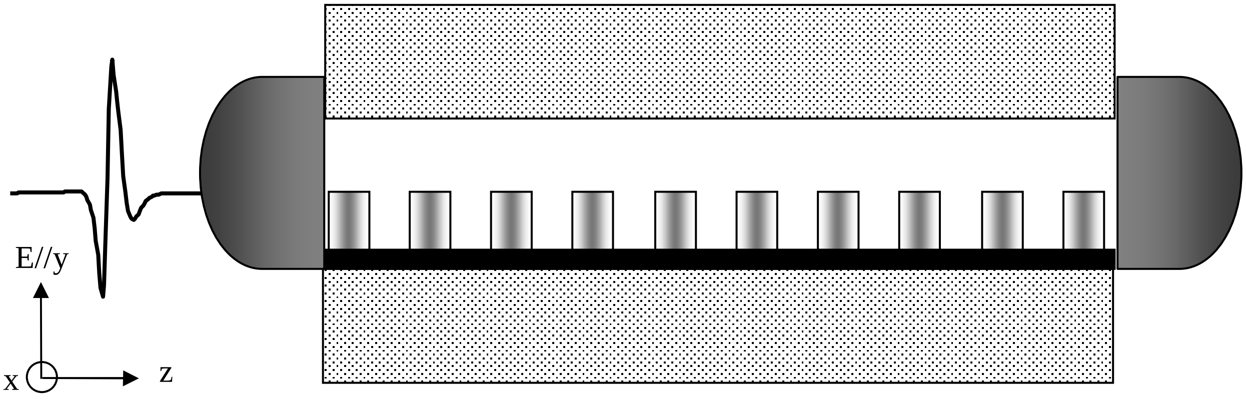

Figure 3-2 - Illustration of type I photonic waveguide. The THz pulse is polarized in the y direction for maximum transmission.

Figure 3.3 shows the normalized output spectra from the type I and type II photonic waveguides plotted against the reference spectrum. Inset in Figure 3.3 THz reference pulse. The two photonic waveguides act as powerful filters creating bandgaps of varying sizes. The type I photonic waveguide, which is represented by the shaded spectrum demonstrates, bandgaps as wide as 1 THz, with very sharp sidewalls. The type II photonic waveguide has a much more transmissive with, narrow bandgaps. The bandgaps in both spectra appear to completely block the signal. While the reference pulse spectrum extends to 4 THz, there is no transmission observed beyond 3 THz for either of the two photonic waveguides.

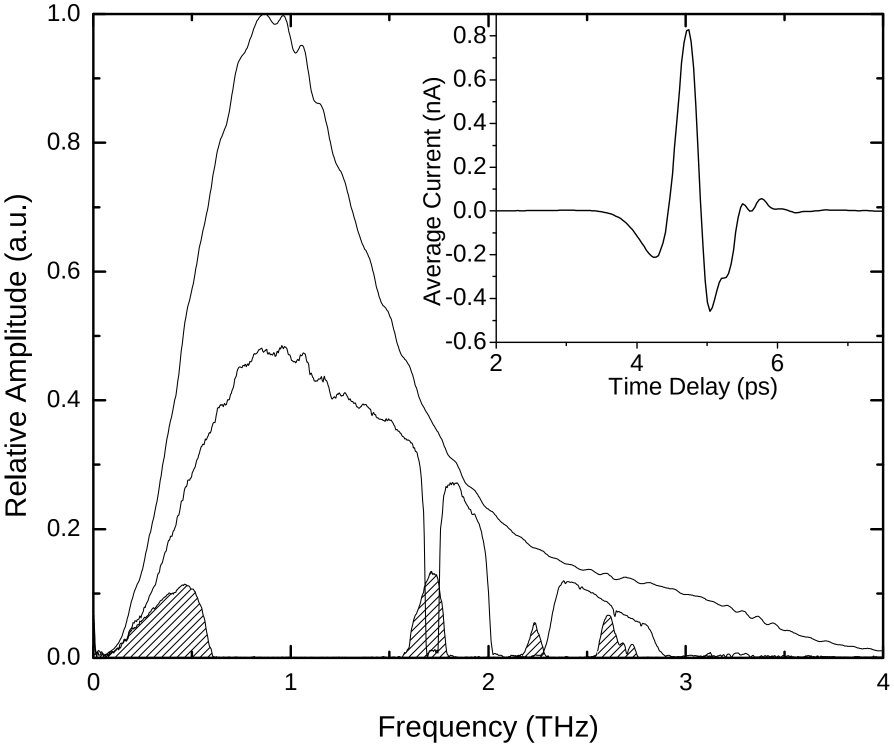

Figure 3-3 - Normalized amplitude spectra from the reference (upper curve) and sample pulses. The middle spectrum is from the type II photonic waveguide and the shaded spectrum is from the type I photonic waveguide. Inset: Reference THz pulse [32].

A complete view of the measurements is shown in Figures 3.4 and 3.5. Fig. 3.4a shows the THz pulse transmitted through the type I photonic waveguide; four output pulses were averaged to improve the signal to noise ratio (SNR). The measured pulse extends to 130 ps, but has been truncated for purposes of illustration. Fig. 3.4b shows the amplitude spectrum of the entire pulse, and Fig. 3.4c shows corresponding power transmission in dB. Fig. 3.5a shows the average of 4 output pulses from the type II photonic waveguide. The type II photonic waveguide output pulse had a shorter ringing structure of only 100 ps, and Fig. 3.5a shows a truncated version of the pulse. Fig. 3.5b shows the amplitude spectrum of the entire pulse, and Fig. 3.5c shows the power transmission T (ω) in dB. All of the output spectra are normalized to the reference spectrum. The power transmission in dB is given by equation 3.1,

$$T(\omega) = 20\log\left|\frac{S(\omega)}{R(\omega)}\right| \tag{3.1}$$

where S (ω) is the sample spectrum and R (ω) is the reference spectrum shown in Figure 3.3.

Fig. 3.4b shows a particularly wide bandgap, from 0.6 to 1.55 THz, with a transmission contrast of 50 dB. Well resolved 50 dB transmission peaks are also observed, illustrating the effectiveness and filtering potential of the type I waveguide. In contrast to these observations the highly transmissive narrow band-reject capability of the type II waveguide is shown in Figures 3.5b and 3.5c. The observed band rejection has a contrast of approximately 30 dB. However, the very sharp Bragg rejection resonance at 1.692 THz is reproducible, with a linewidth of 10 GHz which is limited by the scan length, and a dynamic range of 40 dB.   This resonance is a result of in-phase Bragg reflections from the periodic rows of holes perpendicular to the THz propagation direction shown in the type II surface in Figure 3.1. The 177.3 μm wavelength corresponding to 1.692 THz is approximately equal to the Bragg wavelength of 173.2 μm, twice the 86.6 μm separation between the adjacent hole lines. The loss over the transmitted portion of the spectrum is very acceptable for the type II photonic waveguide, with less than 15 dB loss out to 3 THz despite the large perturbation to the bottom plate of the waveguide. The pulse from the type I photonic waveguide broadens significantly due to highly dispersive propagation characteristic of such sharp frequency-domain features. While both photonic waveguides are dispersive, for the type II photonic waveguide, the frequencies below 1.5 THz arrive in the main peak of the transmitted pulse, and arrive with little delay. The higher frequency components are dispersed, and follow in the ringing structure. Essentially, the type II waveguide acts as an ordinary PPWG for low frequencies, with filtering at the high frequencies. In contrast, the type I waveguide transmitted pulse shows an 11.9 ps time delay relative to the type II waveguide, with dispersion across the transmitted bandwidth and a corresponding much longer ringing structure.

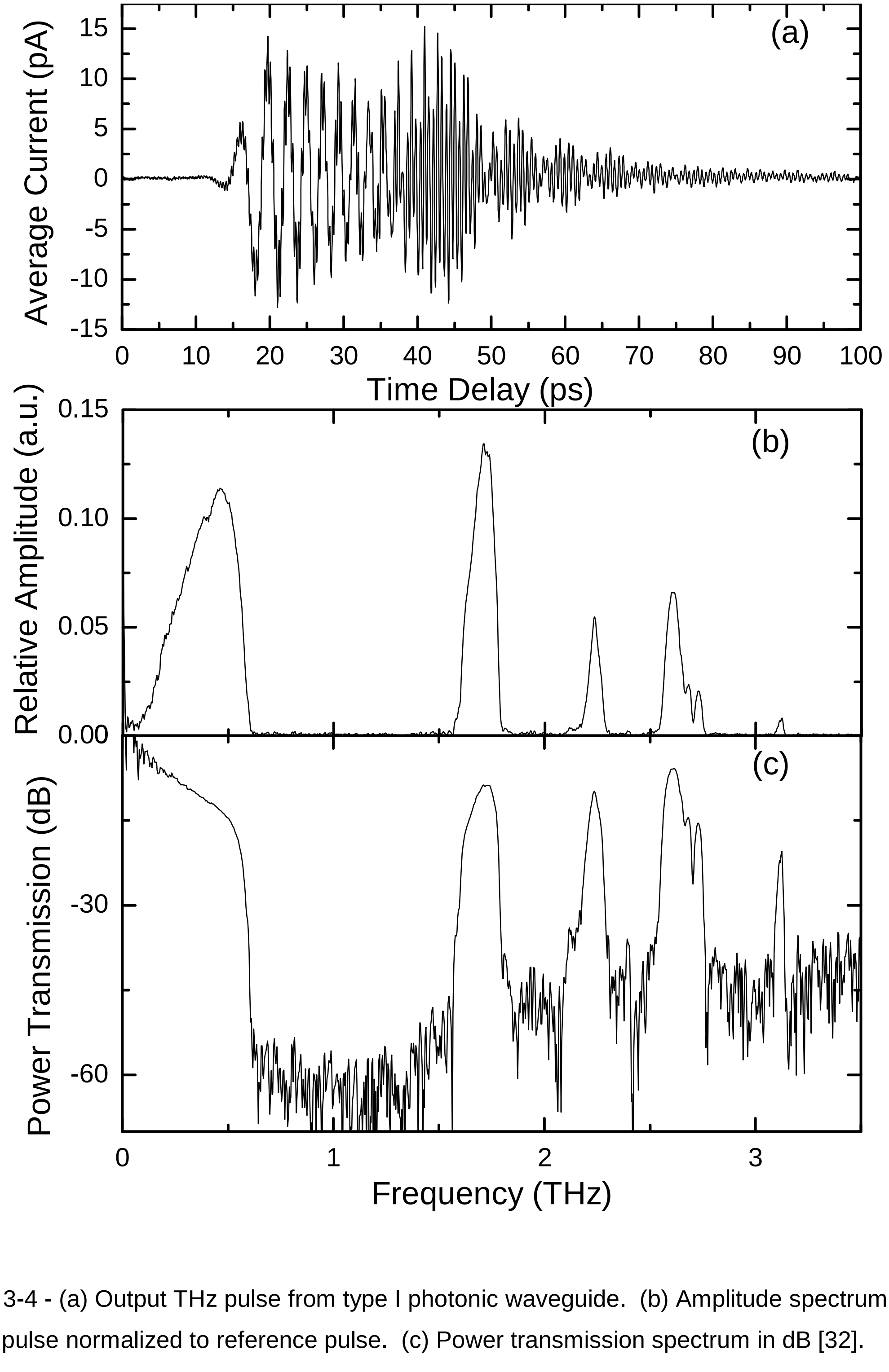

Figure 3-4 - (a) Output THz pulse from type I photonic waveguide. (b) Amplitude spectrum of output pulse normalized to reference pulse. (c) Power transmission spectrum in dB [32].

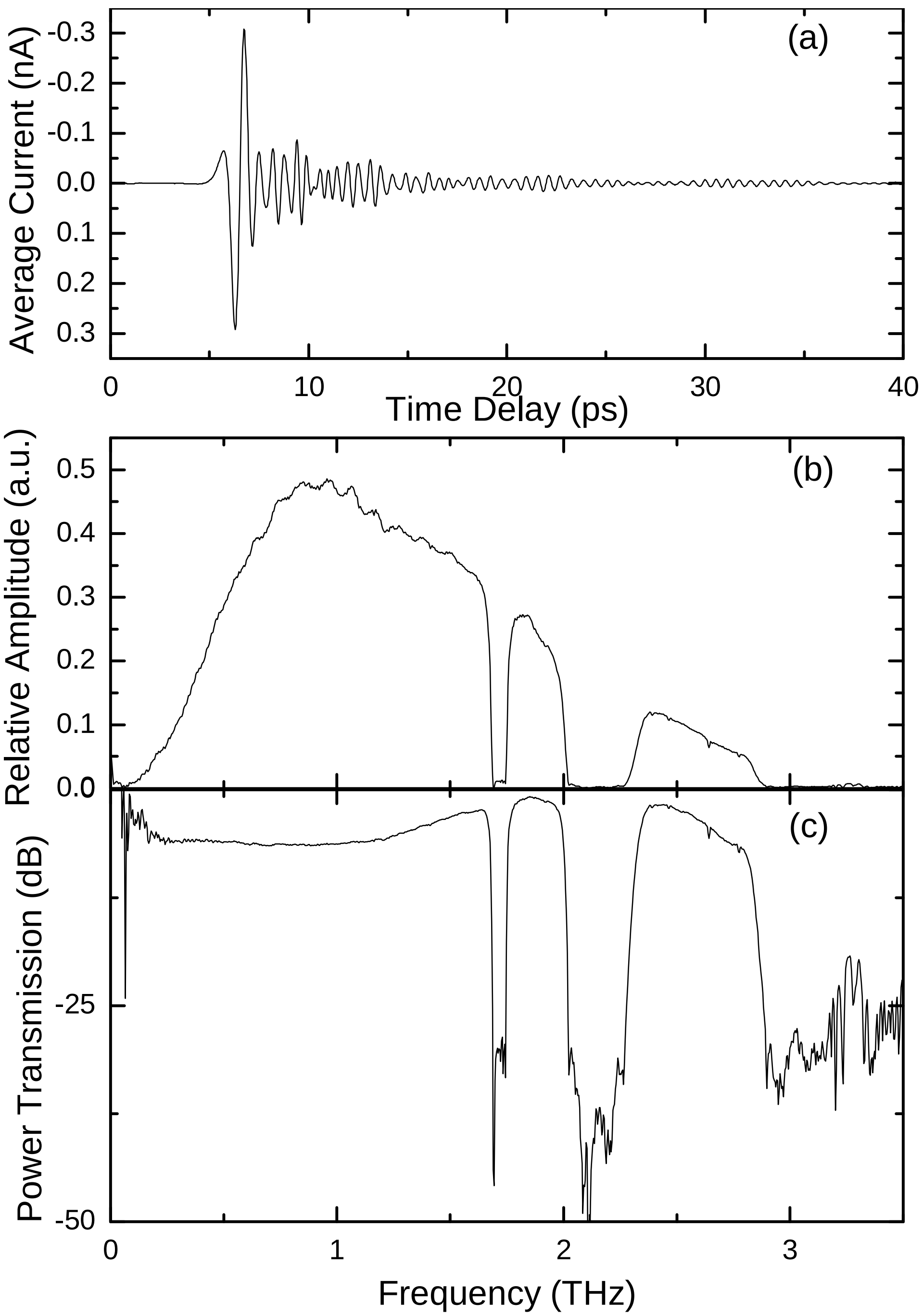

Figure 3-5 - (a) Output THz pulse from type II photonic waveguide (b) Amplitude spectrum of output pulse normalized to reference pulse. (c) Power transmission spectrum in dB [32].

3.2 From 2-D to 1-D Photonic PPWGs

The results from the 2D photonic waveguides were excellent in terms of terms of their very large stopbands, and their clean spectral regions with no frequency-domain interference that has been indicative of multi-mode propagation in previous waveguide experiments [3]. The lack of multimode interference suggest that only the TEM-like mode is coupling out of the waveguide, which is remarkable considering the large perturbations and 170 μm plate spacing at some points in the 2D photonic waveguides. In terms of dynamic range and varying bandwidths, the 2D photonic waveguides are among the best filters that have been demonstrated at THz frequencies. To gain design control over our future waveguide surfaces, and physical insight into the stopband formation, it was necessary to theoretically calculate the transmission of these 2D photonic waveguides.

As with most waveguide problems, the first step was to look to the past for an analytic solution. Similar structures have been demonstrated at microwave frequencies over 50 years ago in so-called ‘Waffle-Iron’ filters [35-46]. These filters had both similar geometry and performance to photonic waveguides demonstrated here. Some demonstrated 60 dB stopbands over 10 GHz bandwidths [42]. The theoretical calculations locating the stopbands were based on equivalent circuit theory [47], treating each perturbation as an equivalent circuit element, and determining the transmission. This would be an ideal way to determine the transmission for the 2-D photonic waveguides, however, the equivalent circuit theory was based upon approximations where the structures are completely single-mode, and the wavelength of the radiation is typically much greater than the component size of the filters. In our case, the 70 μm tall pillars and holes are approximately equal to the wavelengths of radiation demonstrated here, preventing the accurate application of the microwave-theory approximations. A picture of a selection of 'Waffle-Iron' filters is shown in Figure 3.6, illustrating their similarity to the 2-D photonic waveguides.

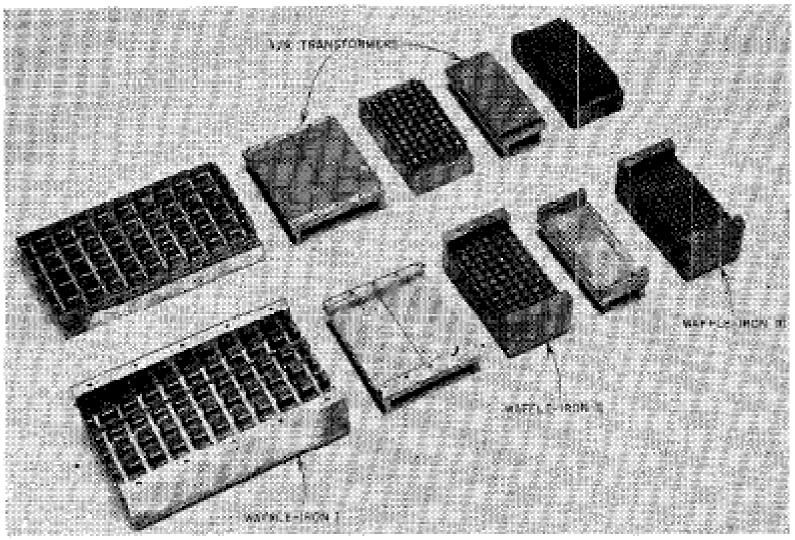

Figure 3-6 - A variety of Microwave Waffle Iron filters [42]

Numerical modeling was also considered as a means to theoretically calculating the transmission spectrum, and programs utilizing finite-difference time-domain (FDTD) and finite element method (FEM) were researched [48]. Unfortunately, the computational geometry required to accurately model the 2-D photonic waveguides was 3-D, and therefore the use of numerical methods was deemed both too time consuming and too complex to fully simulate such a large structure. As such, simplifications were made to the photonic waveguide design. First the dimensions of periodicity were reduced from two to one, which reduced the geometry to a series of PPWGs, which reopened the doors to an to an analytic method. Second, the perturbed section of the waveguide was reduced, dramatically shortening both the programming and calculation time of any numerical methods.

3.3 1-D Photonic PPWGs

The 1D photonic waveguide experiments shown in this section are similar experimentally to the 2D photonic waveguides shown in section 3.1. Figure 3.7 shows an SEM image of a sample 1D photonic chip. A diagram of a 1-D photonic waveguide which is very similar to the waveguides shown in section 3.1 is shown in Figure 3.8. Note that the cylinders of Figure 3.2 have been replaced with 1-D trenches in Figure 3.8.

One significant change between the 1D and 2D geometries is that the 1D geometry allows the simple introduction of defects into the periodic lattice which create a resonant cavity [13,16]. Defects of course allow a resonant frequency to build up inside the cavity, and are capable of generating extremely sharp linewidths. Such sharp resonances are currently of great interest in many sensor technologies which sense trace amounts of chemicals based on small shifts in the resonant frequency. Similar structures have already been demonstrated as DNA sensors in THz microstrip lines [48].

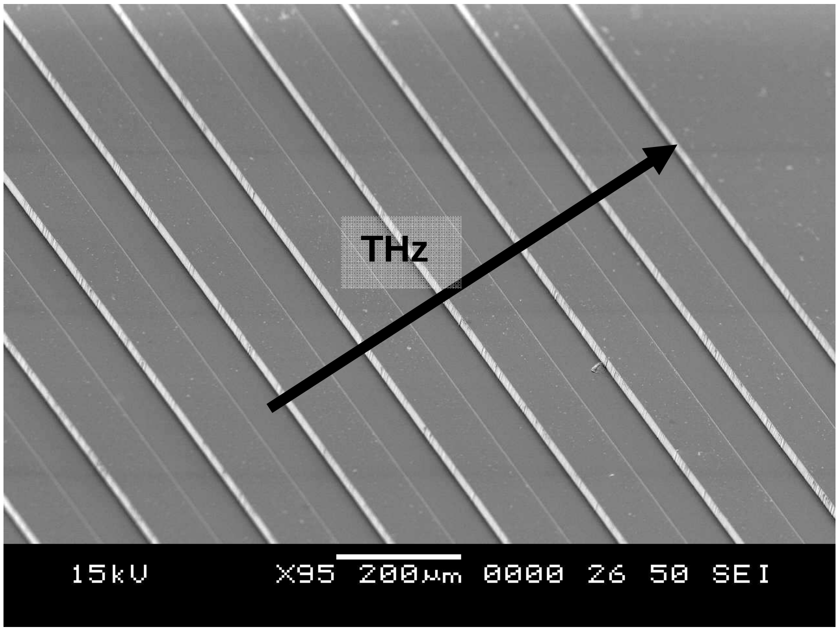

Figure 3-7 - SEM image of 1-D photonic waveguide surface. The period of the trenches is 160 µm; the trenches are 75 µm wide and 30 µm deep. The direction of THz propagation relative to the trenches is shown by the arrow.

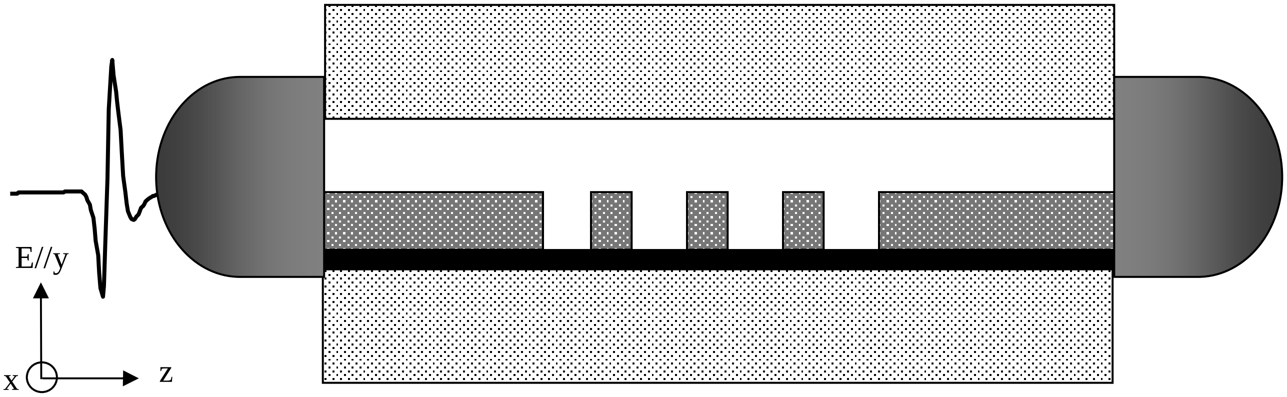

Figure 3-8 - Diagram of 1-D photonic waveguide. The THz pulse is polarized in the y direction for maximum transmission.

The 1-D grating structures were prepared using the same method that has been detailed in Chapter 2, with only minor additional processing steps to limit the pattern to 17 periods. An SEM image showcasing the defect that will form a resonant cavity is shown in Figure 3.9a. The grooves shown in Figure 3.9a are 75 μm wide by 20 μm deep and extend the full 30.0 mm width of the chip. The corresponding plateaus are 85 μm wide. Two different 25.4 mm x 30.0 mm chip geometries were fabricated; chip 17L, with 17 centered, identical grooves and the defect chip 17LD with 17 grooves, where the defect is that the width of the center groove has been doubled. The black rectangles represent the trenches. As shown in Figure 3.9d, the 2.64 mm long grooved section is centered on each chip and is bounded by 11.38 mm of flat metal on each side. The metallized chips were then inserted into the matched aluminum PPWG, covering the entire bottom plate. Before testing the two 1D photonic waveguides, an equivalent bare Si reference chip was metallized with 400 nm of Au and was inserted into the Al PPWG to be used as the reference waveguide. The chips were separated from the upper plate of the waveguide with metal spacers maintaining a 100 μm air gap, and placed into the THz-TDS setup.

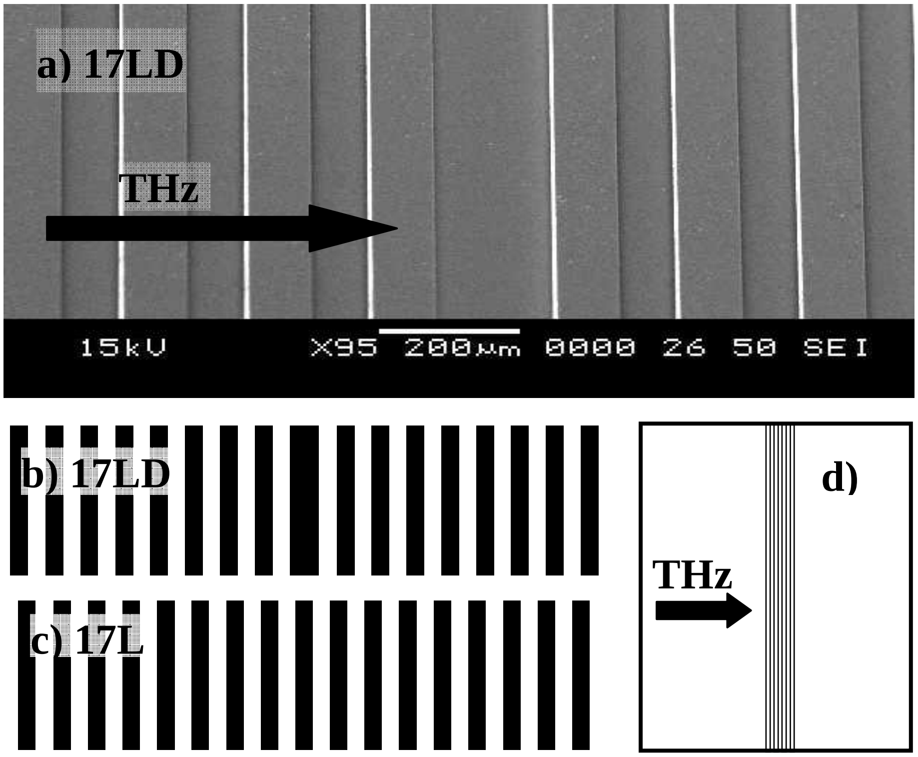

Figure 3-9 - Figure 1 – a) SEM picture of the grooved structure with center defect of chip 17LD. The period is 160 μm, the groove width is 75 μm, and the center groove defect width is 150 μm. b) Schematic of 17 period pattern with defect, chip 17LD. c) Schematic of 17 period pattern, chip 17L. The 20 μm deep grooves are shown in black. d) Chip Layout [33].

The average of four THz output pulses from WG-17L, and WG-17LD are shown in Figures 3.10a and 3.11a. Inset in each figure is the ringing structure following the main pulse which clearly continues beyond 80 ps. Although the measured pulses shown in Figures 3.10a and 3.11a have been truncated at 80 ps to eliminate the multiple reflections between the grooved section of the waveguide and the Si lenses, the experimentally determined linewidths were obtained from pulse measurements extending to 150 ps. Figure 3.10b shows the spectra of the reference pulse, and the 17L pulse. Inset in Figure 3.10b is the measured THz reference pulse through the reference waveguide. Figure 3.11b shows the same reference pulse spectrum with that of the 17LD pulse. The spectra for the reference, 17L, and 17LD pulses were calculated after zero-padding their respective 80 ps time-domain pulses to 160 ps. The defect resonance from the 150 ps scan is shown inset in Figure 3.11b. Note the additional ringing has both strengthened and sharpened the resonance.

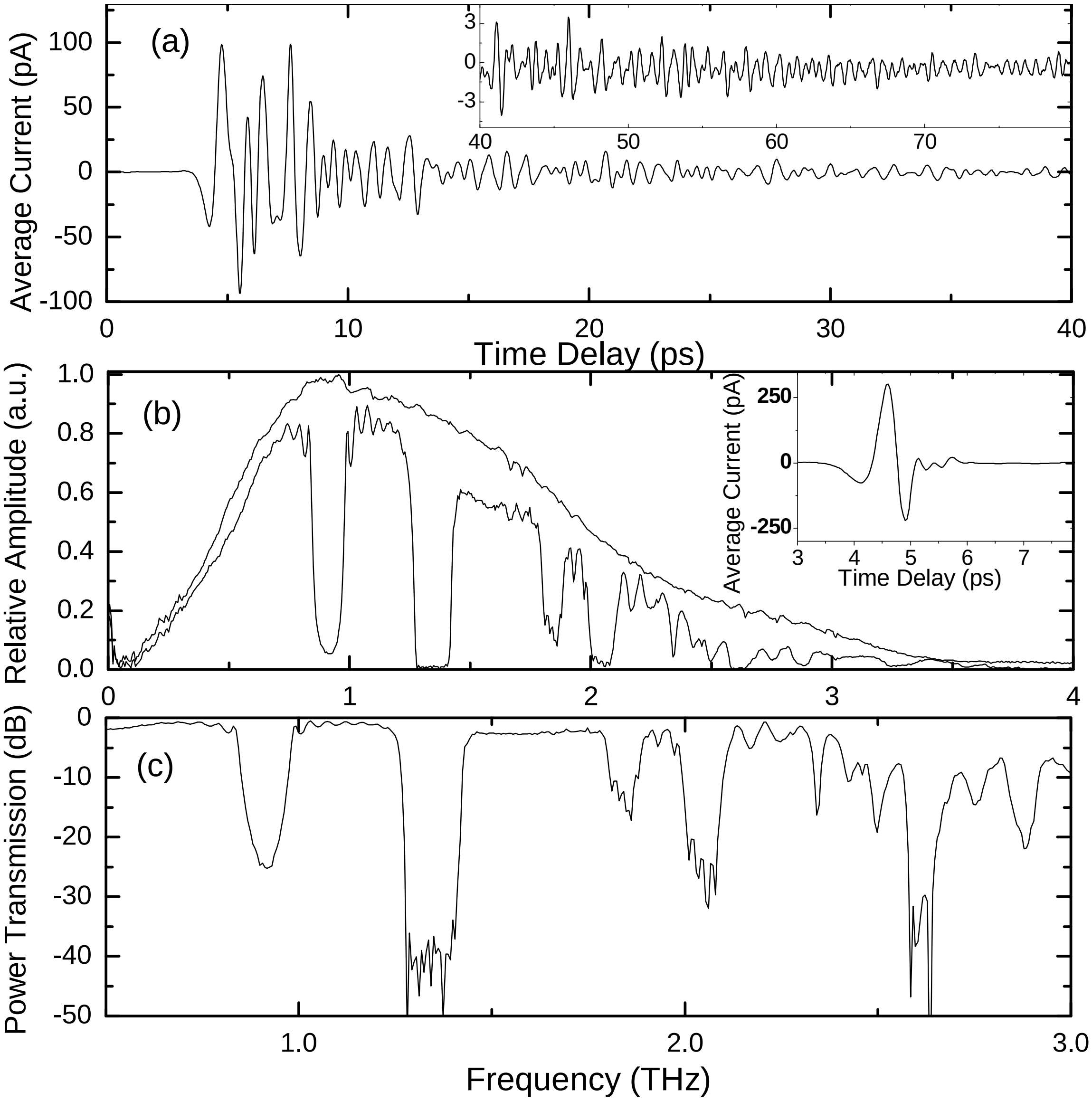

Figure 3-10 – (a) Output THz pulse from WG-17L. Inset: Remainder of pulse ringing. (b) Normalized amplitude spectra from 0 to 4 THz of the reference (upper curve), and 17L pulses. Inset: Reference THz pulse. (c) Power transmission spectrum in dB [33].

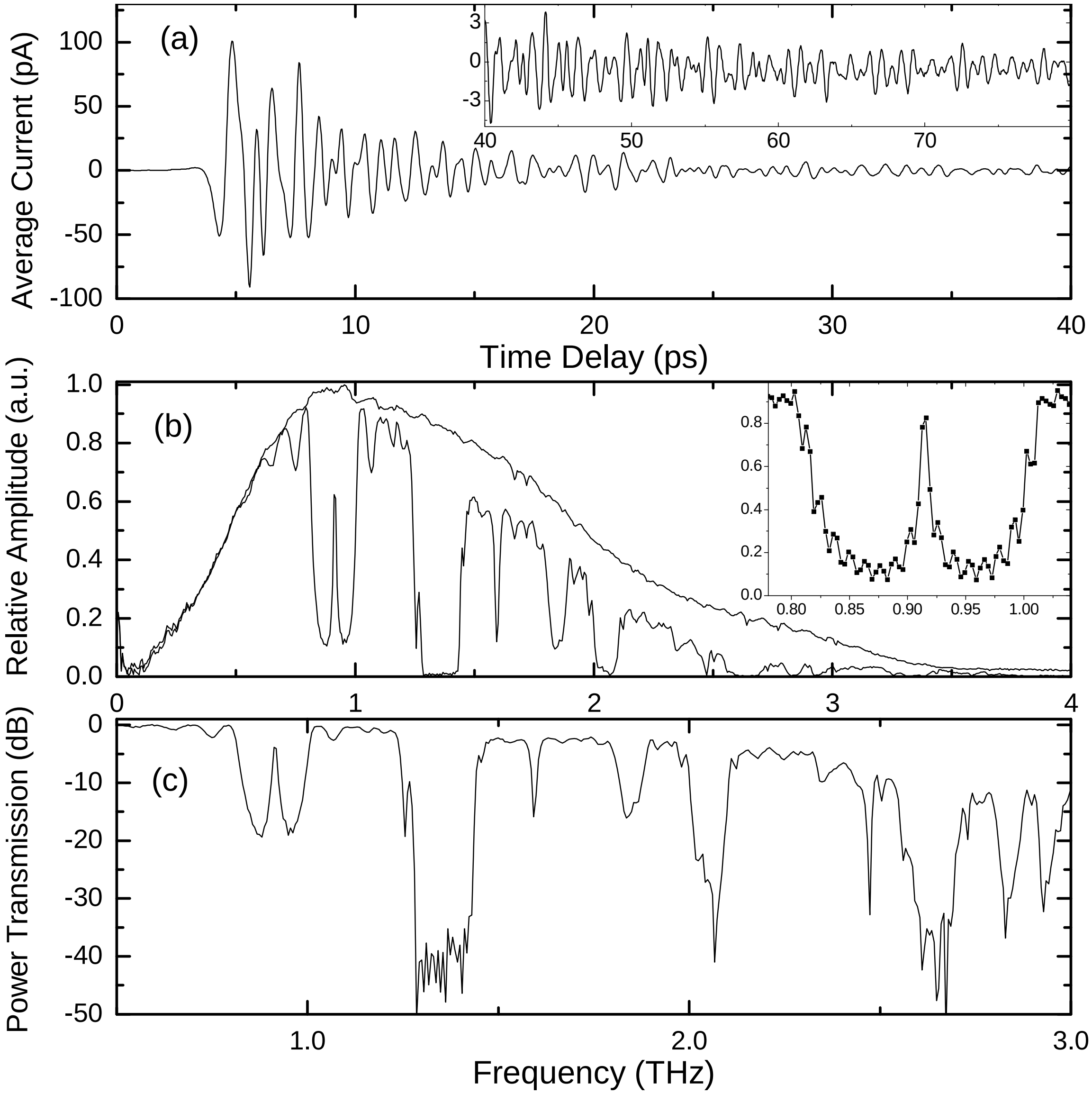

Figure 3-11 – (a) Output THz pulse from WG-17LD. Inset: Remainder of pulse ringing. (b) Normalized amplitude spectra from 0 to 4 THz of the reference (upper curve), and 17LD pulses. Inset: Close-up of resonance from 150 ps scan (c) Power transmission spectrum in dB [33].

There are 5 substantial bandgaps in the region from 0 to 3 THz shown in Figure 3.10c. These bandgaps vary in strength, but the second bandgap (the strongest) is as strong as any of the bandgaps demonstrated for the 2D photonic waveguides with similar sharp sidewalls, and was created with a significantly less perturbed waveguide geometry. While the bandgaps in the transmitted spectra of the 17L and 17LD photonic waveguides overlap, there are some significant differences. The most distinctive difference is the large defect resonance in the middle of the first bandgap in the WG-17LD spectrum. The second major difference is the sharp resonance at 1.64 THz, that is not present in the WG-17L spectrum. These resonances directly result from the doubling of the width of the center trench in WG-17L. In Figures 2c and 3c, the experimental power transmission in dB is shown. The peak dynamic range of the bandgaps is approximately 40 dB.

It is worth noting that because the TEM mode propagation of the PPWG is mathematically equivalent to free space propagation, a comparison can be made with dielectric stack filters, which have been demonstrated for freely propagating THz pulses [21]. These structures demonstrated periodic stopbands due to Bragg reflection, characteristic of 1D photonic crystals. By inserting air-defect layers, defect resonances with a full width at half maximum (FWHM) as sharp as 1 GHz were theoretically predicted for the 1D photonic crystals. However, the experimental observations were limited to 5 GHz linewidths due to the spectral resolution [21]. These free space 1-D photonic crystals are comparable to the 1D photonic waveguides presented here, as will be shown in Chapter 5, waveguiding effects allow stopbands to form that would not be present in a typical photonic crystal.

The 1D photonic waveguides were able to replicate the strong stopbands of the 2D photonic waveguides but with a simpler geometry, much smaller features, and over shorter lengths. Additionally the 1D geometry was amenable to the incorporation of defects, which allowed a sharp resonance to build up in the first stopband. As such the 1D photonic waveguide was judged as a significant step forward over the 2D photonic waveguides. Chapter 4 will detail the derivation of an analytic model to theoretically simulate the 1D photonic waveguides.

Chapter 4 - Theoretical Treatment of Cascaded PPWG Junctions

4.1 Theoretical Approach

The reduction in dimensionality applied to the 1D photonic waveguides demonstrated similar experimental results to the 2D case, but with a simplified geometry. With this simplified geometry in mind, analytically calculating the transmission through a general 1D photonic waveguide is now possible. Reformatting the problem from a periodic boundary to a series of waveguide junctions as illustrated in Figure 4.1 allowed this step to be taken. The natural solution of the problem was to utilize the Mode-Matching method, which has long been used to exactly solve waveguide junction problems [50-58].

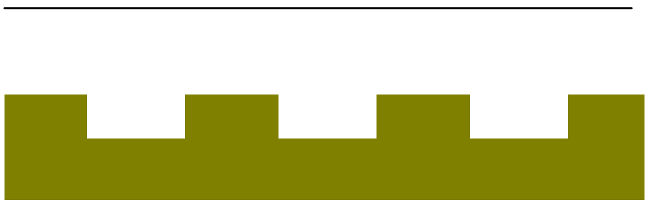

Figure 4-1 - A series of parallel plate waveguide junctions.

A mode incident on the junction of two different waveguides will reflect and transmit into a number of different modes of each waveguide. By summing the modes on each side of the waveguide, and setting the electric and magnetic fields equal to each other at the boundary, the reflection and transmission coefficients for each mode can be calculated.

A single junction, however, is not enough to model the 1D photonic waveguides demonstrated in Chapter 3, which are in actuality made up of repeated junctions of PPWGs. As power is reflected and transmitted into various modes at each junction, it must then propagate with the phase and attenuation of that mode to the next waveguide junction where the process repeats itself. At each junction, power must be conserved, and there must be enough modes taken into consideration to account for any possible excited modes in the spectral bandwidth. This repetitive junction of waveguides has been a popular topic of recent research [59-62]

4.2 Scattering Matrix:

Since the transmission and reflection coefficients of each waveguide mode at a waveguide junction must be kept in order, it is necessary to have a formalism to keep this simple. One such concept, which was borrowed from Network Theory, is the scattering matrix [63]. The scattering matrix is used to determine output quantities at each of the N-ports of a network once the input values to the network are stated. For the case of a waveguide junction, the ports are represented by different waveguide modes. This modal scattering matrix, which determines the output of each mode based on an input to a particular mode or modes. In the calculations that follow, the starting input will always be the TEM mode of our PPWG, but as the THz fields propagate down the waveguide higher order modes will be excited which will in turn be the inputs for later junctions.

The first step is to write out the scattering matrix for a junction of two PPWGs with different plate separations being placed together as shown in Figure 4.2. The A and B coefficients representing the inputs and outputs are labeled in the diagram.

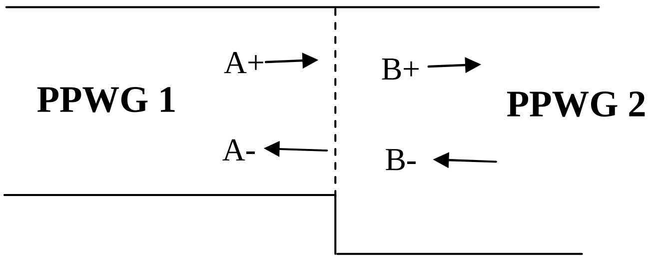

Figure 4-2 - Junction of two parallel plate waveguides

The Scattering Matrix of this junction is represented through the matrix equation as:

$$\begin{bmatrix} A- \\ B+ \end{bmatrix} = \begin{bmatrix} S_{11} & S_{12} \\ S_{21} & S_{22} \end{bmatrix} \begin{bmatrix} A+ \\ B- \end{bmatrix}$$

where the A and B coefficients are the mode amplitudes of the reflected and transmitted portions of the fields at the junction. Each of the A and B coefficients are actually 1 x N vectors denoting the mode amplitude for each mode that can be scattered at the junction. Equivalently, each element of the Scattering Matrix

S_{mn} is actually an N x N matrix. If we have N modes that can be excited by this junction, than equation 4.1 can also be written as:

$$\begin{bmatrix} A_1 - \\ \vdots \\ A_N - \\ B_1 + \\ \vdots \\ B_N + \end{bmatrix} = \begin{bmatrix} S_{11}^{11} & \dots & S_{1N}^{11} & S_{11}^{12} & \cdots & S_{1N}^{12} \\ \vdots & \ddots & \vdots & \vdots & \ddots & \vdots \\ S_{N1}^{11} & \cdots & S_{NN}^{11} & S_{N1}^{12} & \cdots & S_{NN}^{12} \\ S_{11}^{21} & \cdots & S_{1N}^{21} & S_{11}^{22} & \cdots & S_{1N}^{22} \\ \vdots & \ddots & \vdots & \vdots & \ddots & \vdots \\ S_{N1}^{21} & \cdots & S_{NN}^{21} & S_{N1}^{22} & \cdots & S_{NN}^{22} \end{bmatrix} \begin{bmatrix} A_1 + \\ \vdots \\ A_N + \\ B_1 - \\ \vdots \\ B_N - \end{bmatrix}$$

While this is a much more cumbersome form to write out, the utility of the Scattering Matrix becomes clear after writing out one equation from this system of equations:

$$A_1^- = S_{11}^{11} A_1^+ + S_{12}^{11} A_2^+ + \cdots + S_{1N}^{11} A_N^+ + S_{11}^{12} B_1^- + S_{12}^{12} B_2^- + \cdots + S_{1N}^{12} B_N^-$$

The reflected mode amplitude A_n^- is the sum of the incident mode amplitudes A_n^+ multiplied by the scattering coefficients S_{1N}^{11}, in addition to the corresponding B_n^- terms. These scattering coefficients denote the scattering/coupling from the lowest order mode 1 into all other N modes at the junction. The application of the Scattering Matrix to the Mode-Matching Method is shown next.

4.3 Mode-Matching Method:

The Mode-Matching Method is the most complete method for exactly solving waveguide junction problems. The general direction of the following derivation for the mode matching technique follows from [55]. The electric and magnetic fields in each waveguide are set equal to one another via the boundary conditions over the interface. The geometry in question is shown in Figure 4.3.

Two PPWGs with different plate separations are placed in contact. PPWG 1 has a plate separation of *a*, PPWG 2 has a plate separation of *b*.

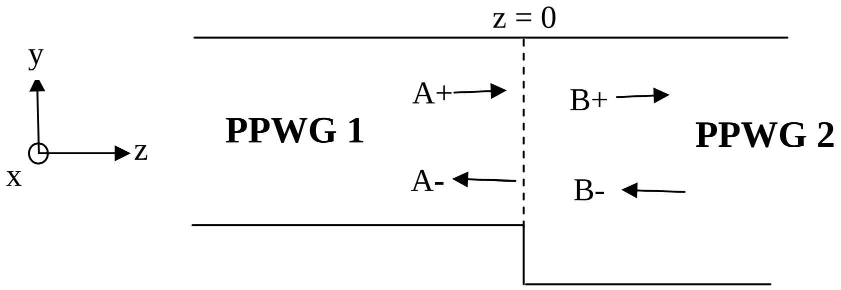

Figure 4-3 – Junction of two parallel plate waveguides.

The tangential fields for PPWG-1 are shown below. The waveguide junction is chosen to be centered at z = 0, which allows the exponential phase factors to equal unity.

$$E_t^1 = \sum_{n=0}^{K} (a_n^+ + a_n^-)\Phi_{1n}\hat{y} \tag{4.1}$$

$$H_t^1 = \sum_{n=0}^{K} (a_n^+ - a_n^-)\frac{\Phi_{1n}}{Z_{1n}}\hat{x} \tag{4.2}$$

E_t and H_t are summed over K modes, Φ_{1n} is the normalized modal field of the waveguide, and Z_{1n} is the frequency dependent impedance of each mode of the waveguide.

$$Z_{1n} = \frac{\omega\varepsilon}{\beta_n} = \frac{\omega\varepsilon}{\sqrt{k^2 - \left(\frac{n\pi}{a}\right)^2}} \tag{4.3}$$

$$\Phi_{1n} = \sqrt{\varepsilon_n / a}\,\cos\left(\frac{n\pi y}{a}\right) \tag{4.4}$$

$$\in_n = \begin{cases} 1 & \text{for} \quad n = 0 \\ 2 & \quad\quad\; n \geq 1 \end{cases} \tag{4.5}$$

where ε_n is Neumann's number, ε is the permittivity of free space, ω is the angular frequency, and k is the wavenumber. The E_t and H_t fields are assumed to be identical in the larger PPWG, with the only changes being the plate spacing which changes from *a* to *b*, and the larger waveguide has a L modes in the summation. As PPWG-2 is larger than PPWG-1, L is therefore greater than K.

At the boundary, the tangential E and H fields of both waveguides are matched by setting them equal to one another.

$$E_t^1 = \sum_{n=0}^{K} (a_n^+ + a_n^-)\Phi_{1n} = \sum_{q=0}^{L} (b_q^+ + b_q^-)\Phi_{2q} = E_t^2 \tag{4.6}$$

$$H_t^1 = \sum_{n=0}^{K} (a_n^+ - a_n^-)\frac{\Phi_{1n}}{Z_{1n}} = \sum_{q=0}^{L} (b_q^+ - b_q^-)\frac{\Phi_{2q}}{Z_{2q}} = H_t^2 \tag{4.7}$$

These fields are equivalent only over the aperture of the waveguide junction, 0 < y < a. More explicitly,

$$\sum_{n=0}^{K} (a_n^+ + a_n^-)\left(\sqrt{\frac{\in_n}{a}}\right)\cos(\frac{n\pi y}{a}) = \sum_{q=0}^{L} (b_q^+ + b_q^-)\left(\sqrt{\frac{\in_q}{b}}\right)\cos(\frac{q\pi y}{b}) \tag{4.8}$$

$$\sum_{n=0}^{K} (a_n^+ - a_n^-)\left(\sqrt{\frac{\in_n}{a}}\right)\cos(\frac{n\pi y}{a})\frac{1}{Z_{1n}} = \sum_{q=0}^{L} (b_q^+ - b_q^-)\left(\sqrt{\frac{\in_q}{b}}\right)\cos(\frac{q\pi y}{b})\frac{1}{Z_{2q}} \tag{4.9}$$

To eliminate the y-dependent cosine terms in the E-field mode matching equation, both sides of (4.8) are multiplied by $\Phi_{2m} = \sqrt{\varepsilon_m / b}\,\cos\left(\frac{m\pi y}{b}\right)$, and then integrated over the waveguide B. This yields

$$\begin{gathered}\int_0^b \sum_{n=0}^{K} (a_n^+ + a_n^-)\left(\sqrt{\frac{\in_n}{a}}\right)\cos\left(\frac{n\pi y}{a}\right)\left(\sqrt{\frac{\varepsilon_m}{b}}\right)\cos\left(\frac{m\pi y}{b}\right)dy = \\ \int_0^b \sum_{q=0}^{L} (b_q^+ + b_q^-)\left(\sqrt{\frac{\in_q}{b}}\right)\cos\left(\frac{q\pi y}{b}\right)\left(\sqrt{\frac{\varepsilon_m}{b}}\right)\cos\left(\frac{m\pi y}{b}\right)dy\end{gathered} \tag{4.10}$$

Rearranging terms,

$$\begin{gathered}\sum_{n=0}^{K} (a_n^+ + a_n^-)\left(\sqrt{\frac{\in_m \in_n}{ab}}\right)\int_0^b \cos\left(\frac{n\pi y}{a}\right)\cos\left(\frac{m\pi y}{b}\right)dy = \\ \sum_{q=0}^{L} (b_q^+ + b_q^-)\left(\sqrt{\frac{\in_m \in_q}{b^2}}\right)\int_0^b \cos\left(\frac{q\pi y}{b}\right)\cos\left(\frac{m\pi y}{b}\right)dy\end{gathered} \tag{4.11}$$

Equation 4.11 can be simplified by using the identities

$$\int_0^x \cos\left(\frac{l\pi y}{x}\right)\cos\left(\frac{k\pi y}{x}\right)dy = \frac{x}{\in_k} \text{ for } k = l \tag{4.12}$$

$$\int_0^x \cos\left(\frac{l\pi y}{x}\right)\cos\left(\frac{k\pi y}{x}\right)dy = 0 \text{ for } k \neq l \tag{4.13}$$

Applying (4.12) and (4.13) to the right side of equation (4.11) yields:

$$\sum_{n=0}^{K} (a_n^+ + a_n^-)\left(\sqrt{\frac{\in_m \in_n}{ab}}\right)\int_0^a \cos\left(\frac{n\pi y}{a}\right)\cos\left(\frac{m\pi y}{b}\right)dy = (b_m^+ + b_m^-) \tag{4.14}$$

Note that the limits of integration on the integral on the left hand side have changed since the field in waveguide A only exists between 0 and *a*, and is zero elsewhere. This relates the mth mode of the b coefficients to the summation of K modes of the a coefficients. But as there are L modes in the larger waveguide (i.e. L total b$^+$ and b$^-$ terms), there are L total equations each with the form of (4.14). To simplify matters, this can be written as a Matrix Equation.

$$M(A^+ + A^-) = (B^+ + B^-) \tag{4.15}$$

Where A^+ and A^- are 1xK column vectors, B^+ and B^- are 1xL column vectors and M is a L x K matrix whose rows m and columns n are defined as:

$$M_{mn} = \left(\sqrt{\frac{\in_m \in_n}{ab}} \right) \int_0^a \cos\left(\frac{n\pi y}{a} \right) \cos\left(\frac{m\pi y}{b} \right) dy \tag{4.16}$$

Equation (4.15) is the E-Field mode matching equation. To derive the H-Field mode matching equation, multiply (4.9) by $\Phi_{1p} = \sqrt{\varepsilon_p / a} \cos\left(\frac{p\pi y}{a} \right)$, and integrate from 0 to *a*. (4.9) then becomes:

$$\begin{gathered} \int_0^a \sum_{n=0}^{K} (a_n^+ - a_n^-) \frac{1}{Z_{1n}} \left(\sqrt{\frac{\in_n}{a}} \right) \cos\left(\frac{n\pi y}{a} \right) \sqrt{\varepsilon_p / a} \cos\left(\frac{p\pi y}{a} \right) dy = \\ \int_0^a \sum_{q=0}^{L} (b_q^+ - b_q^-) \frac{1}{Z_{2q}} \left(\sqrt{\frac{\in_q}{b}} \right) \cos\left(\frac{q\pi y}{b} \right) \sqrt{\varepsilon_p / a} \cos\left(\frac{p\pi y}{a} \right) dy \end{gathered} \tag{4.17}$$

Rearranging terms,

$$\begin{gathered} \sum_{n=0}^{K} (a_n^+ - a_n^-) \frac{1}{Z_{1n}} \left(\sqrt{\frac{\in_p \in_n}{a^2}} \right) \int_0^a \cos\left(\frac{n\pi y}{a} \right) \cos\left(\frac{p\pi y}{a} \right) dy = \\ \sum_{q=0}^{L} (b_q^+ - b_q^-) \frac{1}{Z_{2q}} \left(\sqrt{\frac{\in_p \in_q}{ab}} \right) \int_0^a \cos\left(\frac{q\pi y}{b} \right) \cos\left(\frac{p\pi y}{a} \right) dy \end{gathered} \tag{4.18}$$

Using (4.12) and (4.13), (4.11) becomes:

$$(a_p^+ - a_p^-) \frac{1}{Z_{1m}} = \sum_{q=0}^{L} (b_q^+ - b_q^-) \frac{1}{Z_{2q}} \left(\sqrt{\frac{\in_p \in_q}{ab}} \right) \int_0^a \cos\left(\frac{q\pi y}{b} \right) \cos\left(\frac{p\pi y}{a} \right) dy \tag{4.19}$$

Converting to Matrix Notation, this becomes the H-field mode matching equation:

$$Y_1 (A^+ - A^-) = M^T Y_2 (B^+ - B^-) \tag{4.20}$$

Where the A's and B's are defined as before, Y_1 and Y_2 are the diagonal admittance matrices with diagonal terms $1/Z_{1p}$ (with p counting from 1 to K), and

$1/Z_{2q}$ (with q counting from 1 to L) respectively. M^T is a K x L matrix with row elements p and column elements q elements given by:

$$M_{pq}^{T} = \left(\sqrt{\frac{\in_p \in_q}{ab}}\right)\int_0^a \cos\left(\frac{q\pi y}{b}\right)\cos\left(\frac{p\pi y}{a}\right)dy \tag{4.21}$$

M^T can be shown to simply be the transpose of M.

The Scattering Matrix, consisting of all of the reflection and transmission coefficients of all modes for the waveguide junction is determined from the relationship between the A and B coefficients in the E and H field mode matching equations (4.15) and (4.20). For this case the scattering matrix contains all complex transmission and reflection coefficients for incidence from either side, and from each mode to another. The scattering matrix holds all information regarding the coupling of modes from guide 1, to modes from guide 2. The exact derivation of the scattering matrix will be shown in the next section.

4.4 Scattering Matrix Derivation

To derive the scattering matrix, the matrix forms of the E and H mode matching equations (4.15) and (4.20) are used [55]. To simplify matters incidence is assumed to only be from one direction, i.e. $B^- = 0$, meaning incidence is from the smaller waveguide as shown in Figure 4.3. With this, (4.15) and (4.20) reduce to:

$$M(A^{+}+A^{-})=(B^{+}) \tag{4.22}$$

$$Y_1(A^{+}-A^{-})=M^{T}Y_2(B^{+}) \tag{4.23}$$

(4.22) is then inserted into (4.23) yielding:

$$Y_1(A^{+}-A^{-})=M^{T}Y_2(M(A^{+}+A^{-})) \tag{4.24}$$

With the substitution $Y_x = M^T Y_2 M$, and a little algebra, this becomes:

$$A^{-}=(Y_x+Y_1)^{-1}(Y_1-Y_x)A^{+} \tag{4.25}$$

Which with $B^- = 0$ proves

$$\boxed{S_{11}=(Y_x+Y_1)^{-1}(Y_1-Y_x)} \tag{4.26}$$

since,

$$A^{-}=S_{11}A^{+} \tag{4.27}$$

S_{21} can also be found using the same assumption ($B^- = 0$). This time, $B^+ = S_{21}A^+$, so A^- needs to be eliminated from (4.22) and (4.23). But since S_{11}, has already been derived, (4.27) can be used in conjunction with (4.22) to determine S_{21}. Inserting (4.27) into (4.22),

$$M(A^{+}+S_{11}A^{+})=(B^{+}) \tag{4.28}$$

From this,

$$M(I+S_{11})A^{+}=(B^{+}) \tag{4.29}$$

Where I is a identity matrix with the same dimensions as S_{11}. Therefore,

$$\boxed{S_{21}=M(I+S_{11})} \tag{4.30}$$

Both of these were derived with the assumption that there was only incidence from the left. If the opposite holds, true, ($A^+ = 0$), S_{12} and S_{22} can be derived. This time (4.15) and (4.20) become:

$$M(A^-) = (B^+ + B^-) \tag{4.31}$$

$$Y_1(-A^-) = M^T Y_2 (B^+ - B^-) \tag{4.32}$$

To find S_{12}, B^+ must be eliminated. Solving (4.31) for B^+ and inserting it into (4.32) gives us,

$$Y_1(-A^-) = M^T Y_2 (MA^- - B^- - B^-) \tag{4.33}$$

Collecting like terms,

$$(Y_1 + Y_x)A^- = 2M^T Y_2 B^- \tag{4.34}$$

Where Y_x is as defined previously. Then further rearranging terms, and using the relation from (22) with $A^+ = 0$,

$$A^- = S_{12}B^- = 2(Y_1 + Y_x)^{-1} M^T Y_2 B^- \tag{4.35}$$

$$\boxed{S_{12} = 2(Y_1 + Y_x)^{-1} M^T Y_2} \tag{4.36}$$

Finally S_{22} can be found by plugging in (4.35) into (4.31). Rearranging terms allows us to find:

$$B^+ = S_{22}B^- = (MS_{12} - I)B^- \tag{4.37}$$

$$\boxed{S_{22} = (MS_{12} - I)} \tag{4.38}$$

Thus, all 4 of the scattering submatrices in the larger scattering matrix have been derived. They match the equations found in the literature [55]. After coding the equations into MATLAB, the Scattering Matrix Coefficients can be calculated over a desired range of frequencies. For the waveguide junction shown in Figure

4.3 with a TEM mode normalized to unity power flowing into the junction from the right, the scattering matrix coefficients showing the transmission into the larger waveguide are shown in Figure 4.4. The scattering matrix coefficients showing the reflection into the smaller waveguide are shown in Figure 4.5.

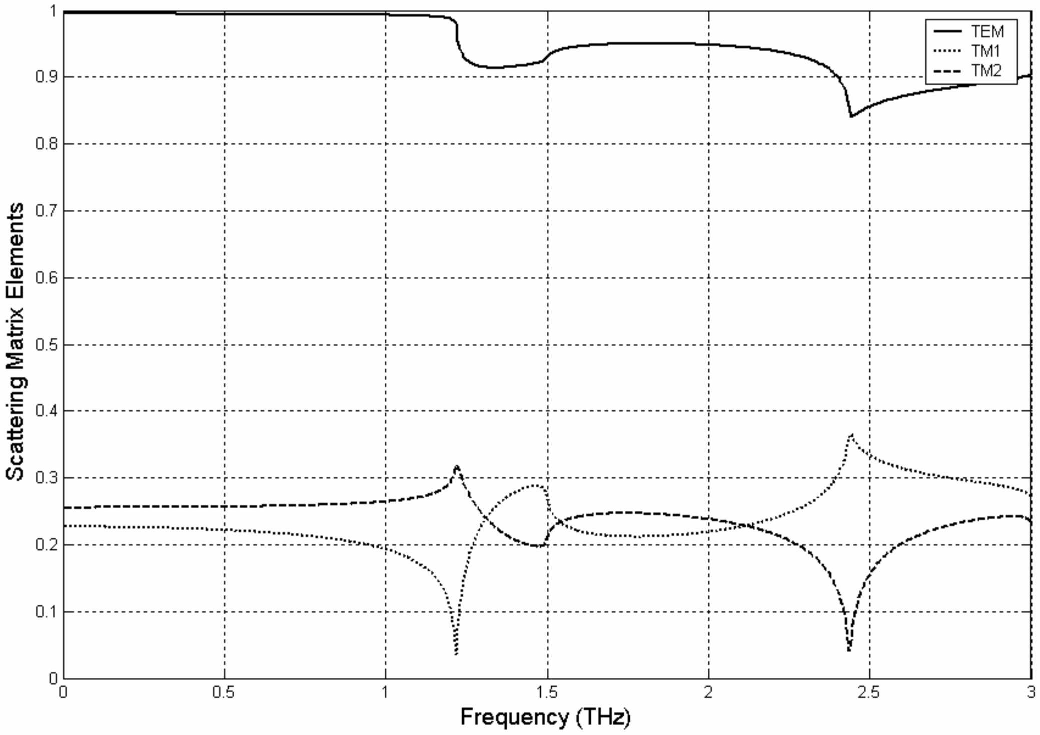

Figure 4-4 - Scattering Matrix Elements for the waveguide junction shown in Figure 4.3. A TEM mode incident from the smaller waveguide excites the TEM, TM_1, and TM_2 modes of the larger waveguide.

The transmission scattering coefficients shown in Figure 4.3 shows the TEM mode of the smaller waveguide couples strongly to the TEM mode of the larger waveguide, as expected as the fields overlap very well. There is some residual coupling to the TM_1 and TM_2 modes, both of which peak at their respective cut-off frequencies. It should be noted that there is coupling of these higher order modes below their respective cutoff frequencies. While these fields will couple to the larger waveguide due to their modal field overlap with the exciting TEM mode, they are evanescent and will attenuate rapidly once they begin to propagate.

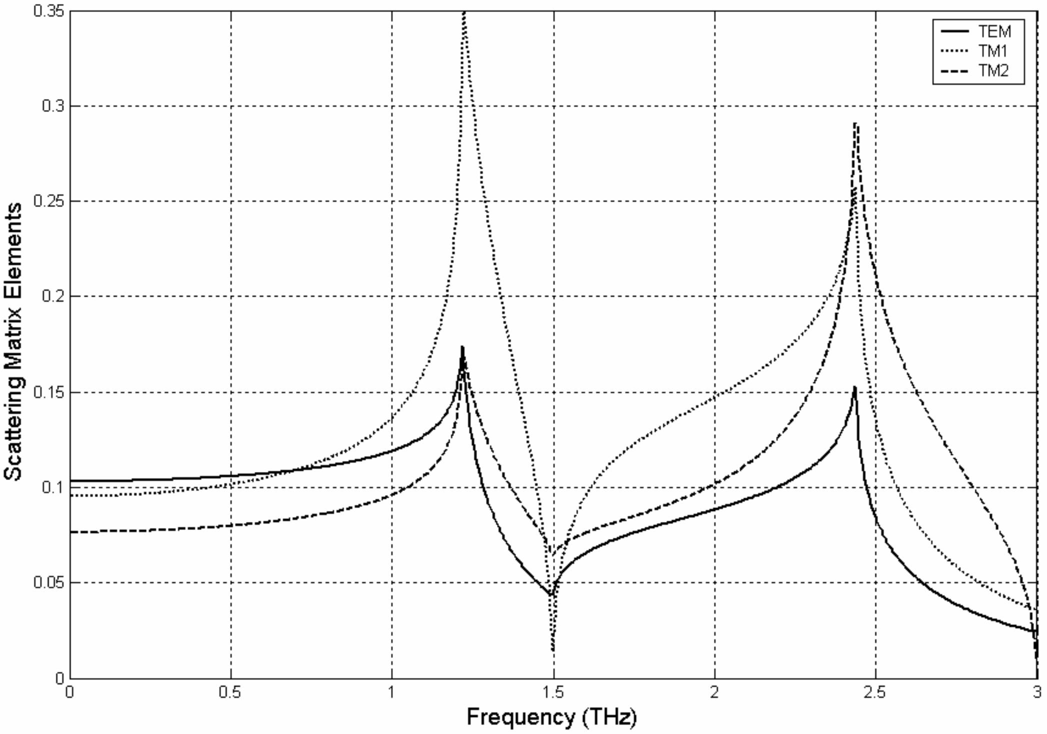

Figure 4-5 - Scattering Matrix Elements for the waveguide junction shown in Figure 4.3. A TEM mode incident from the smaller waveguide reflects at the junction and excites the TEM, TM_1, and TM_2 modes of the smaller waveguide.

Similar behavior is shown for the reflection coupling coefficients for the incident TEM mode reflecting back into the smaller waveguide as shown in Figure 4.5. The TEM mode reflection is relatively small throughout, while the higher order mode reflections then peak upon reaching their cutoff frequencies.

As a check to ensure that the above calculations are correct, a proof of conservation of power for a single junction is shown in Appendix A.

To summarize, a single mode will be incident on the PPWG junction shown in Figure 4.5. The energy in this TEM mode will hit the junction and be both transmitted and reflected into a number of modes. The scattering matrix gives these complex transmission and reflection coefficients. The next section determines what happens to the energy in each of these modes after the junction.

4.5 Propagation Matrices:

The modes that were excited in the previous section will then propagate through the unperturbed section of PPWG in front of them with their respective propagation and attenuation constants [61]. To keep track of the amplitude and phase of the field in each mode, a propagation matrix is used. The new geometry is now shown in Figure 4.6.

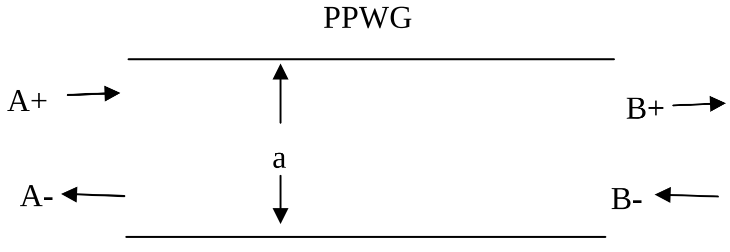

Figure 4-6 – PPWG for construction of Propagation Matrix

The Propagation Matrix for this structure would have the form shown in equation 4.39,

$$\begin{bmatrix} A- \\ B+ \end{bmatrix} = \begin{bmatrix} T_{11} & T_{12} \\ T_{21} & T_{22} \end{bmatrix} \begin{bmatrix} A+ \\ B- \end{bmatrix} \qquad (4.39)$$

Where the A's and B's are again 1 x N vectors denoting the amplitude of each forward and backward propagating mode of the PPWG under consideration. As the fields in each mode are independent of each other, our transmission matrix coefficients will have the form of simple N x N diagonal matrices. Since there is no reflection in the continuous section of PPWG, all the elements of the N x N T_{11} and T_{22} matrices are zero. The elements of T_{12} and T_{21} are equivalent and can be written out as:

$$[T_{12}] = \begin{bmatrix} \exp(-j\beta_1 z) & 0 & \cdots & 0 \\ 0 & \ddots & \ddots & \vdots \\ \vdots & \ddots & \ddots & 0 \\ 0 & \cdots & 0 & \exp(-j\beta_N z) \end{bmatrix} = \begin{bmatrix} \exp(j\beta_1(-z)) & 0 & \cdots & 0 \\ 0 & \ddots & \ddots & \vdots \\ \vdots & \ddots & \ddots & 0 \\ 0 & \cdots & 0 & \exp(j\beta_N(-z)) \end{bmatrix} = [T_{21}]$$

Since there are two different waveguides that the THz will be propagating through, we will need two propagation matrices, one for the waveguide with a smaller plate separation (PPWG 1) and one for the waveguide with a bigger plate separation (PPWG 2). It should be noted that making these propagation coefficients complex will allow the attenuation due to the finite conductivity of the metal to be simulated.

4.6 Cascading Scattering Matrices

When propagating electromagnetic radiation through a thin portion of a dielectric, the multiple reflection and transmissions inside the cavity make it difficult to write the complete transmission and reflection coefficients. Fortunately, the sum of these multiple transmissions and reflections converge easily through a geometric series as shown in the thin film coefficients in Born and Wolf [64].

A series of waveguide junctions present a similar problem as shown in Figure 4.7. Here there are 3 separate portions of parallel-plate waveguide all placed against each other. After the transmission and reflection coefficients for each junction have been found, they can be used in the thin film formulas to get the total transmission through the structure. Another valid method is the cascading of scattering matrices through the structure which will be shown here. This structure will be designated as a single trench for future reference and note that it is a unit cell of the 1-D photonic waveguides.

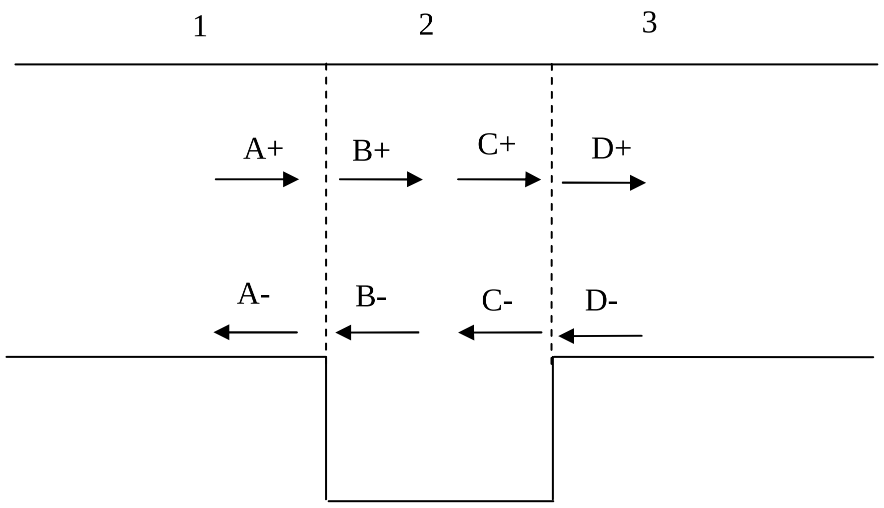

Figure 4-7 – Junction of 3 PPWGs. Single Trench Geometry

For the first junction, from waveguide 1 to waveguide 2 (at the first dotted line), the junction matrices can be written as:

$$\begin{bmatrix} A- \\ B+ \end{bmatrix} = \begin{bmatrix} S_{11}^{1} & S_{12}^{1} \\ S_{21}^{1} & S_{22}^{1} \end{bmatrix} \begin{bmatrix} A+ \\ B- \end{bmatrix} \tag{4.40}$$

But that isn't the only structure shown in Figure 4.7; there is also the unperturbed stretch of Waveguide 2. This requires the introduction of a transmission matrix

$$\begin{bmatrix} B- \\ C+ \end{bmatrix} = \begin{bmatrix} 0 & T_2 \\ T_2 & 0 \end{bmatrix} \begin{bmatrix} B+ \\ C- \end{bmatrix} \tag{4.41}$$

T_2 is a phase term for the propagation across the uniform portion of PPWG 2. For our purposes, $T_2 = e^{-j\beta nd}$, where β_n is the propagation constant of the TM_n mode of the waveguide and d is the length of waveguide section 2.

Finally, there is the second wavguide junction. For the moment, it is assumed that waveguide 2 has been placed in contact with a new waveguide 3, but in reality, waveguides 1 and 3 are the same. For now the general case will be explored. The scattering matrix for the second and final waveguide junction is written as:

$$\begin{bmatrix} C- \\ D+ \end{bmatrix} = \begin{bmatrix} S_{11}^{2} & S_{12}^{2} \\ S_{21}^{2} & S_{22}^{2} \end{bmatrix} \begin{bmatrix} C+ \\ D- \end{bmatrix} \tag{4.42}$$

Now the different scattering matrices must be cascaded together to produce the complete input and output transmission and reflection coefficients for comparison with the thin film coefficients. This is a simple process requiring only matrix algebra, and the fact that it replicates the thin-film formulae for the single mode is remarkable

First, each part of equations (4.40) and (4.41) are written out separately:

$$A^{-} = S_{11}^{1} A^{+} + S_{12}^{1} B^{-} \tag{4.43}$$

$$B^{+} = S_{21}^{1} A^{+} + S_{22}^{1} B^{-} \tag{4.44}$$

$$B^{-} = T_2 C^{-} \tag{4.45}$$

$$C^{+} = T_2 B^{+} \tag{4.46}$$

Next, (4.45) is inserted into (4.43) and (4.44-4.45) is inserted in (4.46). The goal is to write equations for A- and C+. This process yields

$$A^{-} = S_{11}^{1} A^{+} + S_{12}^{1} T_2 C^{-} \tag{4.47}$$

$$C^{+} = T_2 (S_{21}^{1} A^{+} + S_{22}^{1} T_2 C^{-}) = T_2 S_{21}^{1} A^{+} + T_2 S_{22}^{1} T_2 C^{-} \tag{4.48}$$

With that the first two scattering matrices have been combined. The new scattering matrix for the first two sections of the single trench is written as

$$\begin{bmatrix} A- \\ C+ \end{bmatrix} = \begin{bmatrix} S_{11}^{1} & S_{12}^{1} T_2 \\ T_2 S_{21}^{1} & T_2 S_{22}^{1} T_2 \end{bmatrix} \begin{bmatrix} A+ \\ C- \end{bmatrix} \tag{4.49}$$

The use of (4.49) would propagate an input mode up to the second waveguide junction. Following the procedure as shown in (4.43)-(4.48), (4.49) is cascaded the scattering matrix for the second junction. After cascading the entire system the scattering matrix for the structure shown in Figure 1 is:

$$\begin{bmatrix} A- \\ D+ \end{bmatrix} = \begin{bmatrix} S_{11}^{1} + S_{12}^{1} T_2 (I - S_{11}^{2} T_2 S_{22}^{1} T_2)^{-1} S_{11}^{2} T_2 S_{21}^{1} & S_{12}^{1} T_2 (I - S_{11}^{2} T_2 S_{22}^{1} T_2)^{-1} S_{12}^{2} \\ S_{21}^{2} (I - T_2 S_{22}^{1} T_2 S_{11}^{2})^{-1} T_2 S_{21}^{1} & S_{22}^{2} + S_{21}^{2} (I - T_2 S_{22}^{1} T_2 S_{11}^{2})^{-1} T_2 S_{22}^{1} T_2 S_{12}^{2} \end{bmatrix} \begin{bmatrix} A+ \\ D- \end{bmatrix} \tag{4.50}$$

The equivalency of these results and the complex transmission and reflection coefficients through a thin film are shown in Appendix B. For now, the transmission and reflection scattering matrix coefficients for the first three modes of the waveguides will be shown.

As shown in Figure 4.8, the TEM transmission through a single trench is close to unity over the frequencies shown, with one sharp dip at the cutoff frequency of the TM_1 mode of the larger waveguide. There is a corresponding sharp increase in the scattering matrix coefficient for the transmission into the TM_1 mode, which matches the dip in the TEM transmission. The TEM reflection through from a single trench is shown in Figure 4.9.

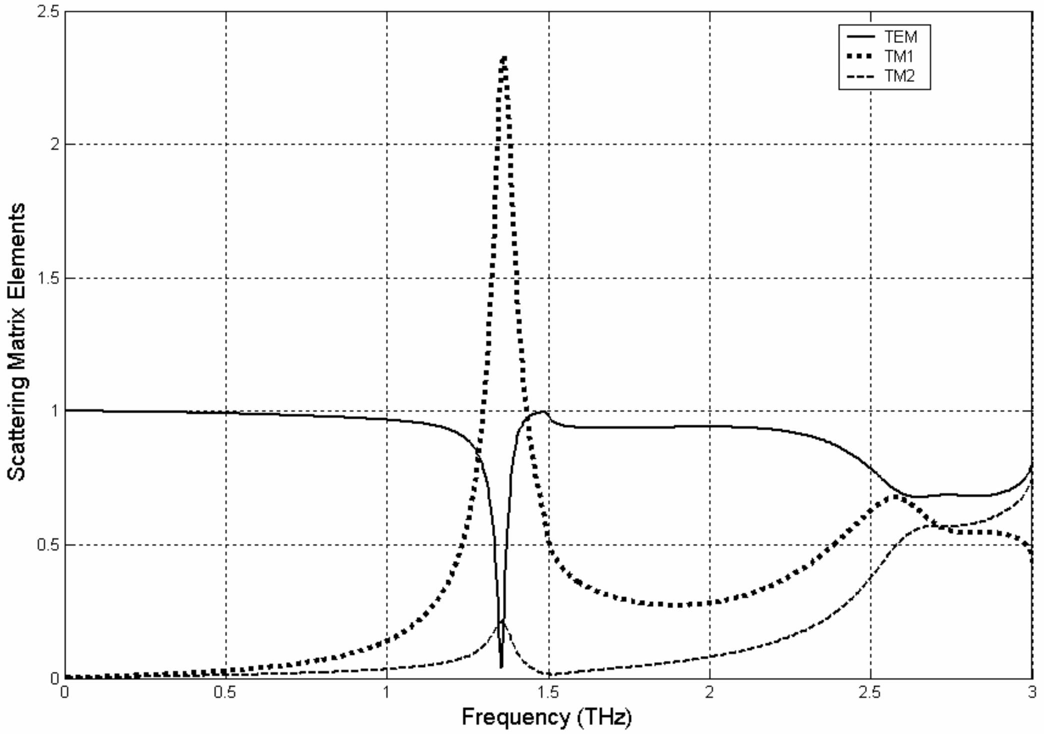

Figure 4-8 - Scattering Matrix Elements for the single trench waveguide junction shown in Figure 4.7. A TEM mode incident from the smaller waveguide reflects at the junction and excites the TEM, TM_1, and TM_2 modes of the smaller waveguide.

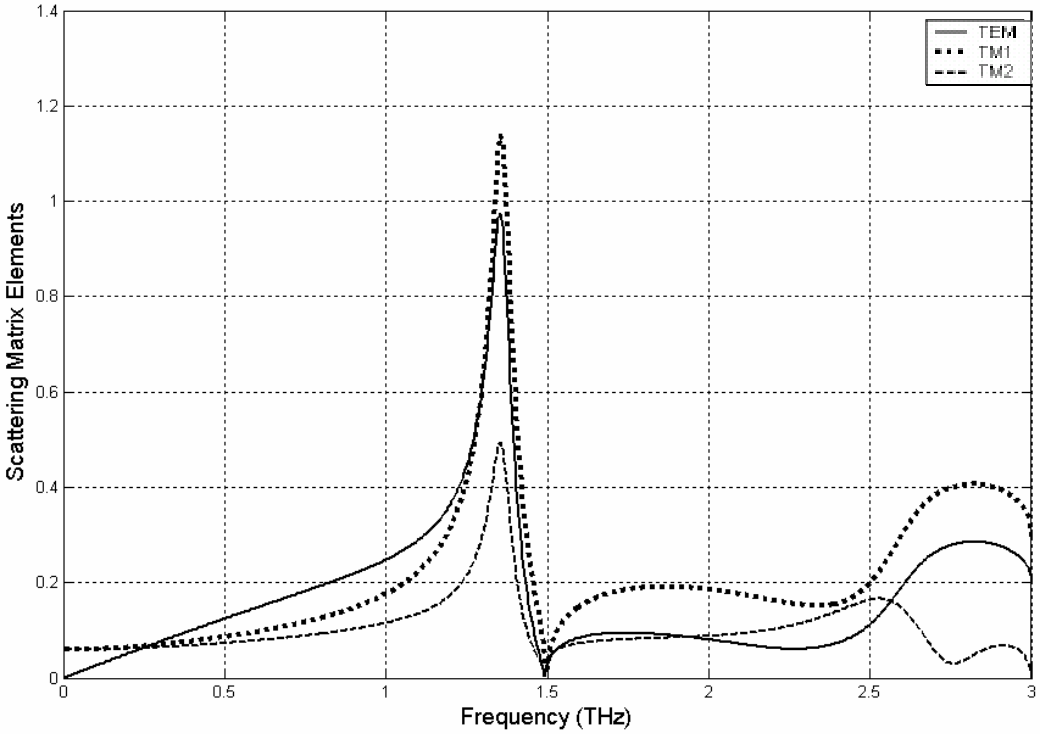

Figure 4-9 - Scattering Matrix Elements for the single trench waveguide junction shown in Figure 4.7. A TEM mode incident from the left reflects at the junction and excites the TEM, TM_1, and TM_2 modes of the smaller waveguide.

4.7 Propagation through an N-Junction PPWG

Now that it is known that cascading scattering matrices properly accounts for multiple reflections, the scattering matrix for a system of waveguide junctions can be calculated. Previous authors have used a star symbol '*', to symbolize the cascading process illustrated in equations (4.43)-(4.49). First introduced by Redheffer in 1961 [65], it is sometimes called the Redheffer Star Product.

A complete unit cell for the 1-D photonic waveguide structure is shown in Figure 4.10.

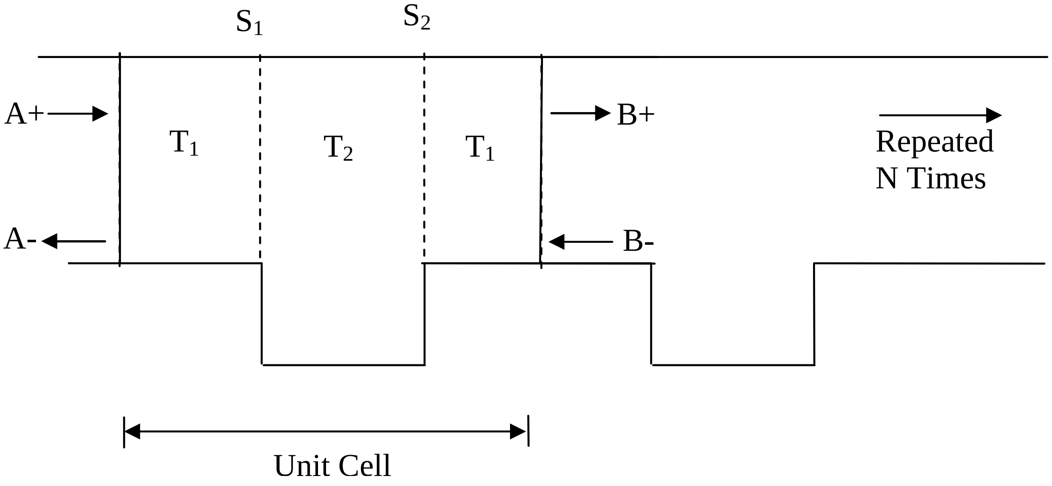

Figure 4-10 – Unit Cell for N-Junction PPWG

Using the star product notation, the total transfer matrix for the single unit cell can be written as:

$$U = T_1{*}S_1{*}T_2{*}S_2{*}T_1 \tag{4.51}$$

In terms of the inputs and outputs,

$$\begin{bmatrix} A- \\ B+ \end{bmatrix} = \begin{bmatrix} U_{11} & U_{12} \\ U_{21} & U_{22} \end{bmatrix} \begin{bmatrix} A+ \\ B- \end{bmatrix} \tag{4.52}$$

where the values for the components of the transfer matrix U are given in equation (4.50). For the complete picture, the transfer matrix U of a unit cell simply needs to be cascaded N times,

$$U_{total} = U{*}U{*}U{*}U{*}\ldots{*}U \quad \text{(N times)} \tag{4.53}$$

Our final amplitude equation is then:

$$\begin{bmatrix} A- \\ B+ \end{bmatrix} = \begin{bmatrix} U_{11}^{total} & U_{12}^{total} \\ U_{21}^{total} & U_{22}^{total} \end{bmatrix} \begin{bmatrix} A+ \\ B- \end{bmatrix} \tag{4.54}$$

which allows the problem to be described as a black box as shown in Figure 4.11

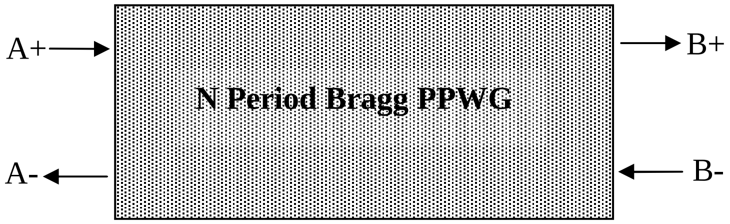

Figure 4-11 – Black Box Representation of N-Period Bragg PPWG Problem and coefficients.

This analysis yields the transmission and reflection coefficients for any N-Period 1-D photonic waveguide demonstrated in Section 3.4. By placing the appropriate values for plate spacing, trench depth, trench width, and the number of trenches, we can calculate the scattering matrix elements for the 17-period 1-D photonic waveguide from Figure 3.11. By applying the parameters for the 1-D photonic wavgeuides demonstrated in Chapter 3, the scattering matrix transmission and reflection coefficients for the TEM, TM_1 and TM_2 modes were calculated, and are shown in Figures 4.12 and 4.13.

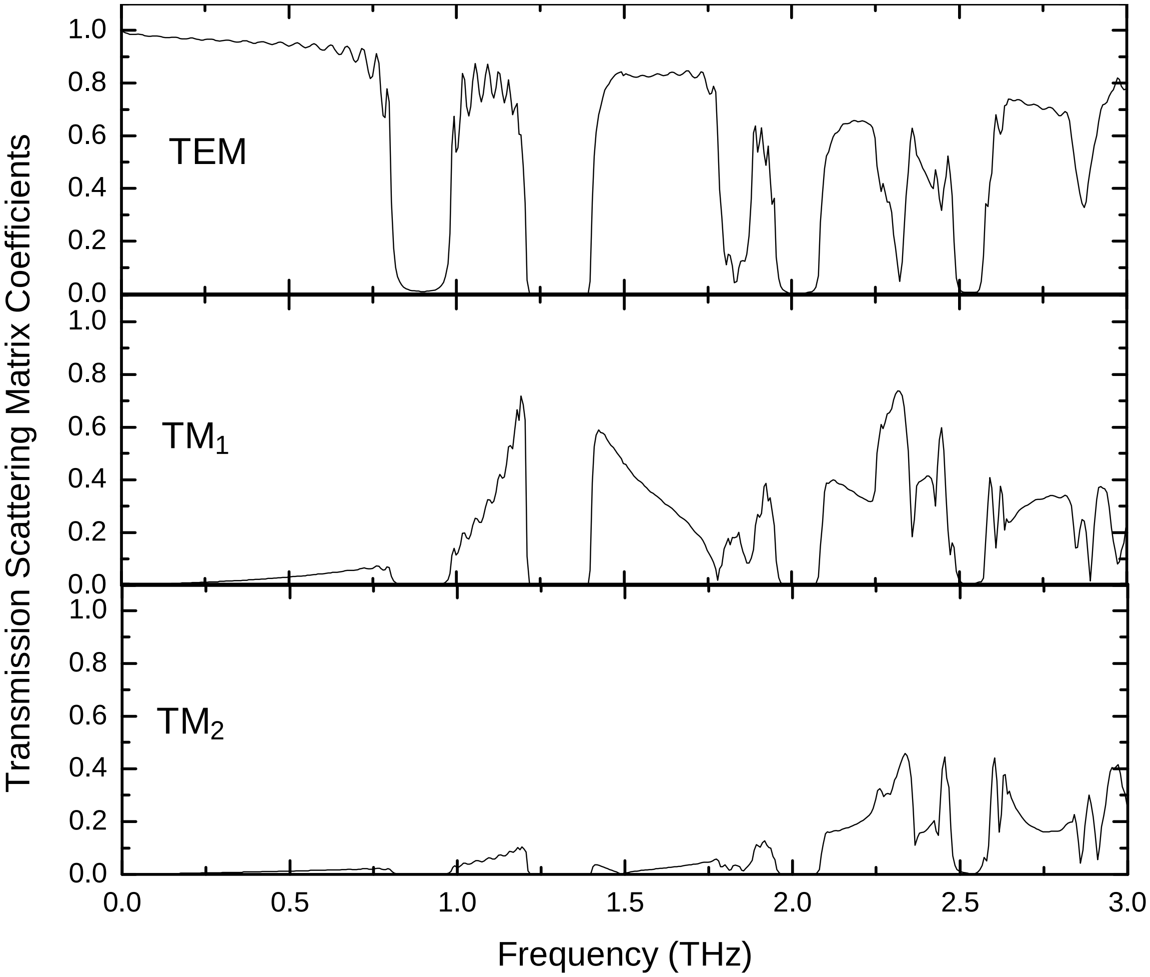

Figure 4-12 - Scattering Matrix Elements for the 17-period 1-D photonic waveguide. Each mode is shown separately for clarity.

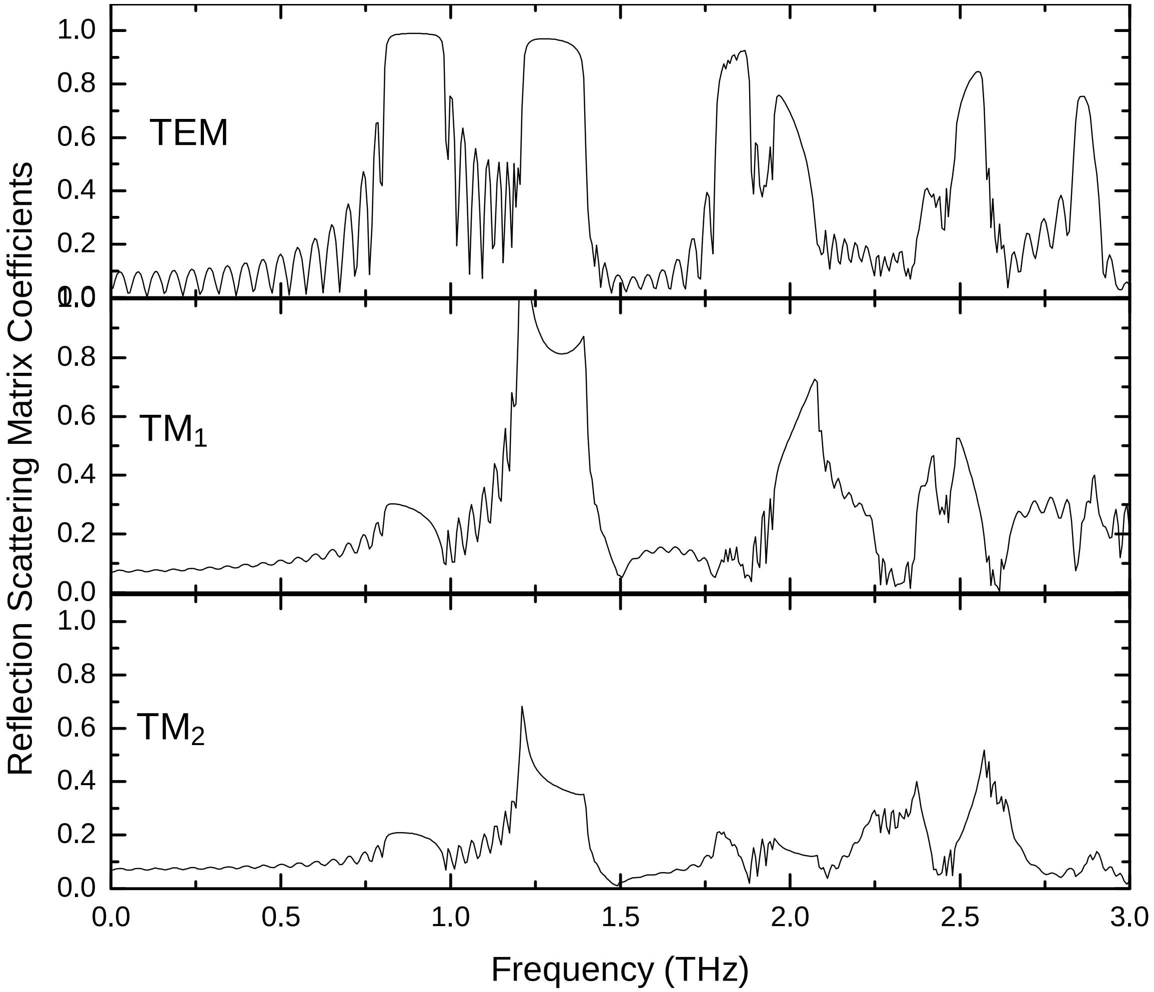

Figure 4-13 - Scattering Matrix Elements for the waveguide junction shown in Figure 4.10. A TEM mode incident from the left reflects at the junction and excites the TEM, TM$_1$, and TM$_2$ modes of the smaller waveguide.

4.8 Theory vs. Experiment

With the scattering matrix for the 17-period 1-D photonic waveguides in place, the transmission coefficients for each of our two structures from Chapter 3, WG-17L and WG-17LD, can be determined. Recall that the trenched section of the waveguide only took up the center 2.64 mm of the waveguide, and that each side of the trenched section is bounded by 11.38 mm of unperturbed 100 μm spaced parallel plate waveguide, meaning all of the power transmitted into the TM_1 mode below 1.5 THz will be evanescent and rapidly attenuate (the same is true for all energy below 3.0 THz for the TM_2) mode. Additionally, the energy in higher order modes that does propagate will propagate with a higher attenuation coefficient than that of the fundamental TEM mode. In keeping with these facts and experimental observations, it is assumed that only energy from the TEM mode will exit the waveguide. As such, the scattering matrix transmission coefficient for the TEM mode becomes the transmission coefficient for the waveguide 17L.

The theoretical E_{out} , which will be compared to the output spectrum from WG-17L is calculated by equation 4.55.

$$E_{out}(\omega) = E_{ref}(\omega)T(\omega)e^{+\alpha(\omega)L_g} \tag{4.55}$$

where $E_{ref}(\omega)$ is the reference spectrum, $T(\omega)$ is the calculated transmission coefficient, $\alpha(\omega)$ is the absorption coefficient from the plane metallic waveguide, and L_g is the length of the grating section. The absorption terms are correction factors applied to take into account that $T(\omega)$ already includes loss for the trenched section of the waveguide. When each of the appropriate $T(\omega)$'s (one for WG-17L, and a separate one for WG-17LD) are used in equation 4.55, two theoretical output spectra are obtained and plotted against the experimental results in Figure 4.14. The solid line (theory) matches the dots (experiment) remarkably well, indicating the strong overlap between theory and experiment.

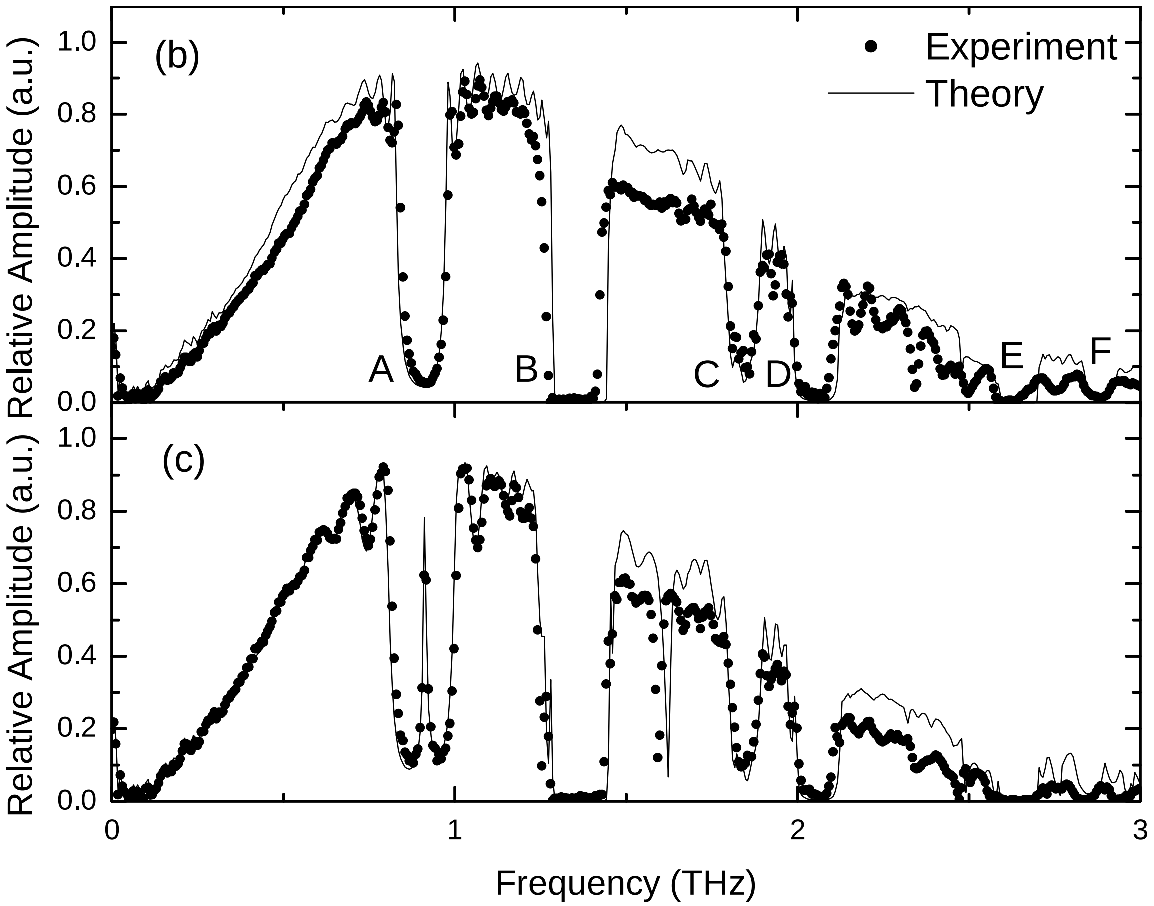

Figure 4-14 - (a) Comparison of theory (solid line) and experiment (dots) for the 1-D photonic waveguide 17L. (b) of theory(solid line) and experiment (dots) for the 1-D photonic waveguide 17LD. The match between theory and experiment is excellent for both cases [66].

The theory shown in Figures 4.14a and 4.14b matches the output of the 17L and 17LD photonic waveguides remarkably well, and replicates the two additional lines found in WG-17LD. If the Q of the defect resonance is defined as the center frequency, 0.915 THz, divided by the measured 3-dB power bandwidth, 7.6 GHz, a Q of 120 is calculated, in excellent agreement with the theoretical 3-dB width of 7 GHz at the calculated 0.913 THz resonance with a theoretical Q of 131. For the dip at 1.59 THz, the inverse 3-dB width is 25 GHz corresponding to a Q of 64. Theory predicts a dip at 1.62 THz that is 27 GHz wide, with a Q of 60. One significant difference between theory and experiment is the sharp line at 2.345 THz in the transmission of WG-17L shown in Figure 2c. This is not believed to be a water vapor line, though there some residual water vapor in the system. The experimental linewidth for this feature is 25 GHz, corresponding to a Q of 94.

With a correct theoretical model in place, the physical origins of the stopbands will be explored. The first six wide stopbands which are predicted by theory have been labeled A, B, C, D, E and F in Figure 4.13a. Stopbands A and C are the result of Bragg reflection due to the grating periodicity. The Bragg stopbands center wavelengths are given by f_{Bragg} = mc/2L, where c is the speed of light, m is an integer and L is the period of the grating.19 For m = 1,2 and L = 160 µm, the stopbands occur at 0.94 THz and 1.86 THz, within stopband A and C, respectively. While the m = 3 stopband at 2.81 THz is closer to the noise floor, it still matches the position of stopband F.

Stopband B, D, and E however, do not result from Bragg reflection, and therefore must be related to waveguiding effects. As seen in Figure 4.8, which shows the scattering matrix elements for the transmission through a single trench, a large portion of energy is both scattered into the TM_1 mode at frequencies centered around stopband B, or is reflected back in the TM_1 mode. Clearly a single trench converts energy from the TEM mode to the TM_1 mode at frequencies close to the cutoff frequency for the TM_1 mode of the larger waveguide. The energy in this mode attenuates rapidly in the smaller waveguide as it is below the cutoff frequency and is therefore evanescent. Other experiments have demonstrated that stopband B shifts with plate spacing, confirming its origin as being due to TM_1 mode conversion. A similar argument can be made for stopband E, which is due to TM_2 mode conversion.

Stopband D, which is centered just above 2 THz, is matched well by theory. However, there is no obvious waveguiding explanation for its appearance.

4.9 Tunable Photonic Waveguides

Armed with a theoretical tool, the mechanisms behind some of the previous applications experimentally demonstrated by Photonic Waveguides can be understood. One of the more promising demonstrations has been the observation of bandgap tuning via changing plate spacing. Zhao and Grischkowsky first observed the widening of bandgaps as the plate spacing is decreased [66]. The observed widening is due to the changing cutoff frequencies of higher order modes.

In order to understand this phenomenon, a 15-period 1-D photonic waveguide with 50 μm deep trenches was simulated with the plate spacing varying in increments of 10 μm from 50 μm to 100 μm. The period of the grating is 160 μm, and the trenches are 80 μm wide. The transmission coefficients for each of the 6 plate spacings are shown in Figure 4.15.

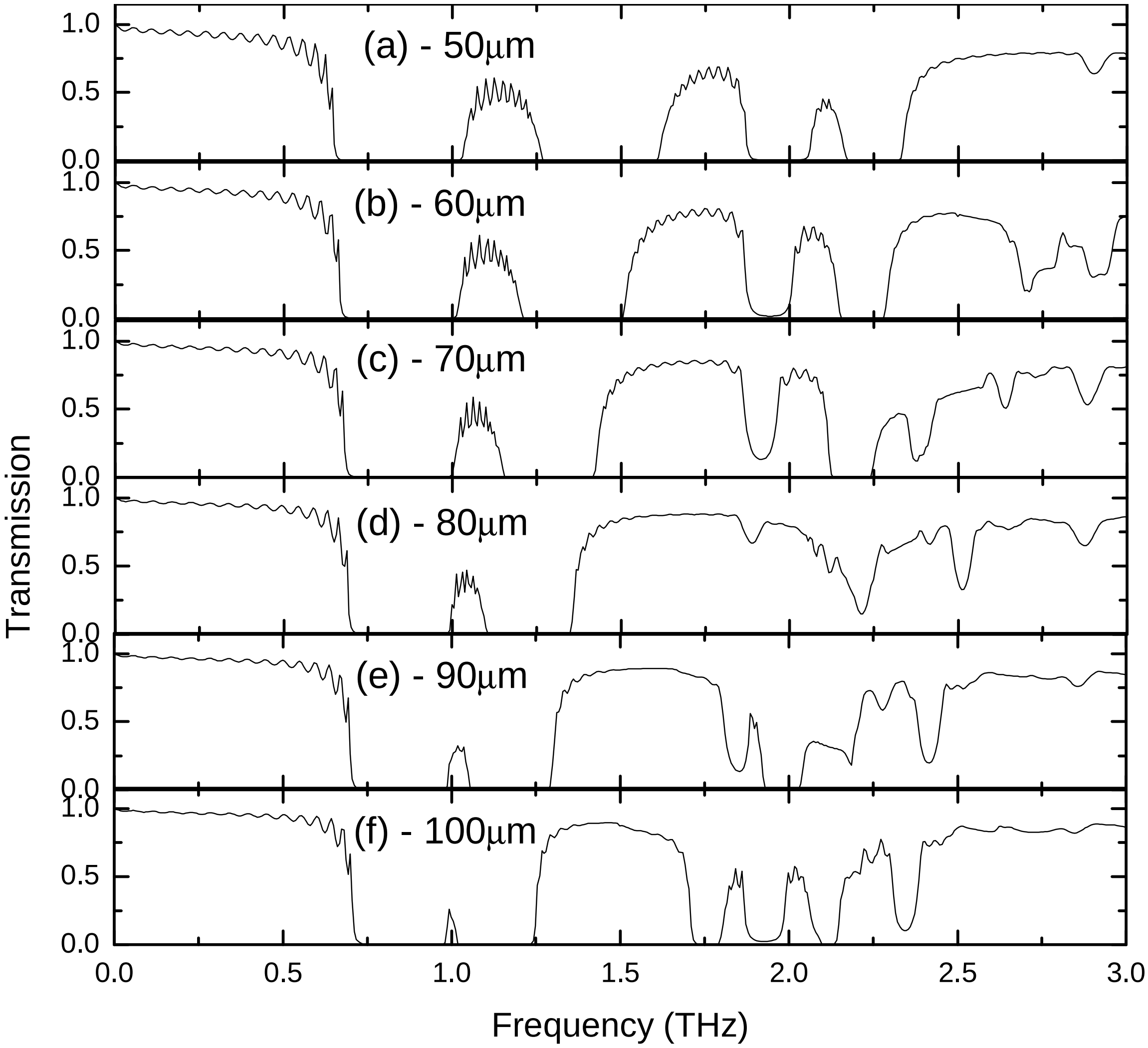

Figure 4-15 - Transmission through a 15-period 1-D photonic waveguide with varying plate spacing. The bandgaps shift and narrow as the plate spacing changes. Note the large 0.75 THz passband in the 80 μm plate spacing transmission coefficient.

The results demonstrate one of the features of the 'modal' bandgaps: they shift with plate spacing. While the first stopband remains mostly stationary, fixed on the Bragg resonance frequency, the second stopband shifts almost 0.25 THz as the plate spacing changes. The passband between the first and second stopbands is almost completely eroded as the plate spacing increases to 100 μm. The other stopbands change with plate spacing as well. Notice the large passband that opens up with a plate spacing of 80 μm. The passband is almost 0.75 THz wide, and only available for that plate spacing. This is due to the third stopband, centered on approximately 2 THz for the 50 μm plate spacing, weakening as the plate spacing increases. Past the 80 μm plate spacing, new stopbands form, limiting the wide passband.

Chapter 5 - THz Photonic Crystal Waveguides

Whereas Chapters 3 and 4 explored the effects of a periodic lattice on the top or bottom plate of a waveguide, Chapter 5 will focus on the effects of placing such a lattice on the side creating a photonic crystal wavguide. These waveguides will be demonstrated with both dielectric and metallic pillars. The results will be compared to finite-difference time-domain simulations.

5.1 Air Propagation of Photonic Crystal Waveguides

Chapter 3 showed photonic crystal's being utilized as an out-of-plane boundary in PPWGs, where one of the planar, metallic boundaries of a PPWG was replaced with the photonic crystal structures consisting of one and two-dimensional patterns. While these structures were complex, for the 1-D case, the geometry could still be approximated as repeated junctions of PPWGs, meaning the essential propagation characteristics were unaltered. In Chapter 5, however, the confinement provided by the photonic crystal lattice will finally be utilized, by shifting the photonic crystal structures will be shifted to create sidewalls in the PPWGs. The introduction of a partially metallic sidewall boundary will dramatically alter the propagation characteristics of the PPWG, creating a photonic crystal waveguide. Whereas the previous photonic waveguides geometries were comparable to a parallel plate waveguide, the waveguides shown in this chapter are more analogous to a rectangular waveguide.

The rectangular waveguide, which in general has many disadvantages for THz pulse propagation, i.e. higher loss, dispersion, and more difficult fabrication, has one significant advantage: spatial confinement. As a parallel plate waveguide gets longer, the diffractive losses in the unguided dimension can become a significant loss process in addition to the Ohmic losses. While the fundamental TE_{10} mode has higher Ohmic propagation losses, it also allows propagation without the diffractive losses associated with longer PPWGs. Most importantly, one can imagine a network of rectangular waveguides routing a THz signal all over a single chip! However, current rectangular waveguide losses for a single mode guide are approximately twice that of a comparatively spaced PPWG. Due to both the higher loss and fabrication difficulties at THz frequencies, there has been little development of rectangular networks.

A photonic crystal with a periodic dielectric constant prohibits propagation for certain frequencies [18]. By inserting defects into the lattice, the frequencies for which propagation is prohibited become trapped, either in a localized point defect, or in a waveguide setting as demonstrated here. A dielectric photonic crystal structure placed in the unguided dimension of a parallel plate waveguide should provided tight confinement with lower loss over conventional metallic rectangular waveguides due to the decrease in metal on the sidewall.

While photonic crystal waveguides have been frequently demonstrated at optical frequencies, examples of THz photonic crystal waveguides are much more limited [23,27-28]. At optical frequencies, the most common photonic crystal waveguide structure consists of a dielectric slab that has been etched with submicron holes. One row of holes is not etched creating a waveguide channel. A common photonic crystal waveguide is shown in Figure 5.1.

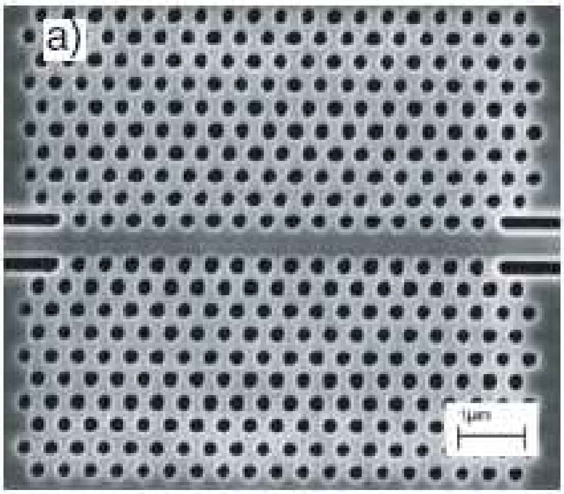

Figure 5-1 - Typical W1 channel at Optical Frequencies [68].

The photonic crystal lattices in this chapter were fabricated following the same procedure as outlined in Chapter 2. Before metallization, a channel was integrated into the photonic lattice by removing necessary cylinders. This process was done by hand under a microscope using a tungsten dissecting probe with a 30 μm diameter. By carefully applying pressure on desired cylinders with the dissecting probe, specific patterns could be integrated into the photonic crystal, allowing ideal channel waveguides to be fabricated. After removing the desired cylinders, the chip is metallized. An example of a 2-D lattice with 1 row removed is shown in Figure 5.2. Note the excellent quality of the area where the cylinders have been removed by hand. Some residual photoresist remains, but is considered to be far enough sub-wavelength over the bandwidth to have little effect on the transmission.

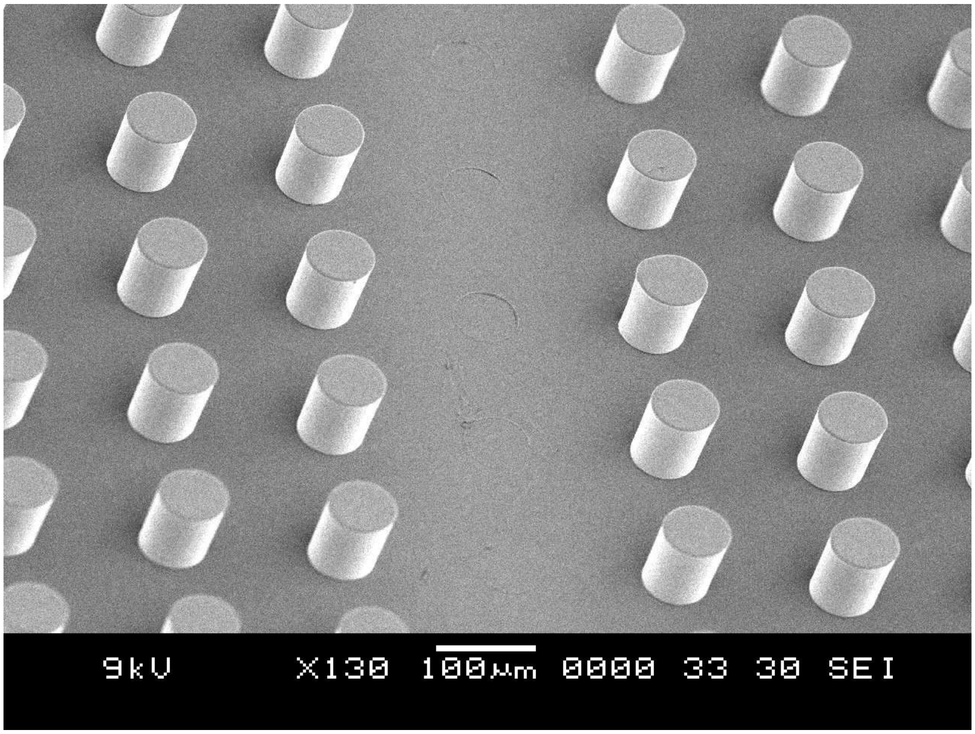

Figure 5-2 - Modified W1 channel at THz Frequencies. The cylinders are 70 μm in diameter, 70 μm tall, and have a 160 μm period.

The experimental setup for the following demonstrations was modified by the use of hyper-hemispherical silicon coupling optics as opposed to the plano-cylindrical lenses used in the photonic waveguide experiments of Chapter 3. This was necessitated by the sidewall boundaries created by the photonic crystal lattice on each side of the air-channel. In previous experiments, there was no sidewall, and as such, no focusing was needed in the unbound dimension of the parallel plate waveguide. In this case, which is more similar to a rectangular waveguide, the spherical optics yielded a much higher transmitted signal. The other primary difference is the lack of an air gap over the top of the cylinders; the only significant air gap is in the air channel created by removing the row of pillars. A diagram illustrating the entrance face of the waveguide channel is shown in Figure 5.3. For the 70 μm diameter cylinders with the 160 μm period that used for the majority of the photonic crystal waveguide devices, removing one row of cylinders creates an opening that is a minimum of 250 μm wide for THz propagation.

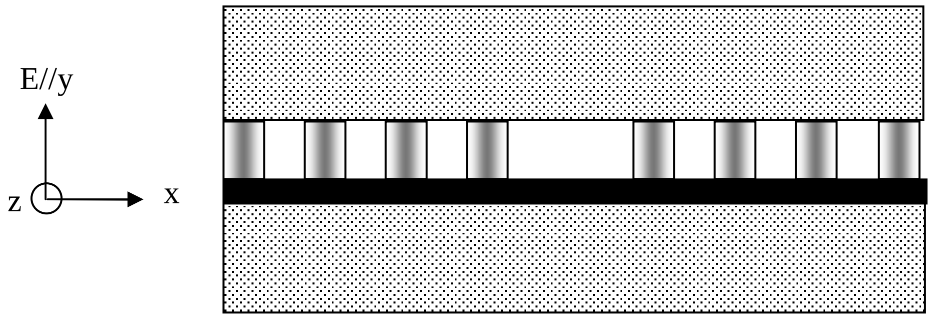

Figure 5-3 - Diagram of THz photonic crystal waveguide bounded by parallel plates. The propagating THz pulse is polarized in the y-direction and is propagating in the z-direction (into the page). Plano-spherical Si lenses not shown) [69].

5.2 Photonic Crystal Waveguide I: Dielectric

The first attempt at transmitting through a photonic crystal waveguide utilized an unmetallized SU-8 chip. In this case, fabrication took place after a 300 μm thick layer of Aluminum was evaporated onto a silicon wafer. This provides a metallic boundary under the pillars. After fabrication, one row of pillars was removed. The pillars are approximately 70 μm tall with a 100 μm diameter and a period of 160 μm. The 9.43 mm chip holding the waveguide was placed into a matched Aluminum parallel plate waveguide as previously described, and the THz pulse was coupled into the waveguide with hyper-hemispherical optics. A single scan output pulse is shown in Figure 5.4.

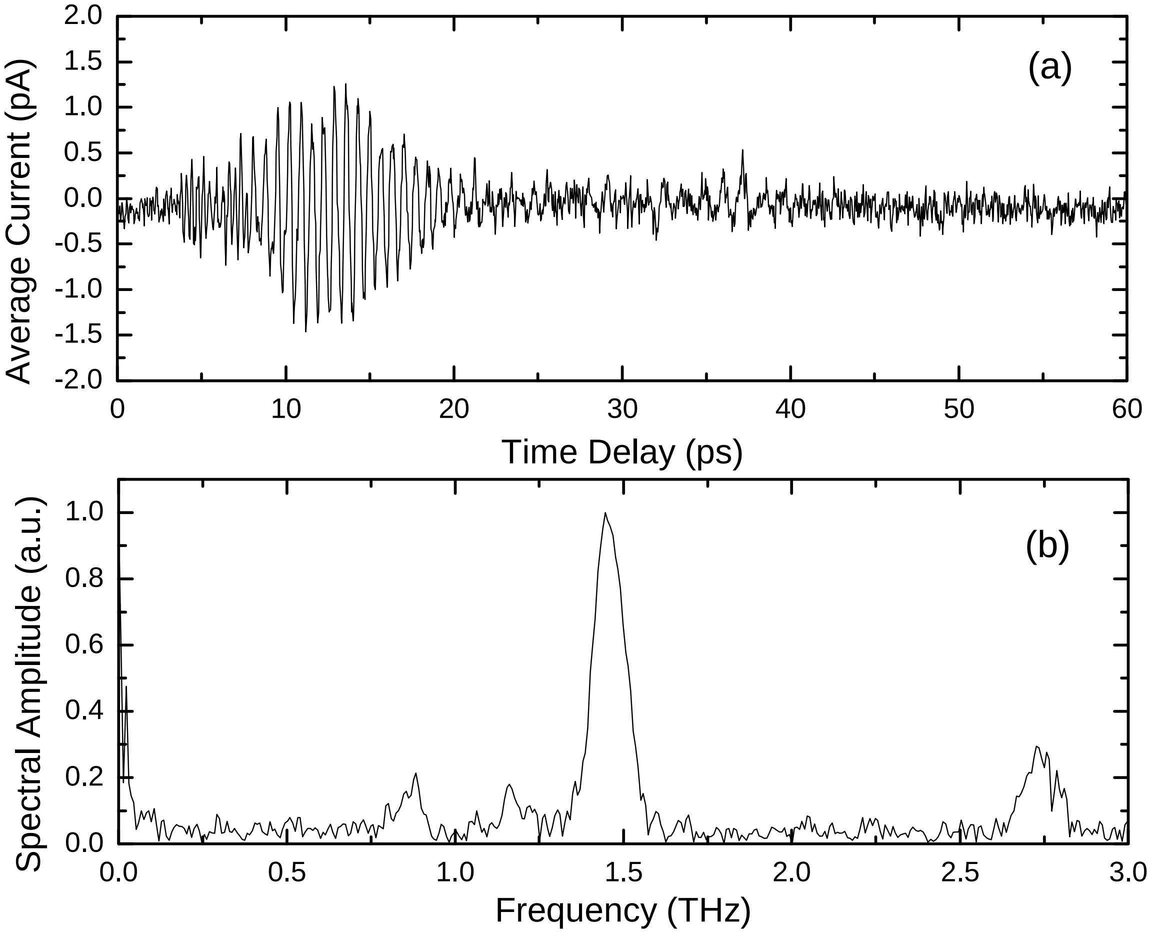

Figure 5-4 - (a) Single pulse through dielectric W1 channel. (b) Spectral Amplitude of pulse.

The weakly guiding nature of this structure is evident from both the strength of the output pulse and the small spectral signal that exits the waveguide. Clearly little energy is being guided in this photonic crystal waveguide. The bulk of the signal is in a peak at approximately 1.45 THz. Though the dielectric photonic crystal waveguide fabricated out of dielectric pillars should have theoretically lower loss than a waveguide with metallic pillars, it was determined that a transition to metallized pillars would be necessary to confine the energy. Some reasons for the poor guiding characteristics are the relatively low refractive index (n = 1.7) and high loss of SU-8 at THz frequencies. Additionally, the lack of total internal reflection (TIR) due to the air core resulted in weaker guiding.

5.3 Photonic Crystal Waveguide II: Metallic

The lack of transmission from the SU-8 photonic crystal waveguide forced the switch to metallized photonic crystal waveguides. More photonic crystal chips were fabricated and metallized; in this case, the diameter of the cylinders was reduced to approximately 60 μm, to lower the Ohmic losses (for the patterns available). In order to measure the attenuation of the photonic crystal waveguide, two identical samples were fabricated, WG-1 which was 9.43 mm long, and WG-2 which was 25.4 mm long. The samples were fabricated on the same wafer to ensure that they had identical geometrical parameters. After removing a single row in each sample, and metallization, the chips were placed into matched parallel plate waveguides. A 3 mm long strip of a metallized photonic crystal chip is shown in Figure 5.5.

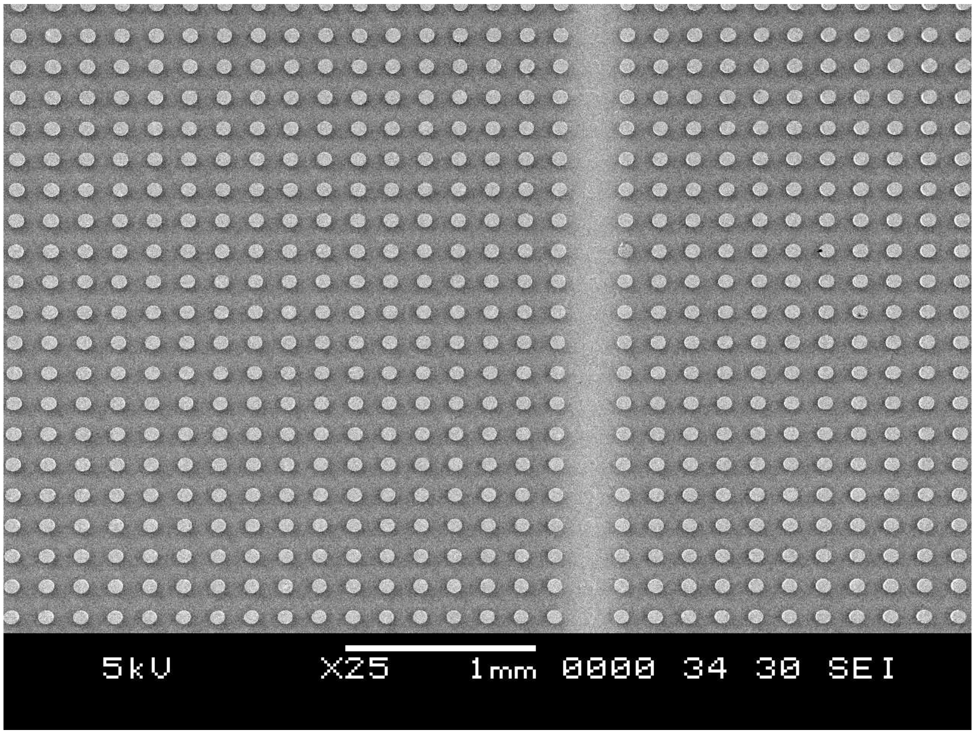

Figure 5-5 - Metallic W1 channel at THz Frequencies. The cylinders are 60 µm in diameter, 70 µm tall, and 160 µm period. Note the excellent fabrication quality with no defects over the area of the sample.

Before inserting the waveguides, a reference spectrum was obtained by moving the Silicon lenses together into their confocal position. While this maximized the transmitted energy, the focus of the lenses is approximately 50 µm after the exit face of the lenses, resulting in the lenses being separated by an airgap of approximately 100 µm. This airgap produced undesirable reflections which distorted the pulse shape. In order to realize a proper reference spectrum, the lenses were then moved away from each other and another reference scan was taken, this time with the correct pulse shape. The spectrum from this pulse was then scaled to match the energy in transmitted through the lenses in their confocal position. This scaled spectrum became the new reference for the photonic crystal waveguides. The output spectra for WG-1 and WG-2 (hatched spectrum) are shown in Figure 5.6. They are plotted relative to the normalized reference spectrum which is shown in the inset.

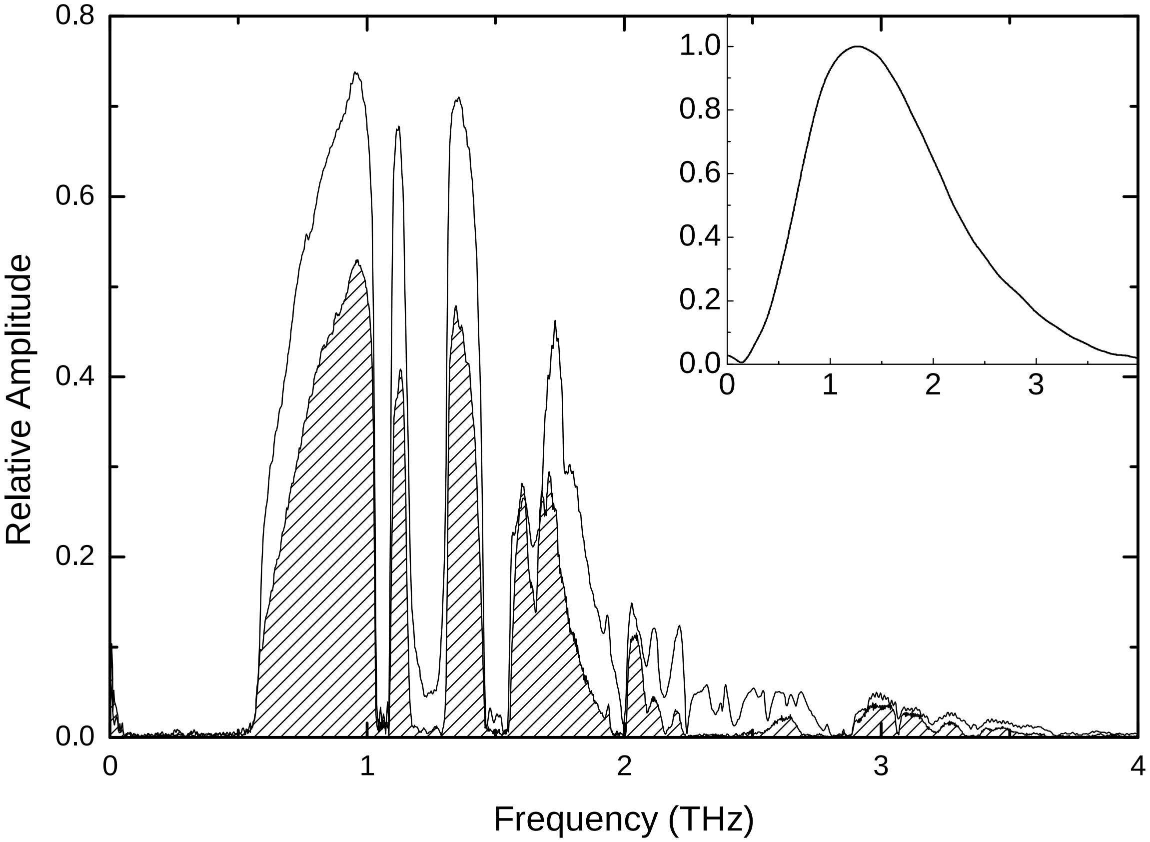

Figure 5-6 – Output Spectra from the 9.43 mm long WG-1 and the 25.4 mm long WG-2 (hatched spectrum). Inset: Normalized reference pulse, which output spectra from WG-1 and WG-2 are relative to [69].

The output of the photonic crystal waveguides overlap extremely well, indicating the excellent quality of fabrication. Both waveguides have a cutoff frequency of 0.58 THz, due to the aperture on the input face of the waveguide. . As the rectangular waveguide is the common geometry that is most similar to the photonic crystal waveguides presented here, it should generate cutoff frequencies similar to those for an equivalently sized rectangular waveguide.

The cutoff frequency for the TE_{10} mode of a rectangular waveguide is $f_c = c/2a$, where c is the speed of light, and *a* is the width of the waveguide [63]. For f_c = 0.58 THz, the effective width is a = 258 μm. This is slightly larger than the 250 μm minimum separation of the cylinders, which is reasonable due to the incomplete metal boundary on the sidewalls.

There are multiple stopbands in the output, which are characteristic of photonic crystals. The first passband from 0.58 to 1.1 THz is the widest of the passbands, while the higher frequency passbands are narrower. The turn-ons/turn-offs at 1.04, 1.09, 1.46, and 1.55 THz are extremely sharp, with approximately 10 GHz from peak to valley.

One remarkable feature of the photonic crystal waveguide is the lack of multimodal interference in the output spectra of the two waveguides. For all previously demonstrated THz waveguides, coupling to a higher order mode has resulted in rapid spectral oscillations beginning at the cutoff frequency of that higher order mode and spreading out as frequency increases [3]. Therefore it is assumed that the pulse is propagating in a single mode. This is remarkable due as the available bandwidth overlaps over 12 modes for a comparable rectangular waveguide.

The complete time and frequency domain data for WG-1 are shown in Figure 5.7. Figure 5.7a shows the time-domain pulse, with the inset showing the pulse ringing which extends to 130 ps where it has been truncated due to a reflection from the silicon lenses. Figure 5.7b shows the spectral amplitude transmission of the pulse. Figure 5.7c shows the power transmission in dB. The stopbands are as much as 40 dB deep, comparable to the photonic waveguides of chapter 3.

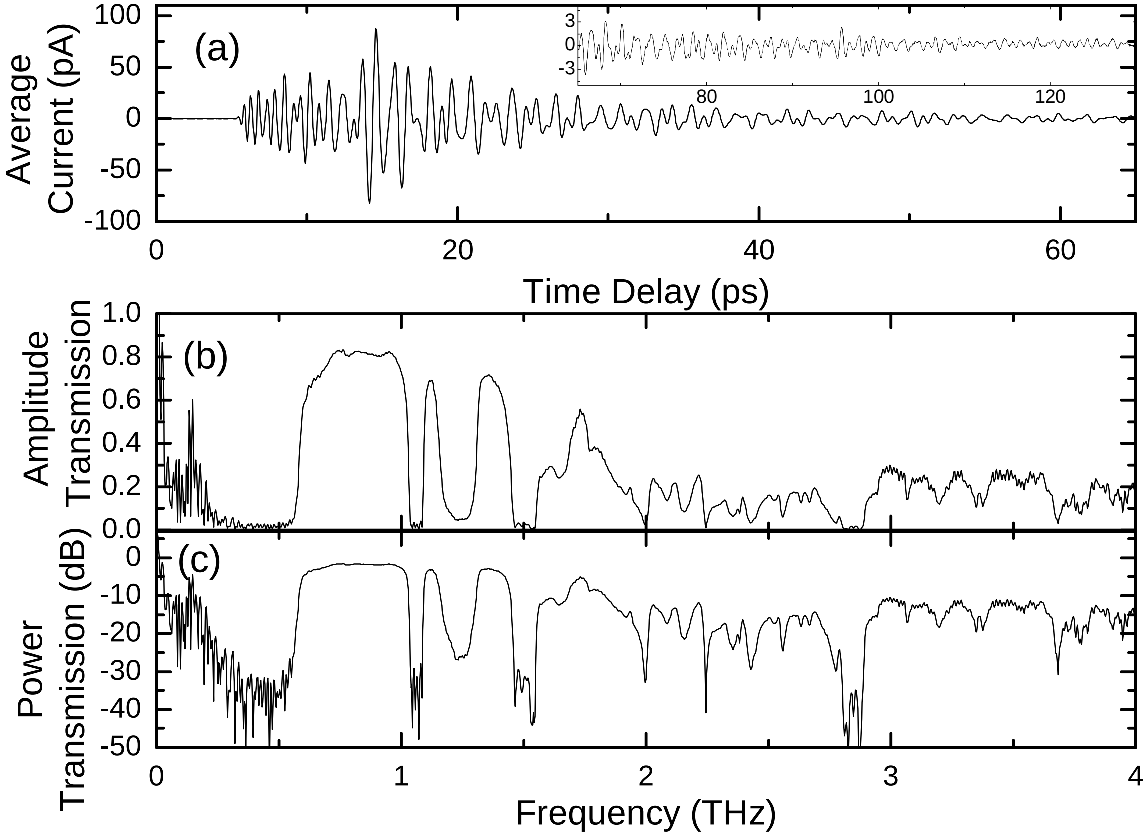

Figure 5-7 - (a) Average of 4 THz pulses through WG-1, a 9.43 mm long photonic crystal waveguide. The ringing past 65 ps is shown on an expanded scale in the inset. (b) Amplitude transmission of WG-1. (c) Power Transmission in dB.

The complete time and frequency domain data for WG-2 are shown in Figure 5.8. Figure 5.8a shows the time-domain pulse, with the inset showing the pulse ringing which extends to 160 ps where it has been truncated due to a reflection from the silicon lenses. Figure 5.8b shows the spectral amplitude transmission of the pulse. Figure 5.8c shows the power transmission in dB.

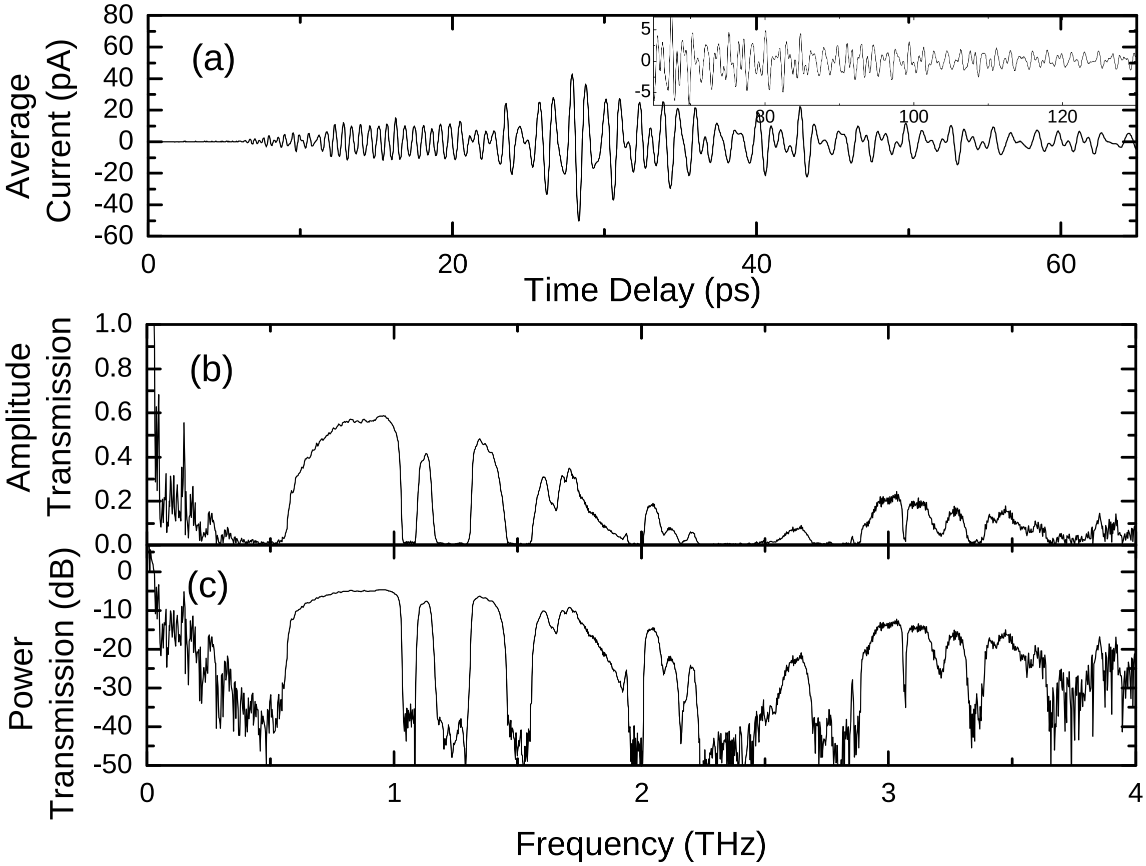

Figure 5-8 - (a) Average of 4 THz pulses through WG-2, a 25.4 mm long photonic crystal waveguide. The ringing past 65 ps is shown on an expanded scale in the inset. (b) Amplitude transmission of WG-2. (c) Power Transmission in dB.

5.4 Photonic Crystal Waveguide Attenuation.

Using the spectral data from the two photonic crystal waveguides, the amplitude attenuation can be easily calculated. As a reference point, the attenuation of the photonic crystal waveguide will be compared to a comparable gold rectangular waveguide. The experimental frequency-dependent attenuation coefficient was calculated using equation 5.1 [8]:

$$\alpha(\omega) = \frac{1}{(L_1 - L_2)} \ln\left|\frac{E_{out2}(\omega)}{E_{out1}(\omega)}\right| \tag{5.1}$$

where L_1 = 9.43 mm is the length of the short waveguide, L_2 = 25.4 mm is the length of the long waveguide, $E_{out1}(\omega)$ is the output spectrum of the short waveguide, and $E_{out2}(\omega)$ is the output spectrum of the long waveguide.

To calculate the theoretical absorption of the rectangular waveguide the standard waveguide attenuation formula for the TE_{10} mode was used. TE_{10} is the fundamental mode, and has the corresponding lowest loss of any rectangular waveguide mode. The calculation was done assuming a completely gold waveguide, which should have a slightly lower loss than the actual experiment condition of three gold sidewalls and one aluminum sidewall. The formula for the attenuation of the TE_{10} mode of a gold rectangular waveguide is given in equation (5.2) [47,63].

$$\alpha = \frac{R_s}{a^3 b \beta k \eta_o}(2b\pi^2 + a^3 k^2) \tag{5.2}$$

Where

$$R_s = \sqrt{\frac{\omega\mu_o}{2\sigma}}$$

is the surface resistance of gold, a = 258 μm is the width of the waveguide, b = 70 μm is the height of the waveguide, k = ω/c is the wavenumber, $\beta = \sqrt{k^2 - \left(\pi/a\right)^2}$ is the propagation constant, μ_o is the permeability of free space, σ = 4.098 x 10^7 S/m is the DC conductivity of gold and η_o = 377 Ω is the impedance of free space.

The attenuation coefficient of the raw data is shown in Figure 5.8 plotted against the theoretical attenuation coefficients of the rectangular waveguide. The stopband regions have been covered by the shaded boxes for clarity.

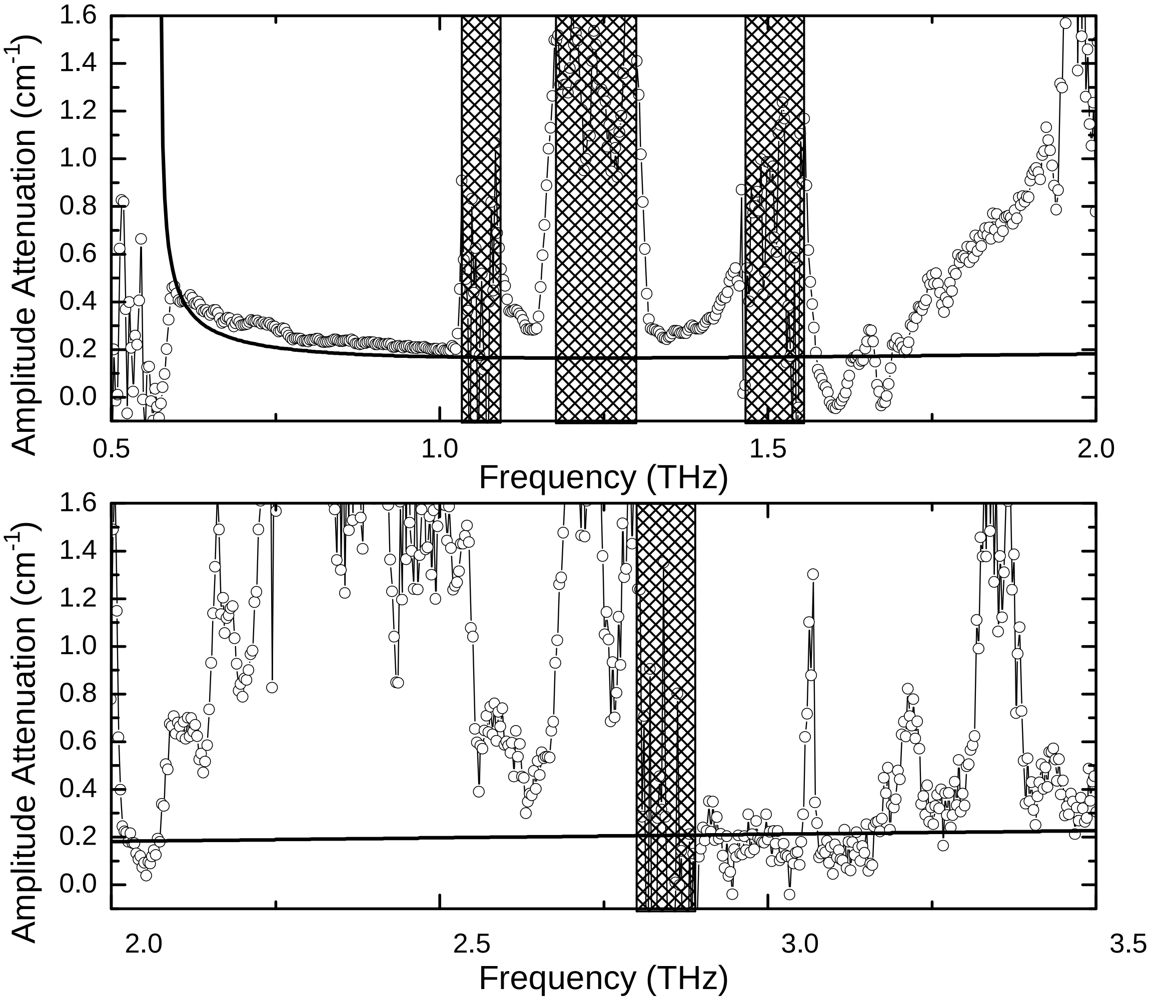

Figure 5-9 - Experimental attenuation coefficient of metallic photonic crystal waveguide (solid line with open circles) vs. theoretical attenuation coefficient the 70 μm x 250 μm gold rectangular waveguide (thicker solid line) [69].

The experimental attenuation coefficient approaches that of the rectangular waveguide for the first 3 passbands up to 1.4 THz. After that point, there are four regions where attenuation dips below that of the rectangular waveguide. The broadest region is from 2.90 to 3.17 THz, approximately centered on the sharp absorption feature at 3.08 THz. This sharp absorption feature has a FWHM of 12.4 GHz.

It should be noted that this calculation for the absorption doesn't include the effect of the different coupling coefficient from the free space beam to the waveguide mode for the different waveguide lengths. As the coupling is slightly worse for the longer waveguide than the shorter waveguide due to the size of the beam relative to the lens aperture, this experimental value should be considered an upper bound on the absorption. An additional factor to consider in regards to the attenuation measurement is the true value of the DC conductivity for our metallic waveguides. Recent demonstrations calculating the attenuation of a PPWG cooled to liquid nitrogen temperatures did not show the expected decrease in attenuation corresponding to the expected increase in conductivity [70]. Additionally, the measured attenuation coefficients for metallic waveguides at THz frequencies rarely attain the loss predicted by theory, leading to questions about the conductivity in the skin depth layer of the metal that our THz pulses interact with. As such a measurement demonstrating loss approximately equal to the theoretical loss for a rectangular waveguide is likely better than any possible observable real-world loss of rectangular waveguides at THz frequencies.

5.5 Theoretical Simulations of THz Photonic Crystal Waveguides.

In order to fully characterize the photonic crystal waveguides, an appropriate theoretical model was necessary. While conventional modal solutions, such as those used for common waveguide geometries, were unavailable for comparison, numerical techniques provided an alternative avenue to model the photonic crystal waveguide. While there are a variety of numerical techniques, the FDTD method was the obvious choice for a number of reasons. First, it is relatively simple when compared to other numerical methods, and numerous commercial and public software programs available. Second, the time-domain nature of the FDTD method allows the output of a complete spectrum of frequencies to be calculated in a single simulation, as opposed to frequency-domain techniques which only determine the output of one frequency per simulation. Finally, the photonic crystal waveguide can be simulated in a 2-D environment due to the spatial variation in the y-direction, dramatically reducing calculation time.

The FDTD method is conceptually simple. As with most numerical techniques, the problem was broken into a grid, whereupon a solution can be determined at each point. Conceptually the method involves solving differential equations by taking small step sizes and computing the finite differences between adjacent points in a grid. The differential equations can then be reduced to simple algebraic equations, which can be quickly solved with the aid of a computer. The FDTD method allows solutions of Maxwell's equations for a great variety of problems to be determined.

The initial plan was to simulate these metallic structures with realistic conductivities. However, when including real values of the conductivity (sigma = 4.098×10^7 S/m for gold), it became necessary to reduce the grid size in the metal, so that the step sizes would be smaller than the skin depth of the metal. At THz frequencies, the skin depth is ~100 nm. This makes it necessary to have a step size significantly smaller than 100 nm, dramatically increasing the size of the calculation. As such the metallic cylinders were assumed to be perfectly conducting.

The simulation was carried out using F2P freeware available online [71]. This software is extremely adept at simulating photonic crystal environments and is designed to be user friendly in terms of setting up periodic boundaries. The geometry was set to match the real-world parameters of the experiment. Since both waveguides resulted in similar outputs, the shorter 9.43 mm long photonic crystal waveguide was simulated to reduce the calculation time. The simulation was done with 2 micron spatial steps and 4.5 fs temporal steps. The 2 µm steps yield λ/50 resolution at the trail edge of the THz pulse spectrum at 3 THz. Over the bulk of the output spectrum, the resolution is far better. For example, near the peak spectrum at 1 THz, the resolution is λ/150 due to the longer wavelengths at lower frequency. The excitation was a 100 µm plane at the input of the waveguide and was detected with a line detector at the output (integrated over line?). The total time length of simulation was approximately 200 ps, similar to the time-domain scan lengths of 130-160 ps.

One significant challenge was creating a proper excitation spectrum. Using the software, it was difficult to make a pulse which had a corresponding spectrum that was an exact match with the reference spectrum. However, by taking advantage of the linear systems nature of the photonic crystal waveguide, it was possible to filter the output spectrum, ensuring that the relative strength of the excitation spectrum was identical. The frequency domain filter, H(w), which was multiplied with the normalized output spectra is shown in equation 5.3:

$$H(\omega) = E_{FDTD}(\omega) / E_{ref}(\omega) \tag{5.3}$$

$E_{ref}(\omega)$ is the reference spectrum for the experimental data, and $E_{FDTD}(\omega)$ is the excitation spectrum used in the simulation. H(ω) was then multiplied onto the output spectrum of the simulation. This scaled the frequency domain components of the output to their appropriate strengths, ensuring an output that can be properly compared to the output spectrum from the experiment. Figure 5.10a compares the spectra from the experimental reference pulse and the excitation pulse of the simulation. Each was self-normalized for comparison. Figure 5.10b shows the H(ω) filtering function calculated using equation (5.3). As the simulation spectrum had slightly larger bandwidth, the adjustment provided by H(ω) was necessary.

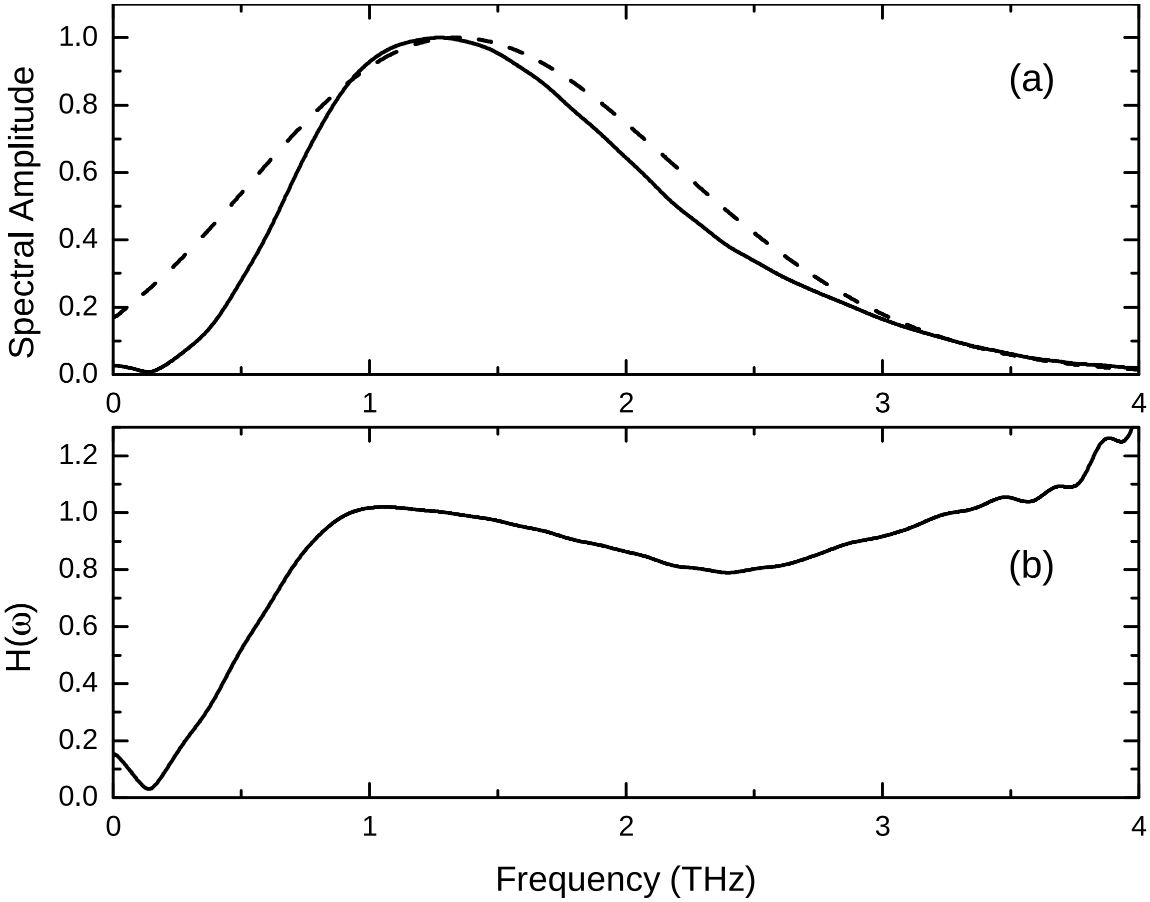

Figure 5-10 – (a) Normalized experimental reference pulse spectrum (solid line) overlapped with normalized simulation excitation spectrum (dashed line). (b) H(ω), ratio of the spectra shown in (a)

The comparison of theory and experiment (hatched spectrum) is shown in Figure 5.11. The theoretical spectrum was scaled to match the amplitude of the experimental spectrum at the first passband. The match is generally quite good, considering the natural differences between the experiment and the simulated experiment, namely the lack of perfect metal, as well as the discretized simulated cylinders vs. the geomtreically perfect real cylinders. The higher relative signal at high frequencies is expected, as the Ohmic losses will be larger at higher frequencies for real metal. The similarities are striking especially in regards to the match of the locations and strength of the stopbands across the bandwidth. The sharp absorption feature at 3.08 THz (which is more visible in the longer waveguide spectrum shown in Figure 5.8) is replicated in the experiment. The match between theory and experiment gives further confidence in the quality of the fabrication and the utility of future waveguides.

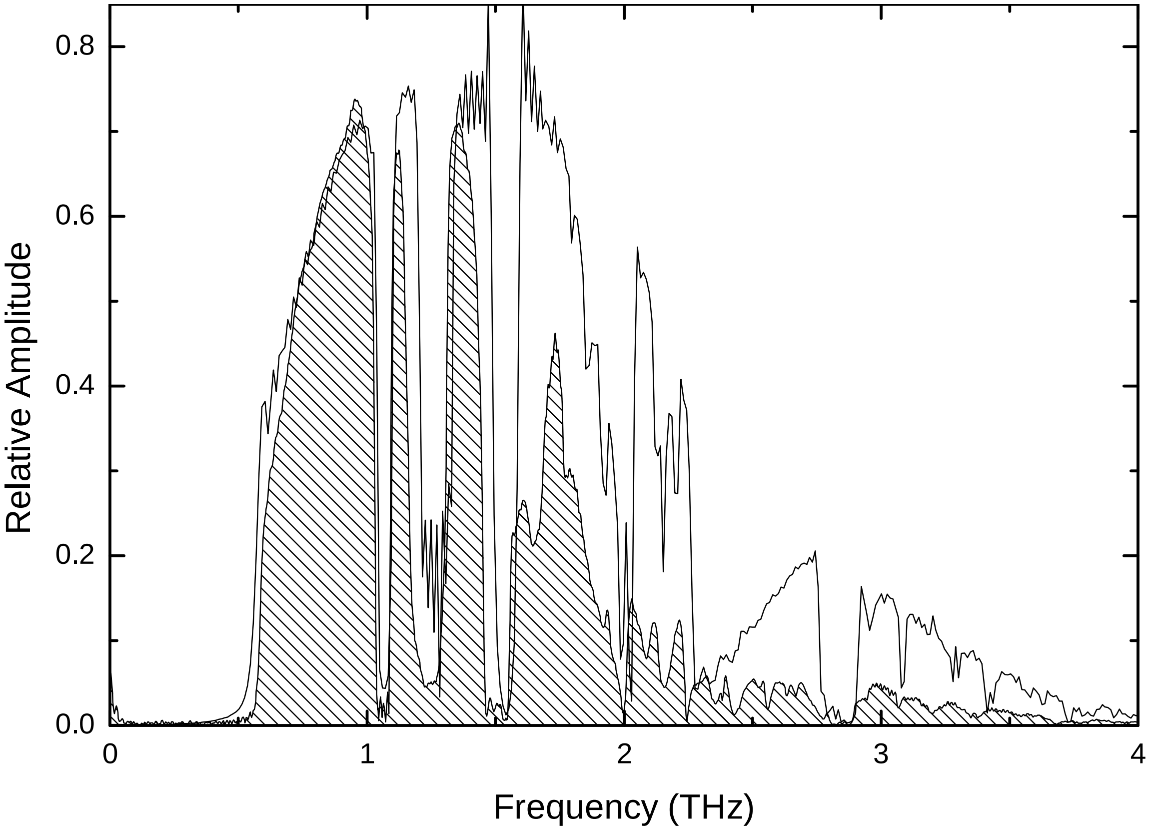

Figure 5-11 – Comparison of FDTD simulation (solid line) and experimental results (hatched spectrum) for the 9.43 mm long photonic crystal waveguide [69].

5.6 Future Considerations

The metallic photonic crystal waveguide was demonstrated to have excellent transmission characteristics with loss approaching, and even exceeding that of a rectangular waveguide across the bandwidth. FDTD simulations proved the validity of these measurements by conforming to the pass and stop bands demonstrated by the photonic crystal waveguide. While the dielectric photonic crystal waveguide demonstrated extremely poor guiding properties, the optical regime will provide more robust, low-loss waveguide designs in the future.

Chapter 6 - Photonic Crystal Waveguide Devices

The photonic crystal waveguides demonstrated in Chapter 5 showed excellent transmission characteristics with reasonable loss. With this platform for a 2-D integrated system established, integrated circuitry can be added. While there are a number of options, the simplest components to integrate are cavities. Chapter 6 will focus on the design and realization of some of these integrated cavities. The performance of integrated cavities in a conventional rectangular waveguide will compared to the photonic crystal waveguide cavities.

6.1 Rectangular Waveguide Cavities

Before beginning work on the photonic crystal waveguide cavities, work on rectangular waveguide cavities was done in collaboration with Paul George and Dr. Farhan Rana of Cornell University. While these structures are not directly related to the photonic crystal waveguides which will be demonstrated later in this chapter, the results will provide an interesting comparison. Though rectangular waveguide cavities have been utilized for over 60 years, this was the first demonstration of such an integrated component at THz frequencies. During his visit, Paul George brought the fabricated waveguides in for testing in the THz-

TDS systems used in the UTOL. As opposed to the SU-8 fabrication process, these waveguides were fabricated by using refractive ion etching (RIE) on a silicon wafer, etching the desired waveguide and cavity structure 150 µm deep into the silicon wafer. After etching the devices they were metalized with 400 nm of gold and placed in contact with a separate gold covered wafer (forming the top plate of the rectangular waveguide. An SEM of the rectangular waveguide cavity is shown in Figure 6.2.

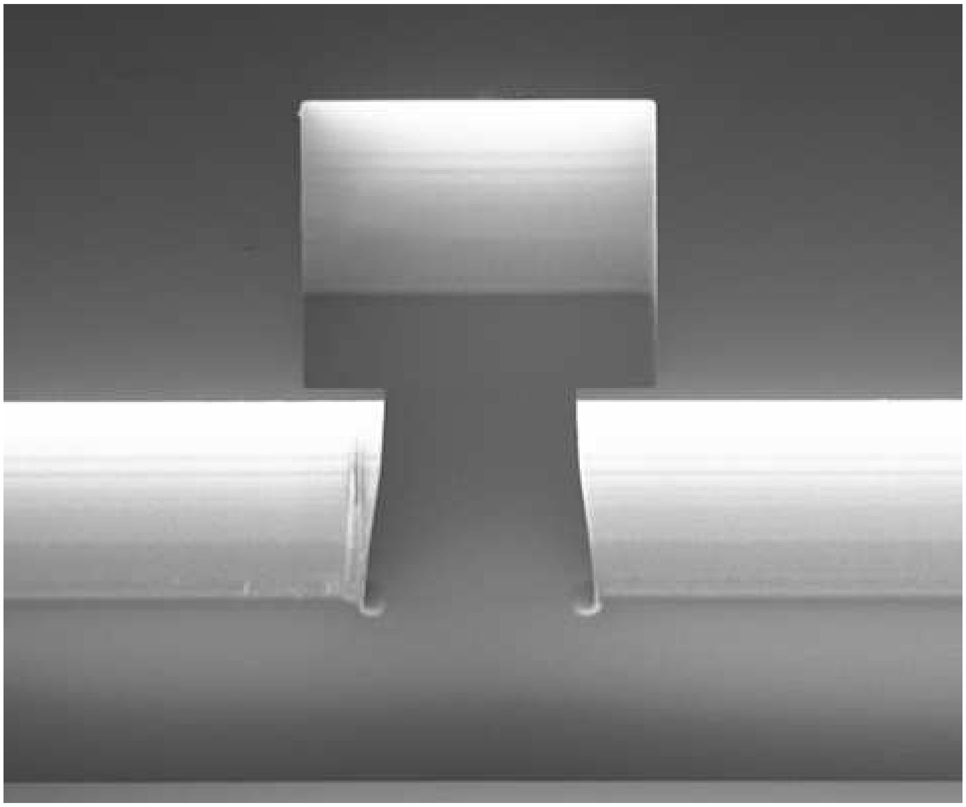

Figure 6-1 – SEM image of rectangular waveguide cavity. The cavity aperture is 100 µm wide, and the cavity dimensions are 125 µm x 125 µm x 150 µm tall [72].

The rectangular waveguide is 200 µm wide x 150 µm tall. The cavity is side-coupled, via an aperture on one of the sidewalls. The cavity aperture's varies in width from 80 – 100 µm. The wall of the aperture is 10 µm wide, and the vertical edge of the aperture are not perfectly straight due undercutting in the RIE process. Three different cavity sizes were studied. The height of the cavities is fixed at the 150 µm etch depth, and the other dimensions for the cavities were 125 x 125 µm, 150 x 150 µm and 175 x 175 µm. As the transmission characteristics of the different cavities were extremely similar, a complete measurement will only be shown for one of the waveguide cavities. The transmission through a 125 µm x 125 µm rectangular waveguide cavity with a 100 µm wide cavity aperture is shown in Figure 6.3.

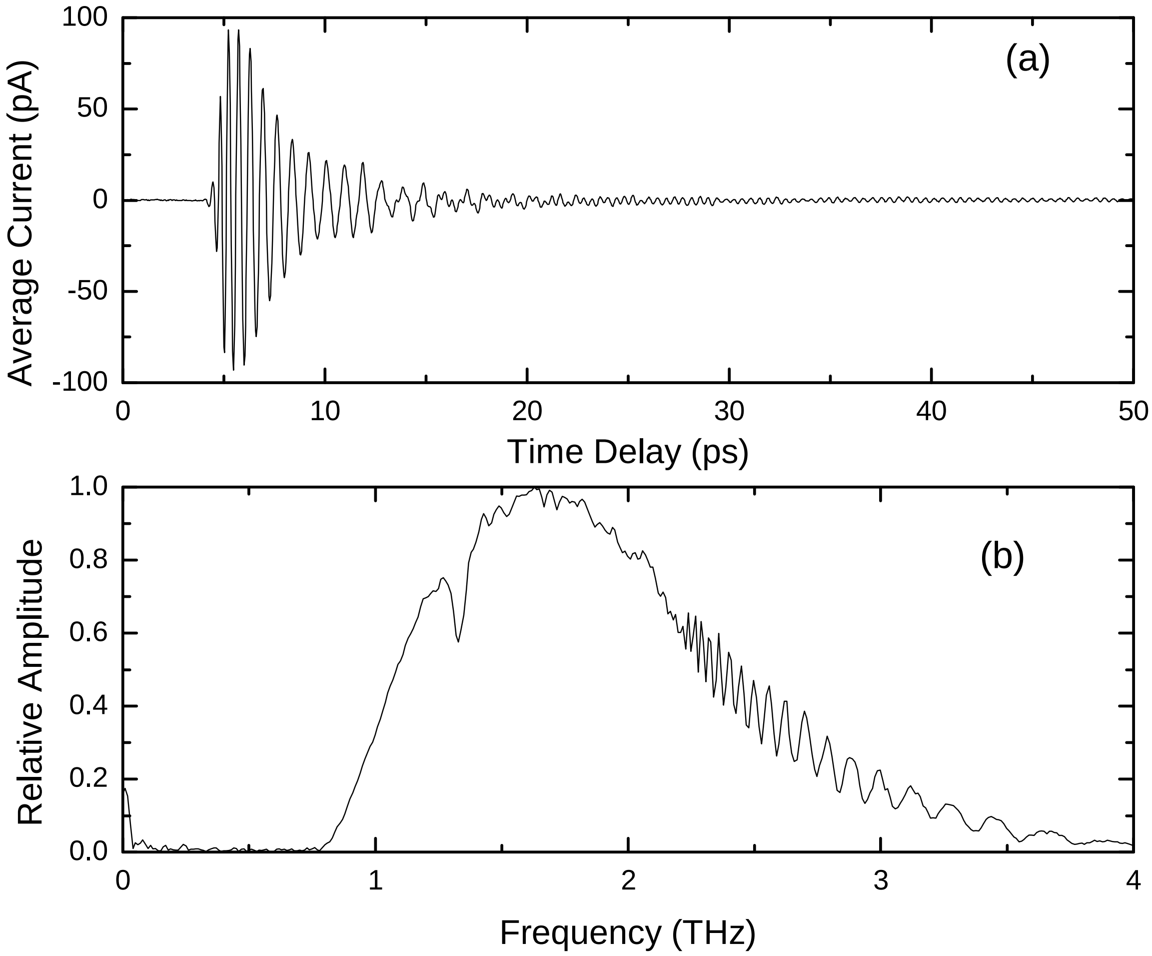

Figure 6-2 – (a) Time domain THz pulse measurement of side-coupled rectangular waveguide cavity. The cavity is 125 µm x 125 µm with a 100 µm aperture. (b) Spectral amplitude of (a) [72].

Figure 6.3a shows the time-domain THz pulse after propagating through the waveguide. As the fundamental mode of the rectangular waveguide is the dispersive TE_{10} mode, there is dispersive propagation, with a sinusoidal pulse ringing after the main envelope of the pulse has passed through. Figure 6.3b shows the corresponding amplitude spectrum. The cavity resonance of the TE_{101} mode at 1.33 THz is immediately distinguishable, and the oscillations beginning at 2.15 THz are due to coupling to the TM_{11} mode. These oscillations represent frequency-domain interference that is characteristic of multimode propagation for broadband THz waveguides [3].

The results for the remaining waveguides were remarkably similar. Each had a single resonance and oscillations due to multimode propagation beginning at 2.15 THz. The results from the rectangular waveguide cavities are shown in Table 6.1. The larger cavities gave corresponding lower frequency resonance, and the narrower apertures shifted the resonances to slightly higher frequency. For example, the 175 µm x 175 µm cavity with a 100 µm aperture had a resonant frequency of 1.08 THz, while the 90 µm aperture blue-shifted the resonance to 1.09 THz. The resonances had typical FWHMs of 50 GHz.

DIMENSIONS (MM)	**APERTURE (MM)**	**RESONANT FREQUENCY (THZ)**	**FWHM (GHZ)**
175 x 175	100	1.08	68
175 x 175	90	1.09	50
150 x 150	100	1.20	50
150 x 150	90	1.22	59
125 x 125	100	1.31	50
125 x 125	90	1.33	53

Table 6-1 – Experimental results from rectangular waveguide cavities. All of the cavities have a constant height of 150 µm [72].

6.2 Design of Photonic Crystal Waveguide Cavities

In contrast to the rectangular waveguide cavities, where the cavities consisted of subtle variations of a standard rectangular waveguide cavities, a variety of different photonic crystal waveguide cavities were designed. In order to create cavities with only the sharpest resonances, numerical simulations were performed so that cavities with poor confinement would not be fabricated and tested experimentally. These simulations were carried out using the FDTD software discussed in Chapter 5 [71]. Figure 6.1 shows 2D diagrams of the cavities which were designed and simulated. The photonic crystal lattice has similar physical dimensions as the waveguide demonstrated in Chapter 5. While the height of 70 µm and the periodicity of 160 µm remain the same, the diameter of the cylinders was increased to 108 µm. It should be noted that simulations performed for 70 µm cylinders produced qualitatively similar results.

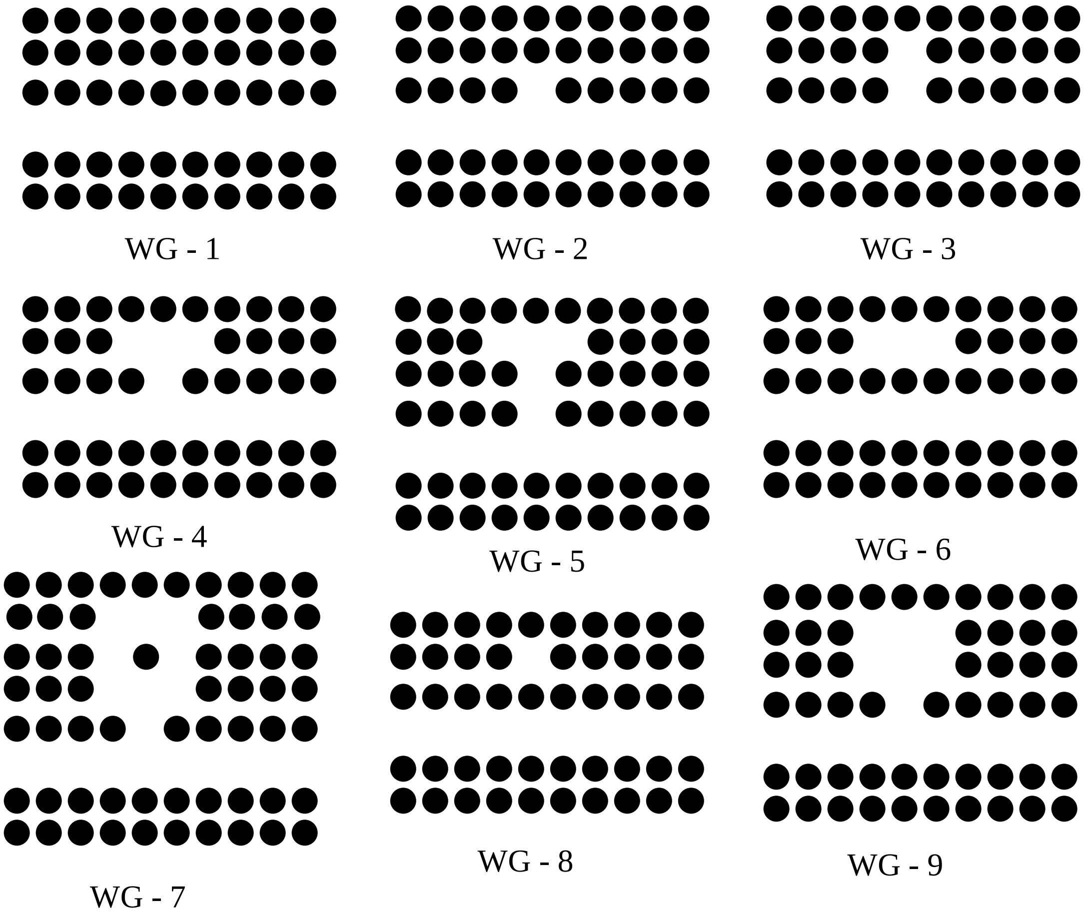
WG - 1 WG - 2 WG - 3 WG - 4 WG - 5 WG - 6 WG - 7 WG - 8 WG - 9

Figure 6-3 – Defect cavity designs. The cavities were placed in the center of the 9.43 mm long photonic crystal waveguides.

After testing, the first five waveguide designs, WG-1 through WG-5 were chosen for fabrication. WG-1 is a reference waveguide, WG-2 has a single cylinder missing creating a small cavity, WG-3 has 2 cylinders missing creating a larger cavity, WG-4 has a 3x1 cavity with a single cylinder removed as an aperture, and WG-5 has a 3x1 cavity with two cylinders removed as an aperture. As will be shown, each of these cavities produces sharp resonances and requires relatively simple fabrication. WG-6 and WG-8 were not chosen for fabrication as the lack of an aperture limited coupling to the cavity and no resonances appeared in the simulations. Simulations for WG-7 and WG-9 both showed a variety of resonances, but were more difficult to fabricate, and thus weren't chosen.

6.3 Photonic Crystal Waveguide Cavities: Experiment

After the simulations, the waveguide chips were fabricated and metalized. The chips were once again inserted into matched 9.43 mm long aluminum waveguides which were inserted into the THz-TDS system used for all experiments in this dissertation. Time-domain data was then taken for each of the five waveguides in sequential order. Figures 6.4a-6.4e show the THz time-domain pulses through each of the 4 waveguides. For the purposes of illustration, the pulses have been shown to 65 ps. The ringing extends to 130 ps when the reflections from the silicon lenses arrive. Longer scans were taken to ensure that the resonances were completely resolved, but the resonance's strength and linewidth did not vary. As such, the reflections were truncated at 130 ps, allowing un-wanted spectral oscillations to be removed. All four pulses show significant dispersion due to propagation through the dispersive photonic crystal waveguides.

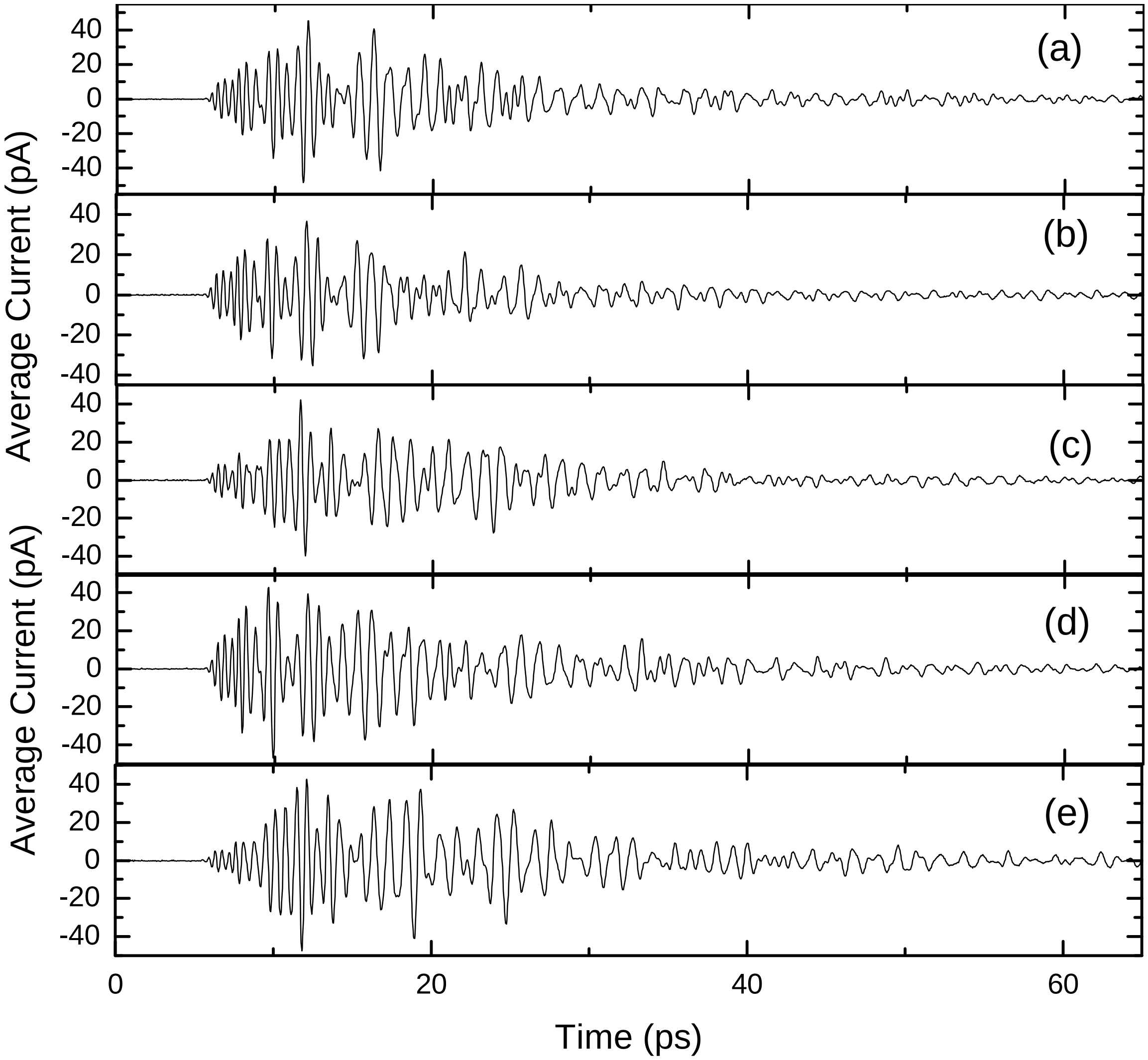

Figure 6-4 – Time domain pulses

The Fourier-transformed spectra for the four waveguides are shown in Figure 6.5. While the spectrum from WG-1 is similar to the previous demonstration of a photonic crystal waveguide, the subsequent waveguides with cavities all have sharp resonant lines. While there are a number of sharp features in each of the spectra, the focus will be on lines in the first passband, where transmission is cleanest. The relatively simple cavity of WG-2 has a sharp line at 0.914 THz, with an approximate FWHM width of 42 GHz. WG-3 has two sharp resonances, at 0.737 THz and 0.982 THz. The corresponding FWHM of these resonances are 18 GHz and 37 GHz. The most complex cavity, WG-4 has resonances at 0.903 THz and 1.034 THz. The corresponding FWHM of these resonances are 24 GHz and 13 GHz.

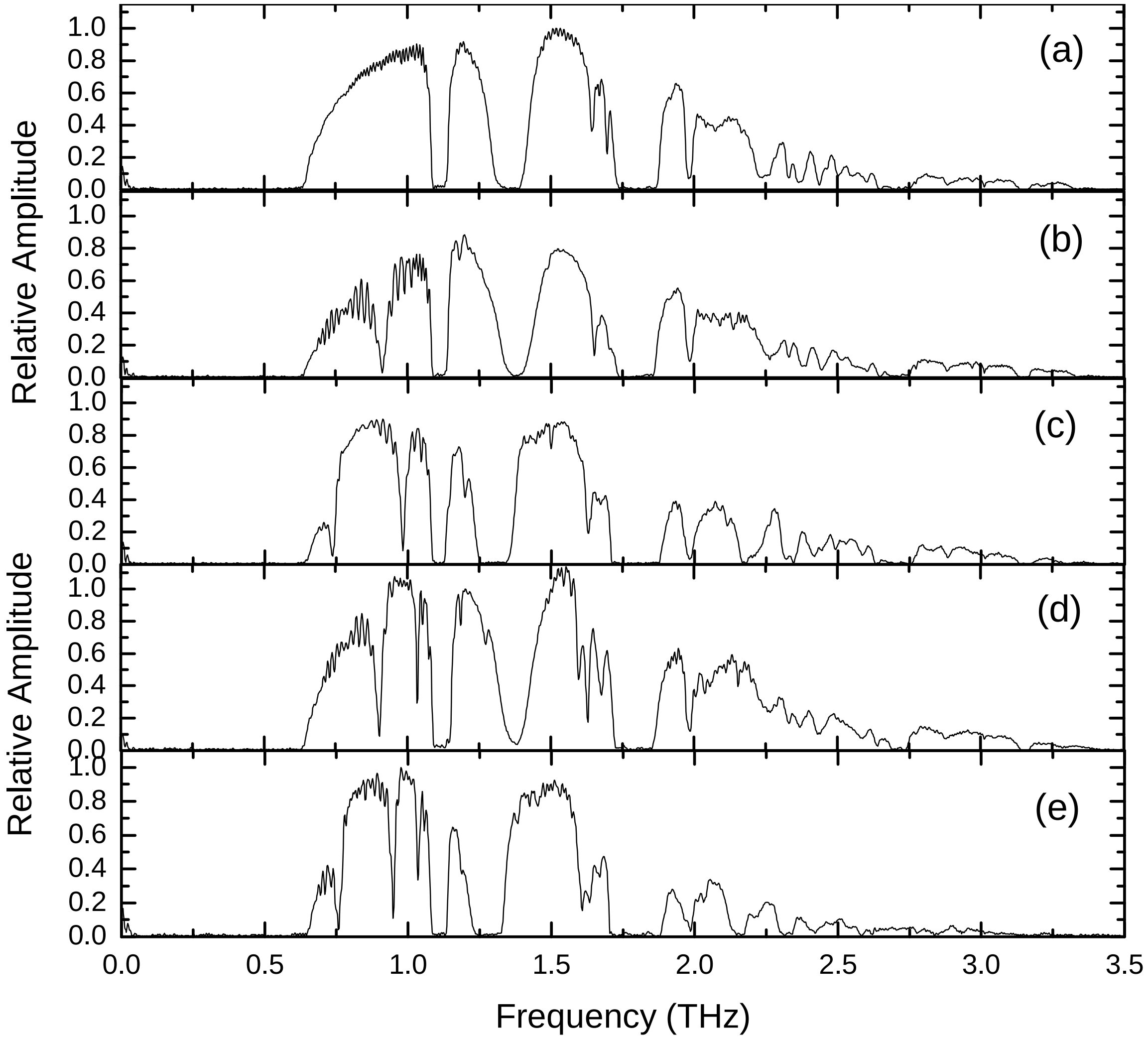

Figure 6-5 – Spectral Amplitudes of Cavities.

The cavities in the photonic crystal waveguides are notably sharper than the previously demonstrated traditional cavities in a rectangular waveguide which had typical FWHM of 50 GHz [72]. This is especially interesting as the photonic crystal waveguides have sharper lines despite having a significantly larger aperture. For comparison, the aperture of the photonic crystal cavities is a minimum of approximately 210 μm wide. For the rectangular waveguide cavities demonstrated earlier, the aperture is 110 μm wide, almost twice as small. Additionally, the photonic crystal boundary lacks the complete metallic boundary on the sidewalls of the cavity. This finding clearly illustrates the power of these photonic crystal waveguide cavities.

6.4 Photonic Crystal Waveguide Cavities: Theory

With the experimental data taken, a comparison between theory and data can now be made. The simulated output spectrum is compared to the experimental output spectrum of WG-2 in Figure 6.6. The simulation again had a 2 μm step size. The theoretical match is again quite good, especially in terms of the cavity resonance, which is well matched. However, for the waveguide cavity data, the stopband which is repeated for each of the waveguides just below 1.5 THz is not in the simulated spectrum (where heavy oscillations appear). The source of this discrepancy is unknown.

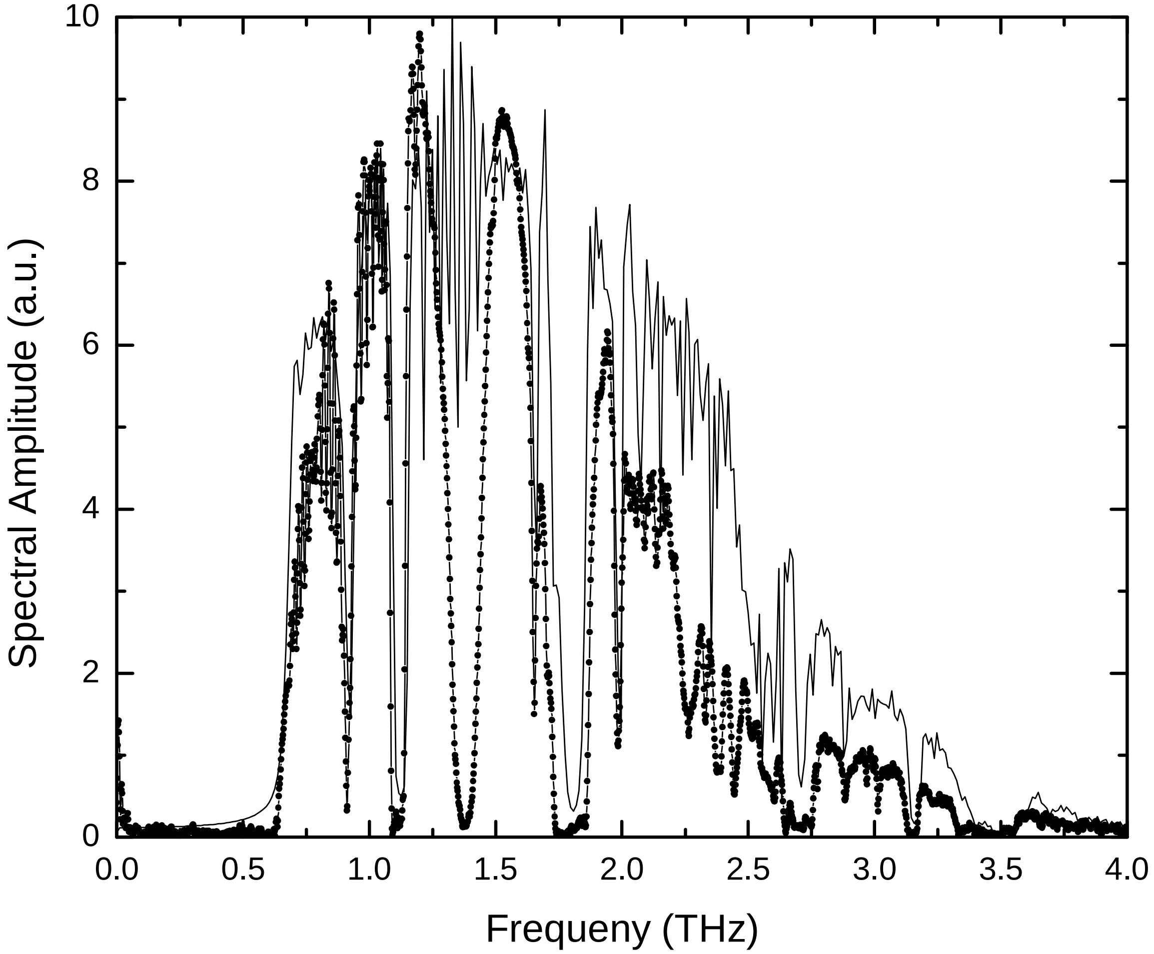

Figure 6-6 – Output spectra from experiment and simulation for WG-2. The experimental spectra is the dotted line.

The most important part of the data, the location and sharpness of the cavity resonances are for all of the waveguides in Table 6.2. The match between theory and experiment is excellent in terms of both the resonant frequency and the sharpness of the lines.

WAVEGUIDE	**RESONANT FREQUENCY (THZ)**	**FWHM (GHZ)**	**FDTD RESONANT FREQUENCY (GHZ)**	**FDTD FWHM (GHZ)**
WG-2	0.914	42	0.915	42
WG-3	0.737	18	0.736	14
WG-3	0.982	37	0.986	33
WG-4	0.903	24	0.902	20
WG-4	1.034	13	1.0350	10
WG-5	0.757	26	0.763	25
WG-5	0.948	22	0.951	25
WG-5	1.034	16	1.044	11

Table 6-2 – Comparison of resonant frequencies and linewidths from the experiment and the FDTD simulations.

6.5 Future Directions

The photonic crystal waveguide cavities investigated in this chapter demonstrated sharp resonances. The FDTD simulations used to design these cavities are in excellent agreement with the experimental observations, indicating that FDTD simulations will be provide design control for future integrated components. The photonic crystal waveguide cavities demonstrated cavities with resonances as much as 4x sharper than demonstrated for the rectangular waveguides at THz frequencies.

Chapter 7 - Conclusions

This dissertation demonstrated the integration of photonic crystal structures as a boundary in a parallel plate waveguide. A variety of devices were demonstrated under this basic premise, including filters, resonators, tunable filters, waveguide channels and waveguide bends. Each device demonstrated unique features with potential for future applications.

Chapter 3 focused on the photonic waveguides, which were defined as a parallel plate waveguide with a metallic periodic boundary replacing one of the planar waveguide plates. These 2-D photonic waveguides showed remarkable transmission characteristics with stopbands of varying bandwidth with a dynamic range of up to 40 dB and extremely sharp turn-ons. In order to simplify the geometry for future theoretical calculations, a transition to 1-D photonic waveguides was implemented with great success. Additionally, defects were incorporated into the 1-D photonic waveguide, allowing a high Q resonance to build up. Potential applications of the 1-D photonic waveguide chip with defect as a sensor were noted.

Chapter 4 investigated the use of the mode matching technique to theoretically simulate the transmission through a 1-D photonic waveguide. By viewing the 1-D photonic waveguide structure as a repetitive junction of PPWGs, the transmission through the device could be analytically calculated, which gives the user the freedom to design a filter with desired properties. The match between theory and experiment was shown to be excellent. Previous observations of a tunable bandstop filter based upon changing the plate spacing of a PPWG were simulated theoretically, providing a qualitative match for the observed 2-D photonic waveguide results.

Chapter 5 demonstrated the first planar photonic crystal waveguide at THz frequencies, for both the dielectric and metallic cases. While the dielectric photonic crystal channel was only weakly guiding, the metallic photonic crystal waveguide demonstrated loss approximately equal to that of a equivalently spaced rectangular waveguide. Considering the measured attenuation coefficients for metallic waveguides at THz frequencies rarely attain the loss predicted by theory, this was considered a significant advancement in terms of decreased loss.

Chapter 6 demonstrated integrated waveguide cavities in both standard rectangular and photonic crystal geometries. The results were matched FDTD simulations with excellent agreement. The photonic crystal waveguides generated significantly sharper lines than their rectangular counterparts.

As with any experiments, there are areas for either improvement or continued research. One could imagine the apodization of the 1-D photonic waveguides by adiabatically introducing the trenched section of the waveguide as opposed to the abrupt change demonstrated in this dissertation. This would remove the large oscillations surrounding the first bandgap providing a more useful filter. The high Q filter demonstrated by the 1-D photonic waveguide with an integrated defect will likely be utilized in ongoing PPWG spectroscopy experiments in the future. Perhaps the greatest amount of untapped potential lies in the photonic crystal waveguides demonstrated in Chapter 5. Any path and structure imaginable could be patterned into the photonic crystal chips offering almost unlimited possibilities in terms of splitters, interferometers, mode converters, resonators and other devices. The dielectric photonic crystal waveguide should not be abandoned, as novel device geometries should be utilized in order to attain guiding with loss that should be significantly lower than the metallic photonic crystal waveguide. By utilizing a more versatile experimental system with a fiber coupled receiver, the output at different points on a photonic crystal waveguide splitter could be measured.

The devices demonstrated in this dissertation all demonstrate performance at among the best currently available techniques at THz frequencies.

Bibliography

1. R. W. McGowan, G. Gallot, and D. Grischkowsky, "Propagation of Ultra-Wideband, Short Pulses of THz Radiation through Sub-mm Diameter Circular Waveguides." Opt. Lett. **24**, 1431-1433 (1999).
2. S. P. Jamison, R. W. McGowan, and D. Grischkowsky, "Single-mode waveguide propagation and reshaping of sub-ps terahertz pulses in sapphire fibers." Appl. Phys. Lett. **76**, 1987- 1989 (2000).
3. G. Gallot, S.P. Jamison, R.W. McGowan, D. Grischkowsky, "THz Waveguides" J. Opt. Soc. B., Vol. 17, 851- 863 (2000).
4. R. Mendis and D. Grischkowsky, "Plastic Ribbon THz Waveguides," J.Appl. Phys. **88**, 4449-4451 (2000).
5. R. Mendis and D. Grischkowsky, "Undistorted guided wave propagation of sub-picosecond THz pulses," Opt. Lett. **26**, 846-848 (2001).
6. Tae-In Jeon and D. Grischkowsky, "Direct optoelectronic generation and detection of subps electrical pulses on sub-mm coaxial transmission lines," Appl. Phys. Lett. **85**, 6092-6094 (2004).
7. K. Wang and D. M. Mittleman, “Metal wires for terahertz wave guiding,” Nature, **432**, 376 (2004).
8. Tae-In Jeon, Jiangquan Zhang and D. Grischkowsky, " THz Sommerfeld wave propagation on a single metal wire" Appl. Phys. Lett. **86**, 161904 (2005). S. Coleman and D. Grischkowsky, " A THz TEM-mode two dimensional interconnect layer incorporating quasi optics," Appl. Phys. Lett., **83**, 3656-3658 (2003).
9. S. Coleman, “2D TEM Mode THz Quasioptics,” PhD Disseration (2005).

10. S. Coleman and D. Grischkowsky, " Parallel plate THz transmitter," Appl. Phys. Lett. **84**, 654-656 (2004).
11. Jianming Dai, S. Coleman and D. Grischkowsky, " Planar THz Quasioptics," Appl. Phys. Lett. **85**, 884-886 (2004).
12. Y. Zhao and D. Grischkowsky, "Terahertz Demonstrations of Effectively Two Dimensional Photonic Bandgap Structures" Opt. Lett. **31**, 1534-1536, (2006).
13. Yuguang Zhao and Daniel R. Grischkowsky, "2-D Terahertz Metallic Photonic Crystals in Parallel-Plate Waveguides " IEEE Trans. Microwave Theory and Techniques, Vol. 55, 656 (2007).
14. Z. Jian, J. Pearce, and D. Mittleman, “Defect modes in photonic crystal slabs studied using terahertz time-domain spectroscopy”, Opt. Lett., **29**, 2067 (2004).
15. Z. Jian, J. Pearce, and D. Mittleman, “Two-dimensional photonic crystal slabs in parallel-plate metal waveguides studied with terahertz time-domain spectroscopy,” Semicond. Sci. and Tech. **20**, 300 (2005).
16. M. Nagel, P. Bolivar, and H. Kurz, “Modular parallel-plate THz components for cost-efficient biosensing systems”, Semicond. Sci. Tech. **20,** S281 (2005).
17. Tushar Prasad, Vicki L. Colvin, Zhongping Jian, and Daniel M. Mittleman, “The superprism effect in a metal-clad terahertz photonic crystal slab,” Opt. Lett. **32**, 683 (2007).
18. J. Joannopoulos, R. Meade, and J. Winn, *Photonic Crystals: Molding the Flow of Light* (Princeton University Press, Princeton, 1995).
19. E. Yablonovitch “Inhibited Spontaneous Emission in Solid-State Physics and Electronics,” Phys. Rev. Lett. **58**, 2059 - 2062 (1987).
20. P. St. J. Russell, "Photonic crystal fibers," Science 299, 358-362 (2003).
21. H. Nemec, P. Kuzel, F. Garet, and L. Duvillaret, “Time-domain terahertz study of defect formation in one-dimensional photonic crystals,” Appl Opt. **43**, 1965-70 (2004).

22. N. Jukam, and M. Sherwin, “Two-Dimenisional terahertz photonic crystal fabricated by deep refractive ion etching in Si”, Appl. Phys. Lett. **83**, 21 (2003).

23. H. Park, M. Cho, J. Kim, and H. Han, “Terahertz pulse transmission in plastic photonic crystal fibres,” Phys. Med. Biol. **47** 3765-3769 (2002).

24. F. Miyamuru, T. Kondo, T. Nagashima, and M. Hangyo, “Large Polarization change in two-dimensional metallic photonic crystals in subterahertz region”, Appl. Phys. Lett., **82**, 2568 (2003).

25. C. Jin, B. Cheng, Z. Li, D. Zhang, L. Li, and Z. Zhang, “Two dimensional metallic photonic crystal in the THz range”, Opt. Comm. **166**, 9 (1999)

26. S. Wang, W. Lu, X. Chen, Z. Li, X. Shen and W. Wen, “Two-Dimensional photonic crystal at THz frequencies constructed by metal-coated cylinders”, J. Appl. Phys., **93**, 9401 (2003).

27. M. Goto, A. Quema, H. Takahashi, S. Ono and N. Sarukura, “Teflon Photonic Crystal Fiber as Terahertz Waveguide,” Jap. Journal Appl. Phys. **43,** L317-L319 (2004).

28. M. Cho, H. Park, Y. Han and H. Han, “Air-guiding photonic crystal waveguides for terahertz radiation,” Proc. Of SPIE **6351**, 63511I-2 (2006).

29. Z. Li, Y. Zhang, and B. Li, “Terahertz photonic crystal switch in silicon based on self-imaging principle,” Opt. Exp. **14**, 3887-3892 (2006).

30. H. Kurt, and D. Citrin, “Photonic crystals for biochemical sensing in the terahertz region,” Appl. Phys. Lett. **87**, 041108 (2005).

31. A. J. Gallant, M. A. Kaliteevski, D. Wood, M. C. Petty, R. A. Abram, S. Brand, G. P. Swift, D. A. Zeze, and J. M. Chamberlain, “Passband filters for terahertz radiation based on dual metallic photonic structures,” Appl. Phys. Lett. 91, 161115 (2007).

32. A. Bingham, Yuguang Zhao and D. Grischkowsky, " THz parallel plate photonic waveguides" Appl. Phys. Lett. **87**, 051101-1 (2005).

33. A. L. Bingham and D. Grischkowsky, " High Q, one-dimensional terahertz photonic waveguides " Appl. Phys. Lett., **90**, 091105 (2007).

34. A. Cheville “GB Menu” MATLAB program Oklahoma State University (1998).

35. J. Verdeyen, *Laser Electronics*, 3rd ed. (Prentice Hall, New Jersey, 1995).

36. P. Goldsmith, *Quasioptical Systems*, IEEE Press, New York, 1998).

37. Y. Zhao, “Study of photonic crystal structures by THz-TDS,” PhD Dissertation (2006).

38. L. Brillouin “Waveguides for Slow Waves”, J. Appl. Phys. **19,** 1023 (1948).

39. S. Cohn, “Analysis of a Wide-Band Waveguide Filter, Proc. IRE 651 **37** (1949).

40. S. B. Cohn “Design Relations for the Wide-Band waveguide filter” Proc. IRE **38,** 799 (1950).

41. S. Cohn, “Direct-Coupled-Resonator Filters”, Proc. IRE 187 **45** (1957).

42. E. Sharp, “A High-Power Wide-Band Waffle-Iron Filter” IEEE Trans. Microwave Theory Tech. **MTT-11**, 111 (1963).

43. R. Levy, “Theory of Direct-Coupled-Cavity Filters” IEEE Trans Microwave Theory Tech. **MTT-15** 340 (1967).

44. R. Levy, “Tapered Corrugated Waveguide Low-Pass Filters” IEEE Trans Microwave Theory Tech. **MTT-21** 526 (1973).

45. G. Matthaei, L. Young, and E. Jones, *Microwave Filters, Impedance-Matching Networks, and Coupling Structures* (Artech House, Boston, 1980).

46. R. Levy and S. Cohn, “A History of Microwave Filter Research, Design, and Development” IEEE Trans. Microwave Theory Tech. **MTT-32,** 1055 (1984).

47. N. Marcuvitz, *Waveguide Handbook,* (Peter Peregrinus, London, UK 1993).

48. M. Sadiku, *Numerical Techniques in Electromagnetics*, (CRC Press, Second Ed., 2000).

49. M. Nagel, P. Bolivar, M. Bruchherseifer, H. Kurz, A. Bosserhoff, and R. Buttner, “Integrated THz Technology for label-free genetic diagnostics”, Appl. Phys. Lett. **80,** 154 (2002).

50. A. Wexler, “Solution of Waveguide Discontinuities by Modal Analysis” IEEE Trans. Microwave Theory Tech. **MTT-15** 508 (1967).

51. R. Abram and G. Rees, “Mode Conversion in an imperfect waveguide” J. Phys. A:Math., Nucl. Gen. **6** 1693 (1973).

52. R. Safavi-Naini and R. Macphie “On Solving Waveguide Junction Scattering Problems by the Conservation of Complex Power Technique” IEEE Trans Microwave Theory Tech. **MTT-29,** 337 (1981).

53. J. Wade and R. Macphie, “Scattering at Circular-to-Rectangular Waveguide Junctions”, IEEE. Trans. Microwave Theory Tech., **MTT-34** 1085 (1986).

54. R. Safavi-Naini and R. Macphie, “Scattering at Rectangular-to-Rectangular Waveguide Junctions”, IEEE Trans. Microwave Theory Tech., **30** 2060 (1982).

55. J. Wade, and R. Macphie, “Conservation of Complex Power Technique for Waveguide Junctions with Finite Wall Conductivity”, IEEE Trans. Microwave Theory Tech., **38** 373 (1990).

56. G. Eleftheriades, A. Omar, L. Katehi, and G. Rebeiz, “Some Important Properties of Waveguide Junction Generalized Scattering Matrices in the Context of the Mode Matching Technique”, IEEE Trans. Microwave Theory Tech. **42** 1896 (1994)

57. P. Borsboom and H. Frankena, “Field analysis of two-dimensional integrated optical gratings” J. Opt. Soc. Am. A **12**, 1134 (1995).

58. J. Frolik, and A. Yagle, “ An Asymmetric Discrete-Time Approach for the Design and Analysis of Periodic Waveguide Gratings” J. Lightwave Tech. **13**, 175 (1995).

59. T. Thumvongskul and T. Shiozawa, “Reflection Charateristics of a Metallic Waveguide Grating with Rectangular Grooves as a Frequency-Selective Reflector”, Microwave and Opt. Tech. Lett., **32** 414 (2002).

60. T. Thumvongskul, Y. Fukunaga, A. Hirata, and T. Shiozawa, “Design of a Compact and Wide-Band Metallic Reflector Grating for Single-Mode Operation”, IEEE Trans. Plasma Science, **30** 2042 (2002).

61. S. Kondoh, A. Hirata, T. Thumvongskul, and T. Shiozawa, “Analysis of a Metallic Reflector Grating with Influence of Joule Loss Taken Into Account”, IEEE Trans. Plamsa Science, **31** 1070 (2003).
62. S. Kondoh, A. Hirata, T. Shiozawa, “A Compact and Wide-Band Metallic Reflector Grating in a Rectangular Waveguide”, IEEE Trans. Plasma Science, **32** 1318 (2004).
63. D. Pozar, *Microwave Engineering* (John Wiley & Sons, New York, 1998).
64. M. Born and E. Wolf, *Principles of Optics* (Cambridge University Press, Cambridge, UK, 1999).
65. R. Redheffer and E. Beckenbach (ed.) *Modern Mathematics for the Engineer* (McGraw-Hill Book Company, New York, 1961).
66. A. Bingham and D. Grischkowsky, “1-D Terahertz Photonic Waveguides, Conference on Lasers and Electro-Optics (CLEO), Baltimore, 2007.
67. Y. Zhao and D. Grischkowsky “A New Method for the Realization of a Tunable Terahertz Photonic Bandgap,” Conference on Lasers and Electro-Optics, Baltimore, 2007.
68. Thomas F. Krauss, “Planar photonic crystal waveguide devices for integrated optics”, Phys. Stat. Sol. (a) **197**, 688-702 (2003).
69. A. Bingham and D. Grischkowsky, “Terahertz 2-D Photonic Crystal Waveguides,” submitted to IEEE Microwave and Wireless Components Letters, (2007).
70. N. Laman and D. Grischkowsky, "Reduced conductivity in the terahertz skin-depth layer of metals," Appl. Phys. Lett. **90**, 122115 (2007).
71. M. Qiu, F2P: Finite-difference time-domain 2D simulator for Photonic devices, http://www.imit.kth.se/info/FOFU/PC/F2p/
72. P. George, C. Manolatou, F. Rana, A. Bingham, and D. Grischkowsky, “Integrated Waveguide-Coupled Terahertz Microcavity Resonators”, Applied Physics Letters, To be published 2007.

Appendixes

Appendix A

Proof of Power Conservation for Field Quantities:

Power conservation of the single waveguide junction shown in Figure 4.3 is shown by summing the total power in each mode, then equating the normalized incident, transmitted and reflected powers according to equation (A1).

$$P_{inc} + P_{ref} = P_{trans} \tag{A1}$$

Assume that only the 3 lowest order modes exist in each waveguide.

The incident fields are

$$E_{inc} = \frac{1}{\sqrt{a}} E_o \tag{A2}$$

$$H_{inc} = \frac{1}{\sqrt{a}} \frac{E_o}{\eta_o} \tag{A3}$$

The transmitted fields are

$$E_{trans} = \sum_{n=0}^{2} E_o S_{n1}^{21} \Phi_{bn} \hat{y} \tag{A4}$$

$$H_{trans} = \sum_{n=0}^{2} E_o S_{n1}^{21} \frac{\Phi_{bn}}{Z_{bn}} \hat{x} \tag{A5}$$

And the reflected fields are

$$E_{ref} = \sum_{n=0}^{2} E_o S_{n1}^{11} \Phi_{an} \hat{y} \tag{A6}$$

$$H_{ref} = \sum_{n=0}^{2} E_o S_{n1}^{11} \frac{\Phi_{an}}{Z_{an}} \hat{x} \tag{A7}$$

Where S^{11} represents the scattering matrix coefficients for the modes reflected into waveguide a, and the S^{21} represents the scattering matrix coefficients for the modes transmitted into waveguide b. The transmitted and reflected fields are frequency dependent due to the frequency dependent impedances and scattering matrix coefficients

The Power will be calculated by the using the Poynting Vector [63]. The incident power is given by (A8)

$$P_{inc} = \tfrac{1}{2}\iint_{S1} \left(E_{inc} \times H_{inc}\right) \cdot ds1 = \tfrac{1}{2}\int_0^a \int_0^w \frac{E_o^2}{a\eta_o} dxdy = \frac{1}{2}\frac{E_o^2 w}{\eta_o} \tag{A8}$$

Following the same procedure for the transmitted and reflected field (summing each mode separately)

$$P_{trans} = \sum_{n=0}^{2} \tfrac{1}{2}\iint_{S2} \left(E_{trans}^{n} \times H_{trans}^{n}\right) \cdot ds2 = \frac{1}{2} E_o^2 w \left(\frac{\left|S_{01}^{21}\right|^2}{\eta_o} + \frac{\left|S_{11}^{21}\right|^2}{Z_{b1}} + \frac{\left|S_{21}^{21}\right|^2}{Z_{b2}} \right) \tag{A9}$$

$$P_{ref} = \sum_{n=0}^{2} \tfrac{1}{2}\iint_{S1} \left(E_{ref}^{n} \times H_{ref}^{n}\right) \cdot ds1 = \frac{1}{2} E_o^2 w \left(\frac{\left|S_{01}^{11}\right|^2}{\eta_o} + \frac{\left|S_{11}^{11}\right|^2}{Z_{a1}} + \frac{\left|S_{21}^{11}\right|^2}{Z_{a2}} \right) \tag{A10}$$

Plugging (A8-A10) into the power conservation equation (A1) yields

$$\frac{1}{2}\frac{E_o^2 w}{\eta_o} - \frac{1}{2} E_o^2 w \left(\frac{\left|S_{01}^{11}\right|^2}{\eta_o} + \frac{\left|S_{11}^{11}\right|^2}{Z_{a1}} + \frac{\left|S_{21}^{11}\right|^2}{Z_{a2}} \right) = \frac{1}{2} E_o^2 w \left(\frac{\left|S_{01}^{21}\right|^2}{\eta_o} + \frac{\left|S_{11}^{21}\right|^2}{Z_{b1}} + \frac{\left|S_{21}^{21}\right|^2}{Z_{b2}} \right) \tag{A11}$$

Canceling like terms results in the final power conservation equation.

$$1-\eta_o\left(\frac{\left|S_{01}^{11}\right|^2}{\eta_o}+\frac{\left|S_{11}^{11}\right|^2}{Z_{a1}}+\frac{\left|S_{21}^{11}\right|^2}{Z_{a2}}\right)=\eta_o\left(\frac{\left|S_{01}^{21}\right|^2}{\eta_o}+\frac{\left|S_{11}^{21}\right|^2}{Z_{b1}}+\frac{\left|S_{21}^{21}\right|^2}{Z_{b2}}\right) \qquad \text{(A12)}$$

To verify conservation of power, the 2nd and 3rd terms in equation (A12) were plotted in MATLAB. The results are shown in Figure A.1. The sum of the 2nd and 3rd terms is unity, confirming the conservation of power at a waveguide junction calculated from Mode Matching Theory.

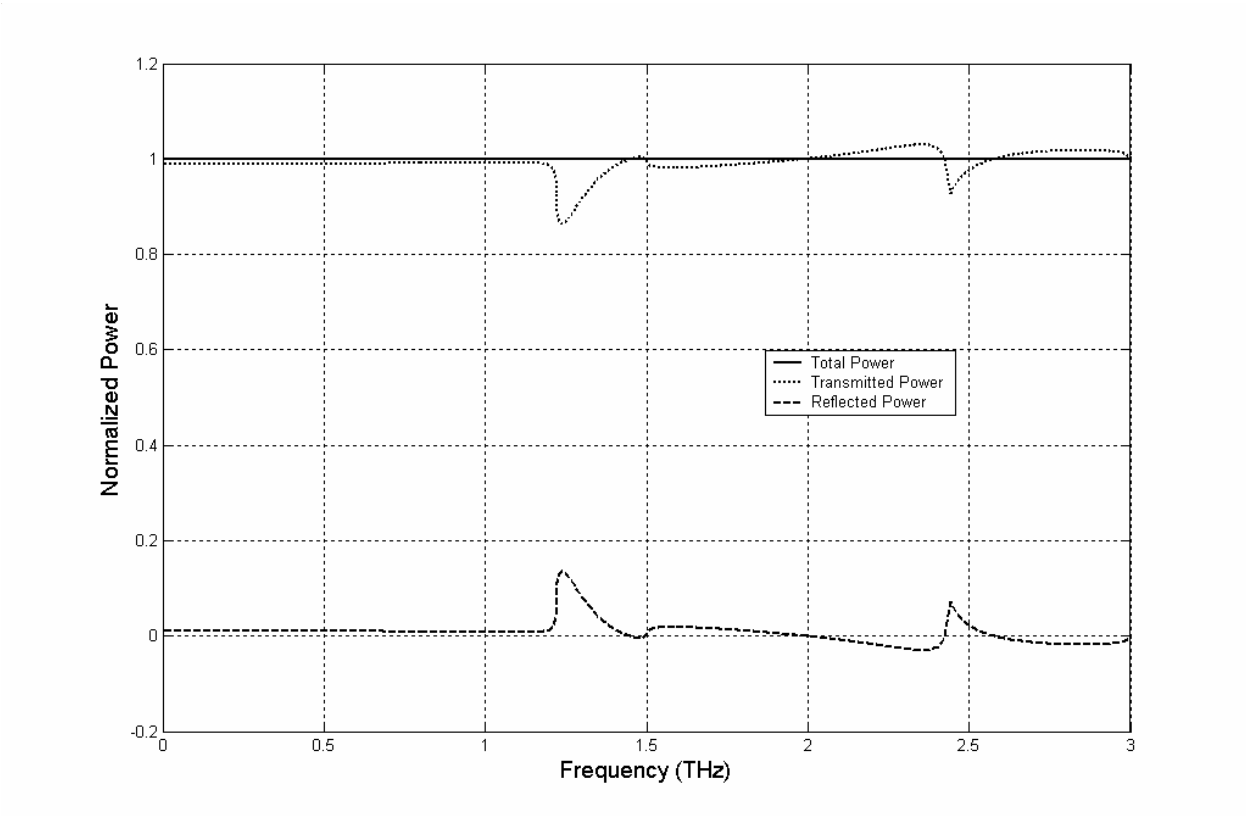

Figure A.1: Proof of conservation of power. The 2nd (dashed line) and 3rd (dotted line) terms from (A12) are plotted, as well as their sum (solid line). The sum equals unity, balancing equation (A12) and confirming the conservation of power.

Appendix B

Equivalency of Cascaded Scattering Matrices and Thin Film Transmission and Reflection Coefficients

In Chapter 4.6, we calculated the scattering matrix for a single trench, by simply cascading the scattering matrices for each part of the trench. However, for the most part this was done with simple matrix algebra. To verify that this process takes into account the multiple Fabry-Perot reflections from any structure with two interfaces, we will now convert equation (4.50) into the well known transmission and reflection coefficients for a thin film [64]. While (4.50) is extremely complex, we will start making simplifications immediately. First, assume that these structures only allow a single mode to propagate. Additionally, we'll switch from scattering matrix parameters to the equivalent notation for a thin film. As such

$$\begin{bmatrix} S_{11}^{1} & S_{12}^{1} \\ S_{21}^{1} & S_{22}^{1} \end{bmatrix} \Rightarrow \begin{bmatrix} r_{12} & t_{21} \\ t_{12} & r_{21} \end{bmatrix} \text{ and } \begin{bmatrix} S_{11}^{2} & S_{12}^{2} \\ S_{21}^{2} & S_{22}^{2} \end{bmatrix} \Rightarrow \begin{bmatrix} r_{23} & t_{32} \\ t_{23} & r_{32} \end{bmatrix} \qquad \text{(B1)}$$

The assumption that we are now in the single mode also causes I, the identity matrix, to become a 1x1 matrix with a single, unity element. Therefore, matrix algebra rules no longer apply. To determine the total reflection coefficient with incidence on the left of the structure shown in Figure 4.7, set D- = 0, allowing

$$\frac{A-}{A+} = r_{LEFT} = S_{11}^{1} + S_{12}^{1} T_2 (I - S_{11}^{2} T_2 S_{22}^{1} T_2)^{-1} S_{11}^{2} T_2 S_{21}^{1} = r_{12} + \frac{t_{21} t_{12} r_{23} T_2^2}{1 - r_{23} r_{21} T_2^2} \qquad \text{(B2)}$$

For the transmission coefficient with incidence from the left,

$$\frac{D+}{A+} = t_{LEFT} = S_{21}^{2} (I - T_2 S_{22}^{1} T_2 S_{11}^{2})^{-1} T_2 S_{21}^{1} = \frac{t_{23} t_{12} T_2}{1 - r_{23} r_{21} T_2^2} \qquad \text{(B3)}$$

It is just as simple to determine the reflection and transmission coefficients for incidence from the right. Letting A+ = 0,

$$\frac{D+}{D-} = r_{RIGHT} = S_{22}^{2} + S_{21}^{2} (I - T_2 S_{22}^{1} T_2 S_{11}^{2})^{-1} T_2 S_{22}^{1} T_2 S_{12}^{2} = r_{32} + \frac{t_{23} r_{21} t_{32} T_2^2}{1 - r_{21} r_{23} T_2^2} \qquad \text{(B4)}$$

$$\frac{A-}{D-} = t_{RIGHT} = S_{12}^{1} T_2 (I - S_{11}^{2} T_2 S_{22}^{1} T_2)^{-1} S_{12}^{2} = \frac{t_{21} t_{32} T_2}{1 - r_{21} r_{23} T_2^2} \qquad \text{(B5)}$$

Before we prove that these formulas are equivalent to the thin film formulas, the fact that the experimental geometry is symmetric must be taken into account. If waveguide 1 and waveguide 3 are identical, then

$$r_{23} = r_{21}$$

$r_{32} = r_{12}$

$t_{23} = t_{21}$

$t_{32} = t_{12}$

With these substitutions,

$$r_{LEFT} = r_{12} + \frac{t_{21}t_{12}r_{23}T_2^2}{1 - r_{21}r_{21}T_2^2} = r_{RIGHT} = r_{scattering} \tag{B6}$$

and

$$t_{LEFT} = \frac{t_{21}t_{12}T_2}{1 - r_{21}r_{21}T_2^2} = t_{RIGHT} = t_{scattering} \tag{B7}$$

The reflection and transmission coefficients are identical with incidence on both sides of the junction for the symmetric geometry. Now that (B6) and (B7) are in the proper notation, all that remains is algebra. Assuming a symmetric structure, the Born and Wolf formulas [64] reduce to

$$r_{th\inf ilm} = \frac{r_{12} + r_{21}e^{-2j\beta d}}{1 + r_{12}r_{21}e^{-2j\beta d}} \tag{B8}$$

$$t_{th\inf ilm} = \frac{t_{12}t_{21}e^{-j\beta d}}{1 + r_{12}r_{21}e^{-2j\beta d}} \tag{B9}$$

Converting (B6) into (B8) is simple. The two expressions are identical with the exception of denominators. By inserting $r_{21} = -r_{12}$ into (20), the expressions for the complex transmission are equivalent. Explicitly,

$$t_{scattering} = \frac{t_{21}t_{12}e^{-j\beta d}}{1-r_{21}r_{21}e^{-2j\beta d}} \Rightarrow r_{21} = -r_{12} \Rightarrow t_{th\inf ilm} = \frac{t_{12}t_{21}e^{-j\beta d}}{1+r_{12}r_{21}e^{-2j\beta d}} \quad \text{(B10)}$$

The conversion from (B7) to (B9) is requires more algebra. Taking (B7), and making 3 substitutions,

$$r_{21} = -r_{12}$$

$$t_{12} = 1+r_{21}$$

$$t_{21} = 1+r_{12}$$

Gives us

$$r_{scattering} = r_{12} + \frac{t_{21}t_{12}r_{23}e^{-2j\beta d}}{1-r_{21}r_{21}e^{-2j\beta d}} \Rightarrow substitions \Rightarrow r_{12} + \frac{(1+r_{12})(1+r_{21})r_{21}e^{-2j\beta d}}{1+r_{12}r_{21}e^{-2j\beta d}} \quad \text{(B11)}$$

Multiplying everything out,

$$r_{scattering} = r_{12} + \frac{(1+r_{12}+r_{21}+r_{21}r_{12})r_{21}e^{-2j\beta d}}{1+r_{12}r_{21}e^{-2j\beta d}} \quad \text{(B12)}$$

Cancelling terms,

$$r_{scattering} = r_{12} + \frac{(1+r_{21}r_{12})r_{21}e^{-2j\beta d}}{1+r_{12}r_{21}e^{-2j\beta d}} \quad \text{(B13)}$$

Multiplying both sides by the denominator,

$$(1+r_{12}r_{21}e^{-2j\beta d})r_{scattering} = (1+r_{12}r_{21}e^{-2j\beta d})r_{12} + (1+r_{21}r_{12})r_{21}e^{-2j\beta d} \quad \text{(B14)}$$

Work out the algebra on the right side, cancelling terms again,

$$(1+r_{12}r_{21}e^{-2j\beta d})r_{scattering} = r_{12} + r_{21}e^{-2j\beta d} \quad \text{(B15)}$$

Finally, divide everything by the term on the left

$$r_{scattering} = \frac{r_{12}+r_{21}e^{-2j\beta d}}{1+r_{12}r_{21}e^{-2j\beta d}} = r_{th\inf ilm} \quad \text{(B16)}$$

This of course is equal to the formula for the reflection coefficient from a thin film. As such, we can conclude that the technique of cascading scattering matrices does indeed take into account multiple reflections.

VITA

Adam Lee Bingham

Candidate for the Degree of

Doctor of Philosophy

Thesis: PROPAGATION THROUGH TERAHERTZ WAVEGUIDES WITH PHOTONIC CRYSTAL BOUNDARIES

Major Field: Photonics

Biographical:

Personal Data: Born in Norman, Oklahoma.

Education: B.S. Optics, 2003, University of Rochester, Rochester, New York. Completed the requirements for the Doctor of Philosophy in Photonics at Oklahoma State University, Stillwater, Oklahoma in December, 2007.

Experience: Recipient of Integrative Graduate Education and Research Traineeship (IGERT) Fellowship at Oklahoma State University from 2003 to 2004. Investigated terahertz waveguides with photonic crystal boundaries while employed as a Research Assistant under Dr. Daniel Grischkowsky at Oklahoma State University in the Department of Electrical and Computer Engineering from 2004 to 2007.

Professional Memberships: Student member of Institute of Electrical and Electronics Engineers (IEEE), Optical Society of America (OSA), and SPIE – The International Society for Optical Engineering.

Name: Adam L. Bingham Date of Degree: December, 2007

Institution: Oklahoma State University Location: Stillwater, Oklahoma

Title of Study: PROPAGATION THROUGH TERAHERTZ WAVEGUIDES WITH PHOTONIC CRYSTAL BOUNDARIES

Pages in Study: 122 Candidate for the Degree of Doctor of Philosophy

Major Field: Photonics

Scope and Method of Study: The research presented in this dissertation investigates the integration of photonic crystal lattices into parallel plate waveguides at terahertz frequencies. The experimental data was obtained by measuring the terahertz pulses through the photonic crystal waveguides in a standard terahertz time-domain spectroscopy system. The terahertz pulses were generated and detected via optoelectronic means utilizing lithographically fabricated transmitting and receiving antennas and a femtosecond laser.

Findings and Conclusions: The main findings of this research are that metallic photonic crystal waveguides are a potential two-dimensional interconnect, and photonic waveguides act as an excellent guided-wave filter. The photonic crystal waveguides demonstrate attenuation approximating that of a comparable metallic waveguide, and demonstrate the capability to integrate guided-wave components with a high level of performance. The photonic waveguides act as a powerful filter, and the mode-matching theory allows complete design control over the waveguides.

ADVISER’S APPROVAL: Dr. Daniel Grischkowsky